



TECHNISCHE
UNIVERSITÄT
WIEN

DISSERTATION

Novel Insights into Ion-Solid Interaction: Case Studies for Space Weathering and Nuclear Fusion Research

Ausgeführt zum Zwecke der Erlangung des akademischen Grades
eines Doktors der technischen Wissenschaften
unter der Leitung von

Univ.-Prof. Dr. Friedrich Aumayr
E134
Institut für Angewandte Physik

eingereicht an der Technischen Universität Wien
Fakultät für Physik
von

Dipl.-Ing. Paul S. Szabo
Matrikelnummer: 01225017
Breitenseer Straße 58/9
1140 Wien

Wien, Mai 2021

(Paul S. Szabo)

Abstract

An extended understanding of ion-solid interaction processes is of great interest in many different research areas. Especially for weathering of the surfaces of planets, moons and asteroids, many relevant effects that are caused by solar wind ions are not yet completely understood and require more experimental research. Another driver for the investigation of ion-solid interaction is nuclear fusion research. The feasibility of this promising energy source of the future is strongly affected by the interaction of plasma ions with wall materials of the reactor. Besides the erosion of the wall, the implantation and retention of hydrogen in wall materials are also important issues that still cause several challenges.

This thesis aims to investigate ion-solid interaction effects to increase the understanding of both space weathering and nuclear fusion research. For this purpose, the sputtering due to ion bombardment as well as H retention were investigated by performing experiments and numerical simulations.

The sputtering behavior of wollastonite (CaSiO_3) as an analog material for the surfaces of the Moon and Mercury was measured in detail using the quartz crystal microbalance technique. The sputtering yields of the major solar wind components H and He could be quantified precisely and for the first time, an extensive study of the angular dependence of the sputtering yield was performed. Sputtering was simulated with the program SDTrimSP and the used input parameters were optimized to allow consistent prediction of sputtering yields, which will be helpful for future studies. Furthermore, potential sputtering of both He^{2+} and multiply charged Ar ions was examined. The observed dynamic behavior could be connected to potential sputtering and subsequent depletion of O near the surface. Based on the experimental findings of He^{2+} , the total effect of solar wind potential sputtering could be calculated to give an overall sputtering increase of about 40%, which underlines the importance of this effect for space weathering.

As a special case, space weathering of the Martian moon Phobos by O ions from the Martian atmosphere was also investigated experimentally and numerically. In this

context, thin films of the mineral augite $((\text{Ca,Mg,Fe})_2\text{Si}_2\text{O}_6)$ deposited on a quartz crystal microbalance were used as an analog for the surface of Phobos. Sputtering yields for both atomic and molecular O ions could be quantified at different energies, revealing significant signs of O implantation in the material. The sputtering yields by O ions were found to be 50% smaller than in previously published models, but the presented findings still show the importance of planetary O ions for the erosion of the Mars-facing side of Phobos.

In the area of nuclear fusion research, this thesis explores new experimental approaches of measuring H isotope retention in the reactor wall material W. Nuclear Reaction Analysis with ^{15}N ions was applied to perform precise depth profiling of H in a W film sample. However, the ^{15}N irradiation was found to significantly alter the retention behavior, which led to a complete absence of gas-filled blisters in the ^{15}N -irradiated areas. The observations could be explained by the additional damages in the W film that were caused by the probing ion beam. The results achieved in this context are not only relevant for the investigation of H retention by ion beam analysis itself, but also for re-deposited W layers in a nuclear fusion reactor. The damages from neutrons created during the fusion process could significantly alter how H isotopes are retained in these layers. A second ion beam analysis method, Elastic Recoil Detection, proved to be better suited for monitoring D depth profiles. H and D concentrations can be measured at different depths at the same time, providing more detailed insights into H isotope retention and desorption than other techniques. This could be shown for the case of D implanted in W, but Elastic Recoil Detection will also represent a powerful tool for further similar analysis.

In this thesis, new insights for both space weathering and plasma-wall interaction research could be achieved. Sputtering and hydrogen retention behaviors could be investigated in both experiment and simulation with the aim of increasing the understanding of the relevant ion-solid interaction effects. Both the applicability of different experimental approaches as well as the usage of the simulation program SDTrimSP discussed in this thesis will surely give a connection point for future studies in planetary science and fusion research.

Kurzfassung

Ein tieferes Verständnis der Ionen-Festkörper-Wechselwirkung ist in mehreren Forschungsbereichen von großem Interesse. Vor allem im Zusammenhang mit der Verwitterung von Planeten-, Mond- und Asteroidenoberflächen ist eine Vielzahl von Effekten, die durch Sonnenwindionen verursacht werden, noch nicht gänzlich verstanden. Die Kernfusionsforschung stellt ein weiteres Forschungsfeld dar, welches Untersuchungen im Bereich der Ionen-Festkörper-Wechselwirkung vorantreibt. Besonders die effiziente Umsetzung dieser vielversprechenden Energiequelle ist stark an das Verständnis der Interaktion zwischen Plasmaionen und Wandmaterialien des Reaktors geknüpft. Neben der Erosion der Reaktorwand sind auch die Implantation und Speicherung von Wasserstoffisotopen im Wandmaterial wichtige Themen, die immer noch Herausforderungen darstellen.

Diese Doktorarbeit setzt sich zum Ziel, das Verständnis der Wechselwirkung von Ionen mit Festkörpern sowohl im Bereich der Weltraumverwitterung als auch in der Kernfusionsforschung zu erweitern. In diesem Zusammenhang wurden die Zerstäubung durch Ionenbeschuss und die Wasserstoffspeicherung mit Experimenten und begleitenden numerischen Simulationen erforscht.

Die Zerstäubung von Wollastonit (CaSiO_3) als Analogmaterial für die Oberflächen des Mondes oder Merkurs wurde mit der Quarzkristallmikrowaagentchnik detailliert untersucht. Die Zerstäubungsausbeuten der Hauptkomponenten des Sonnenwinds, Wasserstoff und Helium, konnten präzise quantifiziert werden und es wurden erstmals ausführliche Winkelabhängigkeiten dieser Größen gemessen. Die Zerstäubung wurde mit dem Programm SDTrimSP berechnet, wobei Simulationsparameter optimiert wurden, um die präzise Vorhersage dieser Größen zu ermöglichen, was auch für zukünftige Untersuchungen hilfreich sein wird. Außerdem wurde die potenzielle Zerstäubung durch zweifach geladene Helium- und mehrfach geladene Argonionen untersucht. Das beobachtete dynamische Verhalten dieses Vorgangs konnte erfolgreich durch ein theoretisches Modell der präferentiellen Sauerstoffzerstäubung und der damit verbundenen Verringerung des Sauerstoffanteils der Oberfläche erklärt werden. Auf Basis dieser experimentellen Ergebnisse wurde der Anteil der potenzi-

ellen Zerstäubung bei der Oberflächenerosion durch Sonnenwindionen berechnet. Das Ergebnis ist ein Anstieg der Erosion um etwa 40%, was den wichtigen Beitrag dieses Effekts zur Weltraumverwitterung unterstreicht.

Als ein Sonderfall der Weltraumverwitterung wurde die Erosion des Marsmonds Phobos durch Sauerstoffionen, die in der Marsatmosphäre erzeugt werden, anhand von Laborexperimenten und numerischen Simulationen untersucht. In diesem Zusammenhang wurden dünne Augitschichten $((Ca,Mg,Fe)_2Si_2O_6)$ auf Quarzkristallmikrowaagen als Analogmaterial für die Phobosoberfläche verwendet. Zerstäubungsausbeuten wurden sowohl für atomare als auch molekulare Sauerstoffionen mit unterschiedlichen Energien gemessen, wobei deutliche Anzeichen von Sauerstoffimplantation beobachtet wurden. Die Zerstäubungsausbeuten durch die Sauerstoffbestrahlung waren um 50% niedriger als jene, die für früher publizierte Modellrechnungen zur Phobosverwitterung angenommen wurden. Die in dieser Arbeit präsentierten Ergebnisse zeigen dennoch, dass die Sauerstoffionen der Marsatmosphäre einen großen Teil zur Erosion der dem Mars zugewandten Seite von Phobos beitragen.

Im Bereich der Kernfusionsforschung untersucht diese Arbeit verschiedene experimentelle Methoden, um die Wasserstoffspeicherung im Reaktorwandmaterial Wolfram zu messen. Dafür wurde zuerst eine nukleare Reaktionsanalyse mit Stickstoff-15-Ionen zur Wasserstofftiefenprofilierung in einem Wolframfilm eingesetzt. Dabei wurde festgestellt, dass die Stickstoff-15-Bestrahlung das Speicherungsverhalten der Probe signifikant beeinflusst und Probenbereiche, welche zuvor mit Stickstoff-15 untersucht worden waren, keine Oberflächenveränderungen durch gasgefüllte Blasen aufwiesen. Diese Beobachtungen konnten durch zusätzliche Materialdefekte, die durch den Stickstoff-15-Ionenstrahl erzeugt worden waren, erklärt werden, da sich der Wasserstoff in diesen Defekten anlagert, anstatt Gasblasen zu bilden. Diese Resultate sind nicht nur für die experimentelle Untersuchung von Wasserstoffspeicherung mit Ionenstrahlanalytik an sich relevant, sondern auch für kondensierte Wolframschichten in einem Fusionsreaktor, da neutroneninduzierte Defekte die Speicherung von Wasserstoff in solchen Schichten stark beeinflussen könnten. Eine zweite Ionenstrahlanalyse-methode, die elastische Rückstreuung, erwies sich als besser geeignet, um Deuteriumtiefenprofile in einer Wolframprobe zu messen. Sowohl Wasserstoff- als auch Deuteriumkonzentrationen können dabei in verschiedenen Tiefen zur selben Zeit gemessen werden, was zusätzliche Einblicke in die Speicherung und das Ausgasen der verschiedenen Wasserstoffisotope ermöglicht. Das wird in dieser Arbeit für das Beispiel der Deuteriumimplantation in Wolfram

demonstriert und die elastische Rückstredetektion wird auch in Zukunft ein wichtiges Werkzeug für eine Vielzahl ähnlicher Untersuchungen darstellen.

Im Rahmen dieser Dissertation konnten neue Erkenntnisse auf dem Gebiet der Ionen-Festkörper-Wechselwirkung in den Bereichen Weltraumverwitterung und Plasma-Wand-Wechselwirkung erzielt werden. Die Verhalten von Zerstäubung und Wasserstoffspeicherung wurden sowohl experimentell als auch numerisch untersucht, um das Verständnis der relevanten ioneninduzierten Effekte zu verbessern. Sowohl die präsentierten Experimente als auch die Berechnungen mit dem Simulationsprogramm SDTrimSP, die in dieser Arbeit vorgestellt werden, können sicherlich einen Anschlusspunkt für zukünftige Untersuchungen in den Planetenwissenschaften sowie in der Kernfusionsforschung darstellen.

List of Publications

Publications as First Author

- **P. S. Szabo**, H. Biber, N. Jäggi, M. Wappl, R. Stadlmayr, D. Primetzhofer, A. Nennung, A. Mutzke, J. Fleig, K. Mezger, H. Lammer, A. Galli, P. Wurz and F. Aumayr
Experimental Insights into Space Weathering of Phobos: Laboratory Investigation of Sputtering by Atomic and Molecular Planetary Ions
Journal of Geophysical Research: Planets **125** (2020) e2020JE006583.
<https://doi.org/10.1029/2020JE006583>
- **P. S. Szabo**, H. Biber, N. Jäggi, M. Brenner, D. Weichselbaum, A. Niggas, R. Stadlmayr, D. Primetzhofer, A. Nennung, A. Mutzke, M. Sauer, J. Fleig, A. Foelske-Schmitz, K. Mezger, H. Lammer, A. Galli, P. Wurz and F. Aumayr
Dynamic Potential Sputtering of Lunar Analog Material by Solar Wind Ions
The Astrophysical Journal **891** (2020) 100.
<https://doi.org/10.3847/1538-4357/ab7008>
- **P. S. Szabo**, R. Chiba, H. Biber, R. Stadlmayr, B. M. Berger, D. Mayer, A. Mutzke, M. Doppler, M. Sauer, J. Appenroth, J. Fleig, A. Foelske-Schmitz, H. Hutter, K. Mezger, H. Lammer, A. Galli, P. Wurz and F. Aumayr
Solar wind sputtering of wollastonite as a lunar analogue material - Comparisons between experiments and simulations
Icarus **314** (2018) 98-105.
<https://doi.org/10.1016/j.icarus.2018.05.028>

Publications as Co-Author

- K. Kantre, **P. S. Szabo**, M. V. Moro, C. Cupak, R. Stadlmayr, L. Zendejas Medina, F. Aumayr and D. Primetzhofer
Combination of in-situ ion beam analysis and thermal desorption spectroscopy for studying deuterium implanted in tungsten
submitted to Physica Scripta

- N. Jäggi, A. Galli, P. Wurz, H. Biber, **P. S. Szabo**, J. Brötzner, F. Aumayr and K. Mezger
Creation of Lunar and Hermean analogue mineral powder samples for solar wind irradiation experiments and thermal infrared spectra analysis
Icarus **365** (2021) 114492.
<https://doi.org/10.1016/j.icarus.2021.114492>
- R. Stadlmayr, **P. S. Szabo**, H. Biber, H. R. Koslowski, E. Kadletz, C. Cupak, R. A. Wilhelm, M. Schmid, C. Linsmeier and F. Aumayr
A high temperature dual-mode quartz crystal microbalance technique for erosion and thermal desorption spectroscopy measurements
Review of Scientific Instruments **91** (2020) 12.
<https://doi.org/10.1063/5.0012028>
- H. Biber, **P. S. Szabo**, N. Jäggi, M. Wallner, R. Stadlmayr, A. Niggas, M. V. Moro, D. Primetzhofer, A. Nennung, A. Mutzke, J. Fleig, A. Foelske-Schmitz, K. Mezger, H. Lammer, A. Galli, P. Wurz and F. Aumayr
Solar wind Helium ion interaction with Mg and Fe rich pyroxene as Mercury surface analogue
Nuclear Instruments and Methods in Physics Research Section B **480** (2020) 10.
<https://doi.org/10.1016/j.nimb.2020.07.021>
- R. Stadlmayr, **P. S. Szabo**, D. Mayer, C. Cupak, W. Möller and F. Aumayr
Erosion of iron-tungsten model films by deuterium ion irradiation: a benchmark for TRI3DYN
Physica Scripta **T171** (2020) 014021.
<https://doi.org/10.1088/1402-4896/ab438f>
- R. Stadlmayr, **P. S. Szabo**, D. Mayer, C. Cupak, T. Dittmar, L. Bischoff, S. Möller, M. Rasinski, R. A. Wilhelm, W. Möller and F. Aumayr
Sputtering of Nanostructured Tungsten and Comparison to Modelling with TRI3DYN
Journal of Nuclear Materials **532** (2020) 152019.
<https://doi.org/10.1016/j.jnucmat.2020.152019>
- R. Stadlmayr, **P. S. Szabo**, B. M. Berger, C. Cupak, R. Chiba, D. Blöch, D. Mayer, B. Stechauner, M. Sauer, A. Foelske-Schmitz, M. Oberkofler, T. Schwarz-Selinger, A. Mutzke and F. Aumayr
Fluence dependent changes of surface morphology and sputtering yield of iron: comparison of experiments with SDTrimSP-2D
Nuclear Instruments & Methods in Physics Research Section B **430** (2018)

42-46.

<https://doi.org/10.1016/j.nimb.2018.06.004>

- B. M. Berger, **P. S. Szabo**, R. Stadlmayr, and F. Aumayr
Sputtering measurements using a quartz crystal microbalance as a catcher
Nuclear Instruments and Methods in Physics Research Section B 406 (2017)
533-537.
<https://doi.org/10.1016/j.nimb.2016.11.039>

Contributions to International Conferences and Seminars as First Author

Invited Talks

- **P. S. Szabo**
Sputtering of Planets and Moons by Ion Impact
XXXII International Conference on Photonic, Electronic and Atomic Collisions (ViCPEAC 2021), Virtual Meeting (upcoming)
- **P. S. Szabo**
Sputtering of Mercury and Moon Analogues by Solar Wind Ions
24th International Conference on Ion-Surface Interactions 2019 (ISI-2019), Moscow, Russia (19.8.2019)

Short Oral Presentations

- **P. S. Szabo**
Real-time depth profiling of D in W during Thermal Desorption Spectroscopy with in-situ Elastic Recoil Detection Analysis
18th International Conference on Plasma-Facing Materials and Components for Fusion Applications (PFMC-18), Virtual Meeting (upcoming)
- **P. S. Szabo**
Experimental Investigation of the Space Weathering of Phobos by Planetary Oxygen Ions
52nd Lunar and Planetary Science Conference (LPSC2021), Virtual Meeting (19.3.2021)
- **P. S. Szabo**
Experimental Insights into Space Weathering of the Martian Moon Phobos

1st Symposium on Ion-Solid and Atomic Collisions (ISAAC 2020), TU Wien, Vienna, Austria (23.09.2020)

- **P. S. Szabo**

Interaction of Ions with the Surfaces of Planets and Moons

1st Symposium on Ion-Solid and Atomic Collisions (ISAAC 2020), TU Wien, Vienna, Austria (23.09.2020)

- **P. S. Szabo**

Experimental Investigation of Sputtering on Phobos by Atomic and Molecular Ions in the Martian Wake

Europlanet Science Congress 2020 (EPSC 2020), Virtual Meeting (21.9.2020)

- **P. S. Szabo**

Solar Wind Sputtering Investigations on Planetary Mineral Analogues

33rd Symposium on Surface Science 2020 (3S20), St. Christoph, Austria (4.3.2020)

- **P. S. Szabo**

Solar Wind Sputtering of Planetary Mineral Analogues

23rd International Workshop on Inelastic Ion-Surface Collisions (IISC-2019), Matsue, Japan (20.11.2019)

- **P. S. Szabo**

Potential Sputtering Experiments on Mineral Targets Relevant for the Lunar Surface

European Geosciences Union General Assembly 2019 (EGU 2019), Vienna, Austria (09.04.2019)

- **P. S. Szabo**

Sputtering Simulations of Rough Plasma-Facing Surfaces

5th Fusion Day, Vienna, Austria (16.11.2018)

- **P. S. Szabo**

Potential Sputtering of CaSiO₃ by Solar Wind Ions

19th International Conference on the Physics of Highly Charged Ions (HCI 2018), Lisbon, Portugal (04.09.2018)

- **P. S. Szabo**

Sputtering of Wollastonite

22nd International Workshop on Inelastic Ion Surface Collision (IISC-2017), Dresden, Germany (18.9.2017)

Poster Presentations

- **P. S. Szabo**, H. Biber, N. Jäggi, M. Wappl, R. Stadlmayr, D. Primetzhofer, A. Nennung, A. Mutzke, J. Fleig, K. Mezger, H. Lammer, A. Galli, P. Wurz and F. Aumayr
Quantifying Space Weathering of Phobos by Martian Planetary Oxygen Ions
European Geosciences Union General Assembly 2021 (EGU 2021), Virtual Meeting (19.4.2021)
- **P. S. Szabo**, H. Biber, N. Jäggi, M. Wappl, R. Stadlmayr, D. Primetzhofer, A. Nennung, A. Mutzke, J. Fleig, K. Mezger, H. Lammer, A. Galli, P. Wurz and F. Aumayr
Laboratory Experiments on the Space Weathering of Phobos by Planetary Oxygen Ions
43rd COSPAR Scientific Assembly (COSPAR 2021), Sydney, Australia (Hybrid Virtual Meeting) (31.1.2021)
- **P. S. Szabo**, K. Kantre, M. V. Moro, C. Cupak, R. Stadlmayr, L. Zendejas Medina, K. Schmid, D. Primetzhofer and F. Aumayr
In-situ Investigation of Deuterium Retention in Tungsten with Ion Beam Analysis and Thermal Desorption Spectroscopy
24th International Conference on Plasma Surface Interactions in Controlled Fusion Devices (PSI-24), Virtual Meeting (25.1.2021)
- **P. S. Szabo**, H. Biber, N. Jäggi, M. Brenner, D. Weichselbaum, M. Wappl, M. V. Moro, A. Niggas, R. Stadlmayr, D. Primetzhofer, A. Nennung, A. Mutzke, M. Sauer, J. Fleig, A. Foelske-Schmitz, K. Mezger, H. Lammer, A. Galli, P. Wurz and F. Aumayr
Combining Experiments and Modelling to Understand the Role of Potential Sputtering by Solar Wind Ions
European Geosciences Union General Assembly 2020 (EGU 2020), Virtual Meeting (8.5.2020)
- **P. S. Szabo**, R. Chiba, H. Biber, R. Stadlmayr, B. M. Berger, D. Meyer, A. Mutzke, M. Doppler, M. Sauer, J. Appenroth, A. Galli, J. Fleig, A. Foelske-Schmitz, H. Hutter, H. Lammer, K. Mezger, P. Wurz, and F. Aumayr
Sputtering of Wollastonite by H and Ar ions
10th International Symposium on Swift Heavy Ions in Matter & 28th International Conference on Atomic Collisions in Solids (SHIM-ICACS 2018), Caen, France (3.7.2018)

- **P. S. Szabo**, R. Chiba, H. Biber, R. Stadlmayr, B. M. Berger, D. Meyer, A. Mutzke, M. Doppler, M. Sauer, J. Appenroth, A. Galli, J. Fleig, A. Foelske-Schmitz, H. Hutter, H. Lammer, K. Mezger, P. Wurz, and F. Aumayr
Experimental and simulated solar wind sputtering of lunar analogue material
European Geosciences Union General Assembly 2018 (EGU 2018), Vienna, Austria (12.4.2018)
- **P. S. Szabo**, B. M. Berger, R. Chiba, R. Stadlmayr, A. Galli, P. Wurz, and F. Aumayr
A new Setup for Experimental Investigations of Solar Wind Sputtering
European Geosciences Union General Assembly 2017 (EGU 2017), Vienna, Austria (27.4.2017)
- **P. S. Szabo**, B. M. Berger, R. Stadlmayr, A. Galli, H. Lammer, P. Wurz, and F. Aumayr
A new setup for sputtering experiments with Mercury and Moon analogues
12th European Conference on Atoms, Molecules and Photons 2016 (ECAMP 12), Frankfurt, Germany (7.9.2016)

Invited Seminar Talks

- **P. S. Szabo**
Experimental Investigations on the Ion Sputtering of Planetary Surfaces
CSH/WP Colloquium, University of Bern, Bern, Switzerland (07.10.2020)
- **P. S. Szabo**
Sputtering of Mercury and Moon Analogue Material by Solar Wind Ions
Seminar for Applied Physics, TU Wien, Vienna, Austria (23.10.2018)

List of Supervised Students

Herbert Biber

Master Thesis: *Sputtering investigations of wollastonite using solar wind ions* (2018)

Project Thesis: *Determination of the angular dependent mass removal rate on wollastonite using hydrogen ions as projectiles* (2018)

David Weichselbaum

Bachelor Thesis: *Experimental sputtering of wollastonite using argon and helium-3 ions* (2019)

Matthias Brenner

Bachelor Thesis: *Difference in Sputtering Yield between $^3\text{He}^+$ and $^3\text{He}^{2+}$ on Wollastonite due to Potential Sputtering* (2019)

Markus Wappl

Project Thesis: *Sputtering effects of oxygen ions on augite* (2020)

Benedikt Holter

Project Thesis: *Measuring sputter yields of Mercury analogues at different temperatures with a QCM* (2021)

Jona Mangold

Bachelor Thesis (ongoing)

Julian Pichler

Bachelor Thesis (ongoing)

Contents

Abstract	iii
Kurzfassung	v
List of Publications	ix
Contributions to International Conferences and Seminars as First Author	xiii
List of Supervised Students	xvii
1 Introduction and Motivation	1
2 Theory and State of Research	5
2.1 Ion-Solid Interaction and Sputtering	5
2.1.1 Energy Loss	5
2.1.2 Sputtering	8
2.2 Existing Research on Sputtering of Planetary Surfaces	12
2.3 Existing Research on H Retention	14
3 Methods	15
3.1 Experimental Methods	15
3.1.1 Experimental Setups	15
3.1.2 Quartz Crystal Microbalance (QCM)	25
3.1.3 Ion Beam Analysis for H Isotope Retention	36
3.1.4 Thermal Desorption Spectroscopy (TDS)	38
3.1.5 Sample Preparation and Analysis	39
3.2 Theoretical Methods: Simulations with BCA-Codes	44
3.2.1 The Binary Collision Approximation (BCA)	45
3.2.2 SRIM	47
3.2.3 SDTrimSP	47
4 Results: Sputtering of Lunar and Hermean Analogs by Solar Wind Ions	49
4.1 Introduction	49

4.2	Sample Preparation Parameters and Analysis Results	50
4.3	Kinetic Sputtering	53
4.3.1	Kinetic Sputtering by Ar ⁺ from Experiment and Modeling	54
4.3.2	Sputtering by H ⁺ Ions	60
4.3.3	Irradiations with ⁴ He ⁺ and ³ He ⁺ Ions	65
4.4	Potential Sputtering	67
4.4.1	Irradiations with ³ He ²⁺ Ions	67
4.4.2	Irradiations with Ar ^{q+} Ions	70
4.4.3	Potential Sputtering Model	74
4.5	Conclusions for Solar Wind Sputtering	79
4.6	Discussion and Outlook	82
5	Results: Sputtering of Phobos by Martian Atmospheric Ions	85
5.1	Introduction	85
5.2	Sample Preparation Parameters and Analysis Results	88
5.3	Sputtering by Atomic Oxygen Ions	90
5.3.1	Measurement Results	90
5.3.2	Discussion	92
5.4	Sputtering by Molecular Oxygen Ions	98
5.5	Contributions from other Molecular Ions	99
5.5.1	Measurements with C ⁺ and CO ₂ ⁺ ions	99
5.5.2	Simulations of Sputtering by Molecular Ions	101
5.6	Conclusions for the Sputtering of Phobos	104
5.6.1	Sputtering by Planetary O ions	104
5.6.2	Potential Sputtering by He ²⁺ Ions	107
5.7	Conclusions and Outlook	108
6	Results: Retention and Release of Hydrogen Isotopes in Tungsten	109
6.1	NRA of H-Implanted W Samples	109
6.1.1	Sample Preparation and Analysis	110
6.1.2	Experimental Procedure	110
6.1.3	Results	111
6.1.4	Discussion	115
6.1.5	Conclusions	122
6.2	ERDA and TDS of D-implanted W Samples	123
6.2.1	Sample Preparation and Analysis	123
6.2.2	Experimental Procedure	124
6.2.3	Results	124
6.2.4	Discussion	126

6.3 Conclusions and Outlook	130
7 Conclusion and Outlook	133
Bibliography	137
List of Figures	155
List of Tables	159
List of Abbreviations	161
Danksagung	165

Introduction and Motivation

The interaction of ions with solids has been an extensively investigated field for several decades. Achieving an understanding of how ions behave upon impact and how surface and bulk of the target are affected has been driven by both applications and natural phenomena. Ions are an important tool for material modification and thin-film growth, but have also become essential for material analysis at a wide range of different energies. Furthermore, the interaction of ions with planetary surfaces is an important process in the solar system that continuously changes the surfaces of many planetary bodies. Major challenges also arise in nuclear fusion reactors when plasma ions interact with the reactor walls.

This thesis aims to investigate effects related to ion-solid interaction for the two topics of space weathering and nuclear fusion. Both new experimental and theoretical approaches are applied to gain new insights into the occurring processes, also with the aim of providing new techniques that will improve further understanding from experiments in the future.

Space weathering currently represents an important research topic in planetary science as it strongly influences the surfaces of most objects in the solar system. Planets, moons and asteroids that are not shielded by a thick atmosphere are vulnerable to precipitation by ions, but also to impacts from micrometeorites or electron- and photon-stimulated desorption processes (see Figure 1.1) [1, 2]. Over the past billion years, this has led to continuous modification of those planetary surfaces, where especially darkening and spectral reddening has been observed [3]. Furthermore, emitted surface atoms can form thin exospheres around the moons and planets, which allow remote insights into the compositions of their surfaces [4, 5]. Such investigations have been an important part of several space missions, among them the recently launched ESA satellite BepiColombo heading for Mercury. A significant part of these planetary exospheres, especially for refractory rock-forming elements, originates from sputtering by ions of the solar wind, which is made up of about 96% H^+ , 4% He^{2+} and a minor part of multiply charged heavier ions [6]. A complete understanding of the fundamental sputtering effects is therefore necessary for an

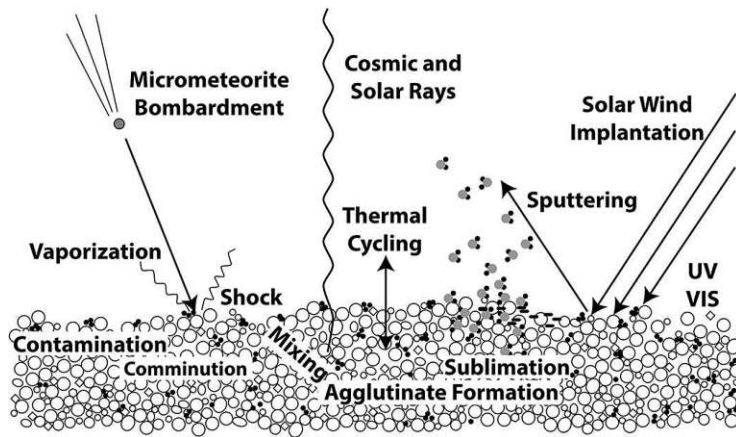


Fig. 1.1: An overview of the effects that occur on a planetary surface due to space weathering. Image taken from [8].

accurate modeling of the exosphere formation. Many investigations have so far only focused on the sputtering by H^+ ions and several models base the used sputtering inputs purely on simulation results. This thesis aims to expand sputtering research towards other ion species and especially focuses on the potential sputtering by multiply charged ions [7], which has not yet been included in any conventional simulation programs. Additionally, the space weathering of the Martian moon Phobos is examined in more detail. Here sputtering by O ions from the Martian atmosphere plays a decisive role, which is investigated experimentally for the first time.

Nuclear fusion is a very promising candidate for finding a reliable source of renewable energy that can contribute to satisfying future energy requirements. It is based on creating deuterium-tritium fusion reactions, which can only be realized in the high temperatures of a plasma. In the commonly used Tokamak and Stellarator reactor principles, this plasma is confined in a magnetic field, but cannot be withheld from the wall completely. Finding suitable wall materials for the reactor that can withstand high temperatures and bombardment by charged particles represents one of the major challenges for current test reactors as well as for future fusion power plants. Ions from the plasma sputter wall material, which causes both erosion and radiation losses due to bremsstrahlung and line radiation effects from sputtered wall atoms entering the plasma. Furthermore, the implantation and retention of H isotopes in plasma-facing components is an important factor for the efficient operation of a fusion reactor and represents a critical parameter for the suitability of potential wall materials. For all these effects, ion-solid interaction plays an essential role in the overall complex plasma-wall-interaction process (see Figure 1.2). The present thesis

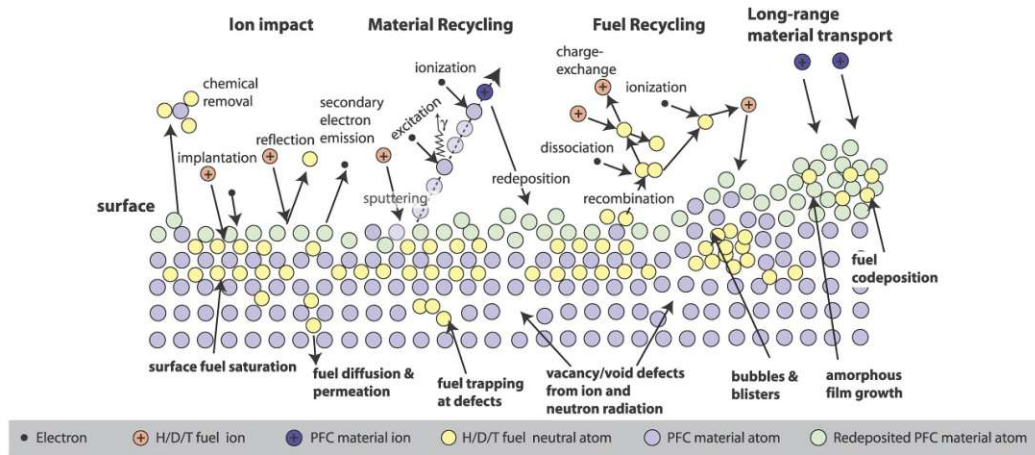


Fig. 1.2: A compilation of the relevant processes for the interaction of plasma ions with plasma-facing components (PFCs) in a nuclear fusion reactor. Image adapted from [9].

aims to improve the understanding of these effects by exploring combined-method approaches with Ion Beam Analysis (IBA) as tools for investigating hydrogen isotope retention.

This thesis is separated into seven chapters: Following this introductory chapter, the physical background of ion-solid interaction as well as current research on space weathering and plasma-wall interaction are outlined in Chapter 2. Chapter 3 introduces both experimental and theoretical methods that are applied throughout this thesis. Results on the sputtering of analogs for the surfaces of Moon and Mercury are then presented in Chapter 4, while Chapter 5 focuses on the sputtering investigations relevant for the space weathering of the Martian moon Phobos. Chapter 6 discusses fusion-relevant applications of IBA methods for new approaches of measuring H retention in W. Chapter 7 gives concluding remarks on the achieved results and outlines remaining challenges as well as upcoming research efforts in both space weathering and nuclear fusion research.

Theory and State of Research

The main topics of interest in this thesis, ion-induced space weathering and plasma wall interaction, underly the same fundamentals of ion-solid interaction. The most important effects are outlined in this chapter following summaries of the current state of research in both ion-induced space weathering and retention of H isotopes in reactor wall materials.

2.1 Ion-Solid Interaction and Sputtering

The research presented in this thesis covers several aspects of ion-solid interaction, but especially sputtering represents an important process. For ions with a kinetic energy in the keV range, the sputtering of atoms from the solid sample is a result from a collision cascade. This collision cascade is created as the ion loses its energy from a large number of nuclear collisions within several nm up to several 10s of nm, depending on ion species and energy. The following section gives an overview of the relevant effects that describe the interaction between an ion and a solid target.

2.1.1 Energy Loss

An energetic ion that hits a solid will penetrate the solid's surface and continuously lose its energy. The ion's kinetic energy strongly influences how this energy is transferred to atoms in the solid, which can occur via elastic collisions with target atoms (nuclear stopping) or via excitation and ionization (electronic stopping).

Stopping is generally described with the quantities of the stopping power $-dE/dx$ or the stopping cross section $S = 1/\rho \cdot (-dE/dx)$, where dE is the change of ion energy

during a distance dx and ρ is the target density. For the stopping cross section, it generally holds that (see [10])

$$S = \int T d\sigma(T) \quad (2.1)$$

with the energy transfer T during a collision and the scattering cross section σ . T is given from the masses of the scattering particles and the scattering angle as (see [10]):

$$T = E \cdot \frac{m_2}{m_1} \cdot \frac{\cos^2 \Phi}{\left(1 + \frac{m_2}{m_1}\right)^2} \quad (2.2)$$

Here E describes the ion energy, m_1 is the ion's mass, m_2 is the target atom's mass and Φ is the recoil scattering angle in the laboratory system. The scattering cross section σ can be derived from the differential cross section [10]:

$$\frac{d\sigma(\theta)}{d\omega} = \frac{p}{\sin \theta} \left| \frac{dp}{d\theta} \right| \quad (2.3)$$

Here p is the impact parameter, ω the solid angle and θ the scattering angle in the center-of-mass system.

Ultimately, both T and σ are determined by the scattering angle of the elastic collision, which can be calculated from the classical scattering integral [10]:

$$\theta = \pi - 2p \int_{R_{\min}}^{\infty} \frac{dR}{R^2 \sqrt{1 - \frac{V(R)}{E_{\text{cms}}} - \left(\frac{p}{R}\right)^2}} \quad (2.4)$$

Here R is the distance between the two scattering partners, R_{\min} denotes the distance of closest approach during the scattering event and E_{cms} describes the energy in the center-of-mass system. This integral requires an expression for the interaction potential $V(R)$. For example, inserting the pure coulomb interaction as $V(R)$ in equation 2.4 leads to the well-known Rutherford cross-section [10], and this can be applied, for example, for the case of light MeV ions in IBA. However, this approximation is not valid for ions in the keV range because the atoms' electron shells cannot be neglected for the interaction potential $V(R)$. Instead, a screened Coulomb potential is required because the colliding atoms stay far enough apart that the positive charge of the nuclei is at least partly compensated by the negative charge of the atoms' electrons. Common examples for such screened interaction potentials are the Ziegler, Biersack and Littmark (ZBL) potential [11] or the KrC potential [12]. These screened potentials are mostly based on the original approach

by Thomas and Fermi [13, 14], which consists of the Coulomb interaction multiplied with a screening function $\phi(R/a)$ [10]:

$$V(R) = \frac{1}{4\pi\epsilon_0} \frac{Z_1 Z_2 e^2}{R} \phi\left(\frac{R}{a}\right) \quad (2.5)$$

Here Z_1 and Z_2 describe the atomic numbers of the interacting atoms and a is a screening length, which determines above which distance the electrons screen the electric field of the protons in the nucleus. For the above stated examples of the ZBL and KrC potentials, ϕ is taken as the sum of several exponentials that cause interaction to diminish for larger distances.

By using screened interaction potentials, expressions for the nuclear stopping cross section S_n of an ion in matter can be derived [15, 16]. For the electronic stopping S_e caused by interaction with target electrons, different theories such as the Fermi-Teller model [17], the Firsov model [18] or the Lindhard-Scharff model [19] exist [10]. Evident differences between nuclear stopping and electronic stopping exist: Nuclear stopping is associated with large-angle scattering events, while electronic stopping usually is the sum of a large number of small angle scattering interactions that hardly change the direction of an ion in the solid. Furthermore, nuclear and electronic stopping have strongly deviating dependences on the ion's energy. Therefore, the total stopping cross section S is often approximated as the sum of two independent components from nuclear stopping S_n and electronic stopping S_e [10]:

$$S = S_n + S_e \quad (2.6)$$

Nuclear stopping is more prominent for slower ions, where longer interaction times and higher cross-sections for nuclear interaction allow a large number of such collisions with atoms from the target. Electronic stopping, on the other hand, dominates the interaction towards higher velocities, where more momentum transfer to electrons becomes possible. A typical comparison of nuclear and electronic stopping is shown for the example of I in Si in Figure 2.1, with I being a commonly used species in IBA. Results of a calculation with the program Stopping and Range of Ions in Matter (SRIM) are plotted [20]. Nuclear stopping (blue full line) is typically the dominant energy loss contribution at lower energies, while electronic stopping (red dashed line) increases proportional to the ion's velocity v . Above the Bragg peak of maximum energy loss, electronic stopping also decreases again.

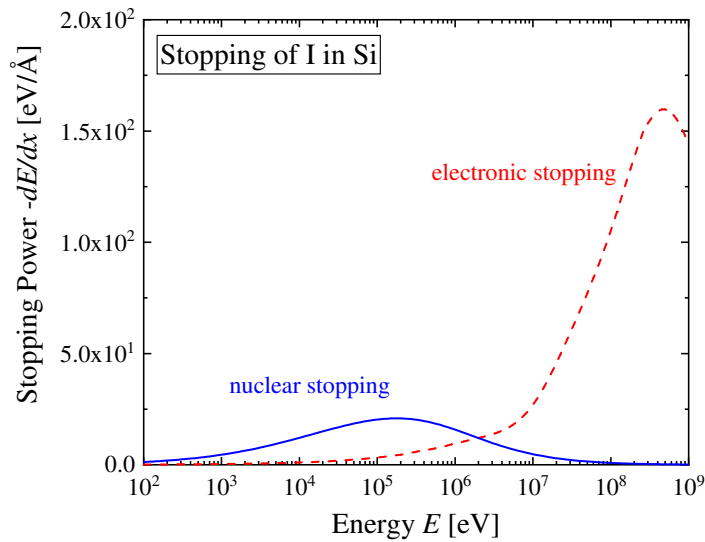


Fig. 2.1: This plot shows nuclear stopping (blue full line) and electronic stopping (red dashed line) for I ions in a Si target at energies between 100 eV and 1 GeV simulated with SRIM [20].

Figure 2.2 gives a different example of the energy loss of H (blue), He (orange) and Ar (green) projectiles in SiO₂ as calculated by SRIM. The left image in Figure 2.2 compares nuclear stopping (full lines) and electronic stopping (dashed lines). The right image gives the ions' projected ranges R_p in the target for the same systems, which represent the average depth beneath the surface where the ions get stopped. For the mostly investigated energy regions in the keV range, electronic stopping dominates for H, both contributions are comparable for He and for interactions with heavier ions such as Ar electronic stopping is negligible. The typical projected ranges are several nm for Ar and several 10 nm for H and He, which clearly illustrates that in these cases the ion-solid interaction processes happen in a region very close to the surface. These ions transfer their energy to the solid by a large number of scattering events, which causes a collision cascade to be formed. Most of the energy is ultimately transferred to phonons, but some target atoms receive enough energy to be emitted from the surface and to be sputtered.

2.1.2 Sputtering

Sputtering denotes the emission of atoms from a solid's surface following the impact of an energetic particle, mostly at energies from eV to several MeV [22]. **Kinetic sputtering** is a result from the collision cascade that forms in the near surface region,

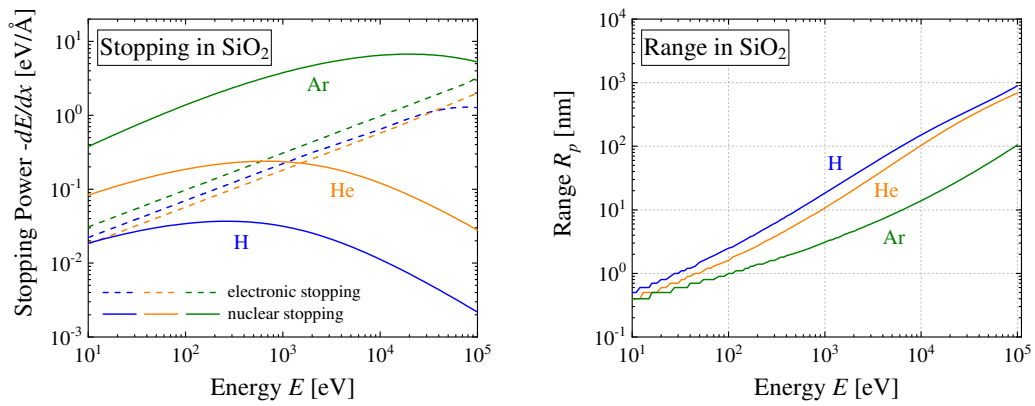


Fig. 2.2: Left: Stopping powers of H (blue), He (orange) and Ar (green) in SiO₂ from SRIM [20]. Full lines denote nuclear stopping, dashed lines represent electronic stopping. Right: The corresponding ranges for H, He and Ar in SiO₂ from SRIM.

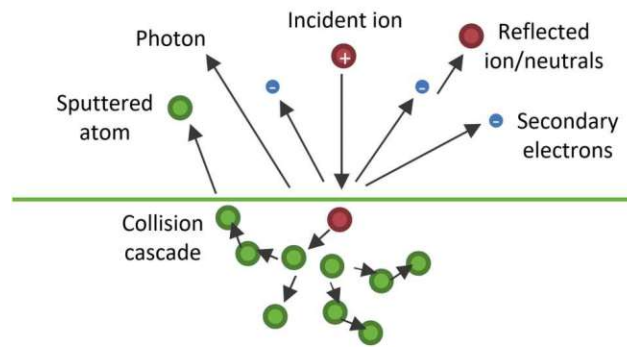


Fig. 2.3: This sketch illustrates common processes of ion solid-interaction. As a result of a collision cascade formed near the surface, enough energy can be transferred to target atoms for them to leave the surface and be sputtered. This image is adapted from [21].

as it is sketched in Figure 2.3. Enough energy first has to be transferred to target atoms to displace them from their lattice positions, corresponding to a displacement energy E_d , which is typically assumed to be in the range of several 10 eVs. In order to be sputtered, recoil atoms also have to be energetic enough to overcome the surface binding energy U_B , which is often approximated by the sublimation enthalpy of a few eV. Both effects lead to a threshold condition for the ion's energy for sputtering to occur, which is usually in the range of 10s of eV [23].

The amount of sputtered material is usually quantified by the **sputtering yield** Y , which denotes the number of sputtered atoms per ion, or especially in this thesis for the case of composite targets alternatively by the yield y describing the sputtered mass per ion. As kinetic sputtering is a product of elastic nuclear collisions, the sputtering yield strongly depends on the quantities that govern this collision process such as the ion mass, the target atom mass and the ion energy, but also the angle of incidence and the surface binding energy [24]. The sputtering yield is proportional to the inverse of the surface binding energy $1/U_B$ [24], which is at the same time a not very well known quantity, leading to challenges of sputtering simulations especially for composite targets. The dependence on the incidence angle stems from the lower ion range at oblique incidence, which leads to the collision cascade moving closer to the surface. Sigmund derived a $\cos^{-f} \alpha$ proportionality [24], with α being the incidence angle in regard to the surface normal. Currently established fitting formalisms apply a similar form for the angular dependence, but also take into account that above angles of incidence of around 60° the ion reflection becomes more frequent and the sputtering yield decreases again [16, 25]. Considering the energy dependence, the sputtering yield first increases with energy as more energy is transferred to recoil atoms. A maximum for the sputtering yield is reached at energies between several keV and several tens of keV, after which the increased energy cannot compensate shorter interaction times and longer ion ranges that lead to less energy being deposited close to the surface. An example for both the angular dependence and the energy dependence of the sputtering yield Y is shown in Figure 2.4 for Ar ions sputtering a W target. The plotted data represents the results from SDTrimSP simulations [26].

Another effect that comes into play for insulating targets and multiply charged ions is the so-called **potential sputtering** [7]. It especially is the major erosion effect for slow, highly charged ions where the ion's potential energy becomes higher than its kinetic energy. It should, however, not be neglected for multiply charged ions in the solar wind either, which will be one of the topics to be investigated in this

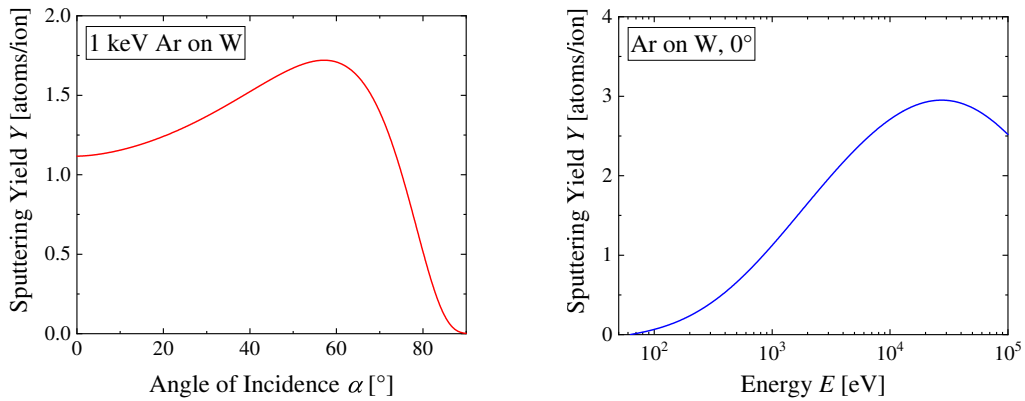


Fig. 2.4: Left: The dependence of the W sputtering yield on the angle of incidence for 1 keV Ar ions. Right: The dependence of the W sputtering yield under Ar bombardment on ion energy for irradiation under normal incidence. Sputtering yields are simulated with the program SDTrimSP and fitted with the formula proposed by Eckstein and Preuss (see section 4.3) [16, 26].

thesis. The origins of the potential sputtering effect had been long disputed, but existing experimental data was found to best agree with the defect mediated theory of potential sputtering [7, 27]. According to this theory, potential sputtering not only requires potential energy from the ion, but also an efficient electron-phonon coupling. The ion's potential energy leads to the self-trapping of electronic excitations in the solid, which ultimately leads to additional desorption of target atoms. In contrast to conventional kinetic sputtering, potential sputtering is currently not included in any established simulation programs, inputs on its effect therefore still require experimental data, which will be discussed later in this thesis.

For the special case of composite targets, which are especially relevant for space weathering in the form of planetary minerals, **preferential sputtering** also plays an important role. This effect is caused by a non-uniform sputtering of the constituent elements caused by varying energy transfer to the different atomic species as well as different surface binding energies. As it is sketched, in Figure 2.5, the ratio of sputtered elements will initially not be the same as the ratio of elements in the target. The preferential sputtering causes changes of the composition in the near-surface region as sputtered atoms originate from the top atomic layers [28]. In the shown example the blue atoms are enriched, which then changes the ratio of sputtered elements again. A steady state is reached, when the different elements are sputtered in the same relative abundance as they occur in the target's bulk, ultimately leading to a uniform erosion of the target.

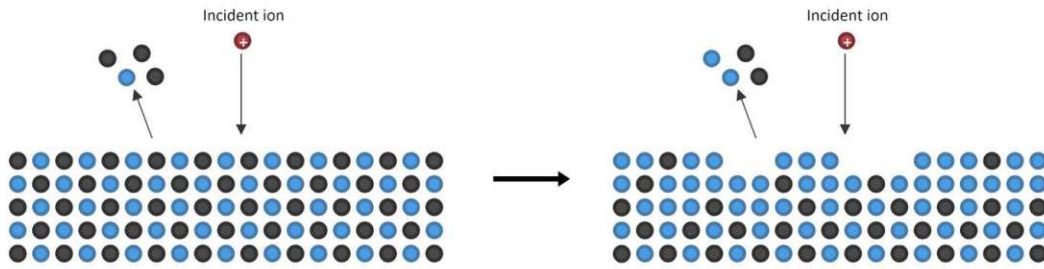


Fig. 2.5: Left: A composite target will initially not be uniformly sputtered. In this example, the sputtering yield for the black atoms is higher than for the blue atoms, even though their concentrations in the sample are equal. Right: Preferential sputtering leads to changes in the surface composition. The higher sputtering yield of the black atoms leads to an enrichment of blue atoms near the surface. In the steady state, an equilibrium is reached where the ratio of elemental sputtering yields corresponds to the ratio of elemental concentrations in the bulk. Assets for this image have been adapted from [21].

2.2 Existing Research on Sputtering of Planetary Surfaces

The main contribution to ion-induced space weathering of planets, moons and asteroids is caused by ions of the solar wind, which is a steady stream of ions that originates from the Sun. While a faster solar wind component is emitted over the pole regions of the Sun, planetary bodies are mostly affected by the so-called slow solar wind with velocities of around 400 km/s, which corresponds to specific kinetic energies E/m of 1 keV/amu. The solar wind mostly consists of 1 keV protons (96%) and 4 keV He^{2+} ions (4%) [6], but it also includes minor contributions from heavier, multiply charged ions such as C, O or Fe. During a coronal mass ejection event, these contributions from heavier ions have been observed as significantly increased and can therefore also contribute to the space weathering by the solar wind [29]. The flux of solar wind ions, about 10^{12} ions/m² at the Moon, is several orders of magnitude lower than the fluxes of typical laboratory ion beams. However, this is compensated by the long astronomical timescales that are relevant for the weathering of planetary bodies, which causes the solar wind to significantly contribute to the erosion of their surfaces.

Space weathering effects have often been investigated in regards to the optical changes of surfaces [30], mostly connected to the formation of nanophase Fe near the surface [1]. For solar wind sputtering of relevant materials, only little experimen-

tal data exists and several exosphere models rely on estimates or SRIM simulations for sputtering yields [31, 32, 33, 34]. They identify sputtering by ions of the solar wind as a key part for exosphere creation, especially for the emission of refractory material from the surface. However, due to a lack of experimental data and uncertainties in simulation inputs, the sputtering contribution is not well constrained.

Sputtering rates of planetary material and multi-component materials in general have been of early interest in sputtering research [35, 36]. Sputtering yields for SiO_2 , which is often used as a reference material, were determined at solar wind energies (1 keV/amu). Their yields of about 0.1 for He and about 1 for Ar irradiation were found by Betz and Wehner [36], which was later confirmed for Ar by Seah and Nunney [37]. Johnson and Baragiola [38] gave an overview of the different effects that occur for solar wind sputtering, which includes kinetic sputtering, preferential sputtering and as a result the change in surface composition, which is especially important for oxides. Dukes et al. [39] investigated the effect of H^+ and He^+ irradiation on olivine surfaces describing changes in composition and optical properties. Surface reddening was also found by Loeffler et al. for olivine under He^+ bombardment [40]. Preferential sputtering was further investigated by Dukes et al. for He^+ irradiation of tectosilicates, where preferential Na sputtering could be observed [41]. Meyer et al. investigated potential sputtering effects for lunar regolith simulant material, where increases for the relative O yield at higher ion charge states could be found, but no absolute yields were determined [42].

Recent efforts by Hijazi et al. focused on determining absolute sputtering yields for thin anorthite films ($\text{CaAl}_2\text{Si}_2\text{O}_8$) under H^+ and multiply charged Ar irradiation with a commercial microbalance setup [43]. Later, further investigations were performed by Hijazi et al. to derive experimental sputtering yields for He^+ and He^{2+} irradiation [44]. Physical sputtering yields were found to agree with SRIM simulations, while an increase by about a factor of 2 was found for He^{2+} ions compared to singly charged He. A model for sputtering of multiply-charged Ar ions was applied to calculate the potential contribution. This model was then applied for all solar wind ions, identifying H and He as the main sources of ion sputtering. However, apart from this work by Hijazi et al., sputtering experiments with analogs for planetary surfaces are still quite limited. The work presented in this thesis aims to bridge existing knowledge gaps to further quantify sputtering yields by solar wind ions, especially by multiply charged ions. For the first time, sputtering by planetary O ions is also investigated to assess their effect on space weathering of Phobos.

2.3 Existing Research on H Retention

Due to the multitude of challenges for plasma-facing components, several different materials have been considered for the use in nuclear fusion reactors. Experimental investigation of plasma-wall interaction in the recent years has focused on ITER-relevant wall materials such as W and Be [45], or steels that are in consideration for future use in the DEMO reactor [46]. The ITER reactor, which is under construction, will use a W divertor, but Be as a wall material. This setup has been tested at the JET reactor [47], where especially the improvement of fuel retention compared to previous carbon wall materials are underlined [48].

Still, the retention of H and D is not yet completely understood and continues to be an important topic of research. The complex scenario that has to be expected in a fusion reactor has been shown in the JET campaign with an ITER-like wall, where hydrogen isotopes, plasma-wall species and seeding gas ions all contribute to erosion, deposition and fuel retention. The trapping of H isotopes in wall material has been found to be massively material-dependent and has therefore been extensively investigated for both W and Be [49, 50]. Different trapping mechanisms in the bulk and in vacancies have been identified by using Thermal Desorption Spectroscopy (TDS) measurements and accompanying modeling efforts [51, 52, 53]. Current research in this area focuses on further fundamental understanding of retention of different H isotopes, exploring for example the effects of damages on the retention [54]. Another topic of interest is the combination of retention studies with IBA methods to get more insights of the retention behavior during an experiment [55]. This point is also explored in the present thesis, where further methods for in-situ IBA characterization of implanted H isotopes is tested.

Methods

This chapter introduces both experimental and numerical methods that have been used throughout the research presented in this thesis. First, the experimental setups at TU Wien for space weathering research and at Uppsala University for IBA measurements of H retention in W are described. Then the main used experimental approaches are presented with a strong focus on the Quartz Crystal Microbalance (QCM) technique. Sample preparation and analysis methods are also introduced, the concrete results are later described in chapters 4, 5 and 6 respectively. Finally, the codes SRIM and SDTrimSP, which are commonly used for ion-solid interaction simulations in this thesis, are also introduced.

3.1 Experimental Methods

3.1.1 Experimental Setups

TU Wien

Most of the experimental investigations presented in this thesis were performed at the Augustin Ion Beam Laboratory situated at the Institute of Applied Physics (IAP) at TU Wien. The experimental setup used for QCM measurements is included in Beamline 3 connected to the Electron Cyclotron Resonance Ion Source (ECRIS) SOPHIE. The schematics of this setup are shown in Figure 3.1.

Ion Source The setup is centered around the ECRIS, where gas is ionized by microwave-induced electron impact ionization [58]. By magnetically confining the ions in a plasma, multiple ionization steps become obtainable and ion beams of multiply charged ions with μA currents can be created. An ECRIS is thus well suited for performing sputtering experiments also with multiply charged ions. This possibility differentiates it from conventional sputter gun ion sources that mostly

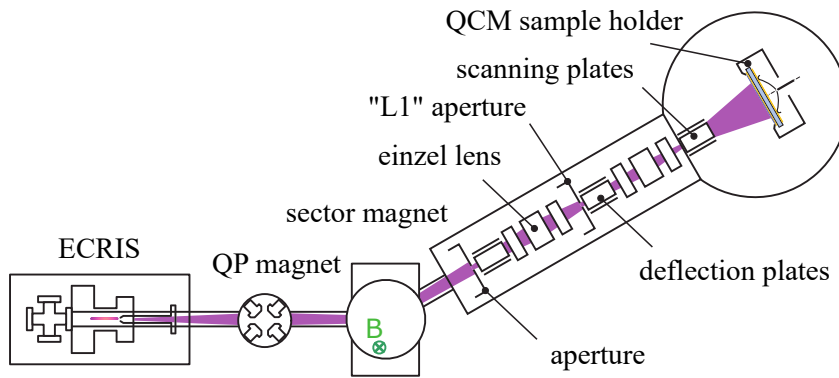


Fig. 3.1: The experimental setup for ion beam irradiations at TU Wien is sketched in this image. After ionization in the ECRIS, ions are extracted and focused by a quadrupole (QP) magnet system. The sector magnet is then used to steer the ion beam into the beamline, while simultaneously acting as a filter for the mass-over-charge-state ratio m/q . In the beamline, the ions are steered into the sample chamber by two sets of deflection plates. Two einzel lenses focus the beam, before it is then scanned uniformly across the QCM sample. Image adapted from [56].

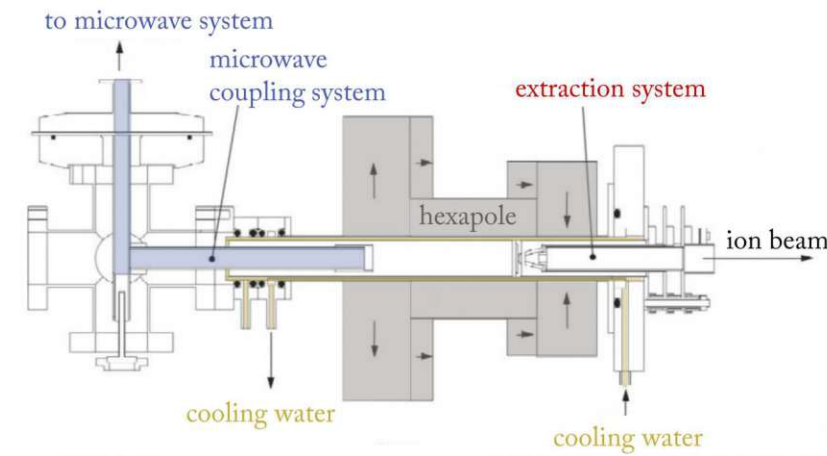


Fig. 3.2: This cross-section sketch shows the working principle of the ECRIS at TU Wien. Microwave radiation (blue) is used to heat the plasma that is confined in the hexapole magnetic configuration (grey). This allows multiple ionization of ions before they get accelerated by the extraction system. The whole source is water-cooled to prevent the permanent magnets from overheating during operation. Image taken from [57], where it was adapted from [58].

produce singly charged ions, but also from Electron Beam Ion Sources that provide much higher charge states at the cost of ion current [59]. In order to achieve magnetic confinement, the plasma chamber is equipped with four permanent magnet rings and a Halbach-type hexapole to create a combination of an axial and radial magnetic field (see the sketch in Figure 3.2) [58]. The plasma is heated by microwave-radiation generated from an oscillator and amplified with a solid state amplifier. The microwave frequency ω is chosen to correspond to the electron's cyclotron resonance in the magnetic field B :

$$\omega = \frac{e \cdot B}{m_e} \quad (3.1)$$

Here e represents the elementary charge and m_e the electron mass. The magnetic field setup of the ECRIS at TU Wien results in a nominal electron cyclotron frequency of 14.5 GHz, the actual operating frequency can be tuned between 12.75 and 14.5 GHz [58]. Electrons excited by the microwave radiation at this frequency repeatedly collide with gas atoms and ionize them, which creates more electrons that can further heat the plasma. Due to the magnetic confinement, ions are not immediately accelerated, but may remain in the plasma long enough to be further ionized following more collisions with electrons. This step-wise multiple ionization evidently depends on the number of electron impacts per gas atom before the ion hits the chamber wall or can leave the plasma volume accelerated by the electric field of the ion extraction system. The mean charge state \bar{q} is influenced by the microwave power P ($\bar{q} \propto P^{\frac{1}{3}}$ [60]) and the gas pressure inside the plasma chamber. Lowering the latter favors higher mean charge states \bar{q} due to an increased inelastic mean free path length for the electrons, which are then accelerated to higher impact energies in the plasma. Furthermore, loss to charge exchange reactions also becomes less probable [61]. Ion extraction is performed with a triode "accel-decel" system [61], where the plasma chamber is set on the positive acceleration voltage U , but ions are not directly accelerated to ground potential. Instead a suppressor electrode, typically at -100 V, is used for improving beam shaping and preventing Bremsstrahlung creation from electrons that would be accelerated into the ion source [61].

Using a turbomolecular pump, the ion source is kept at a base pressure in the low 10^{-7} mbar range, while operating pressures are in the 10^{-5} mbar range. The ion source has two thermostatically-controlled gas inlets, which allow gas mixing usually for improving ion source performance [58, 60, 61], but might also be used for replicating the H/He mixture of the solar wind in future experiments. Gas mixing is usually applied in an ECRIS by adding a lighter gas to the working gas with the

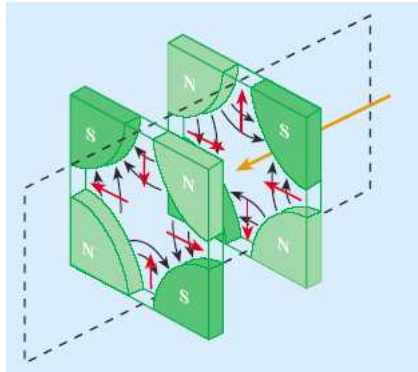


Fig. 3.3: This image shows the working principle of a quadrupole focusing magnet. The alternating array of magnetic north and south poles has a focusing effect in one plane and a defocusing effect in the respective perpendicular plane. The defocusing is combatted by using two subsequent quadrupole magnets that are rotated by 90° in respect to each other.
 Image taken from [63].

means of increasing the mean charge states of extracted ions. The lower mean charge states of light ions increase the confinement time of the multiply charged heavier ions. For this purpose, often He and O are used as mixing gases. For the experiments presented in this thesis, no mixing gas was used as the achieved ion beam currents were large enough for the application in sputtering experiments. The only recent tests of operating the ion source in gas mixing mode have been done by using ambient air, which did not lead to any significant improvements in the Ar^{8+} current [62]. Previous experiments with this ECRIS indicate, however, that He or O are better suited as a mixing gas and should be considered for future use [61]. For a more detailed description of the ion source SOPHIE as well as details on how further aspects such as the bias plate or tuning the microwave coupling system affect the source performance, also see [61].

Quadrupole Magnets After extraction from the ion source, the ion beam is focused using a set of two quadrupole focusing magnets. Such quadrupole magnets are a common device in accelerator physics for focusing an ion beam. The working principle is sketched in Figure 3.3: the quadrupole of two north and two south poles creates a magnetic field perpendicular to the ion beam path. Following the shape of the field lines from north to south pole (black arrows) and the Lorentz force $F_L = q \cdot (\vec{v} \times \vec{B})$ (red arrows), the magnetic field causes a focusing in one plane and a defocusing in the other. For this reason, two quadrupole magnets are used directly after each other, with the second one being rotated by 90° in respect to the first. In

doing so, a net focusing effect on the whole ion beam can be achieved.

Sector Magnet After focusing in the quadrupole magnets, the ion beam enters the sector magnet, from where different paths to the three beamlines are possible. The vertical magnetic field allows steering the beam in horizontal direction, but also acts as a filter. After extraction from the source, the ion beam will contain several charge states as well as ions from residual or mixing gases, which are unwanted for the experiment. These charge states or ion species can be separated in the sector magnet as long as their mass-over-charge-state ratio m/q is different. In the constant sector magnetic field, ions will perform a circular motion around the magnetic field lines, which ultimately results in a rotation of the ion beam direction by a certain angle ϕ . Different angles ϕ lead to the steering into the different beamlines of the setup. The angle ϕ is defined by the circular motion inside the sector field B , which can be characterized by the Larmor radius r_g :

$$r_g = \frac{m \cdot v}{q \cdot e \cdot B} \quad (3.2)$$

The ions' velocity v can be expressed by the acceleration voltage U , the charge state q , the elementary charge e and the ion mass m :

$$v = \sqrt{\frac{2 \cdot q \cdot e \cdot U}{m}} \Rightarrow r_g = \sqrt{\frac{2 \cdot m \cdot U}{q \cdot e}} \cdot \frac{1}{B} \quad (3.3)$$

For the ion beam to enter the beamline, a fixed Larmor radius r_g is required and the mass-over-charge-state ratio of the ion beam is then given by:

$$\frac{m}{q} = \frac{e \cdot B^2}{U} \cdot \frac{r_g^2}{2} \quad (3.4)$$

This relation also becomes evident in the used setup settings: Figure 3.4 shows an evaluation of 265 saved working points of different experiments that were used for ion beam irradiations at Beamline 3 since 2011. The mass-over-charge-state ratio m/q is here plotted over the ratio B^2/U (red dots) and a clear linear behavior is observed as calculated before. Some regularly used ion species are clearly visible, the examples of Ar^+ , Ar^{2+} and O^+ are given in the image. For B , the LabView control value that is entered for setting the sector magnetic field strength is used here instead of the actual measured magnetic field from the hall probe. The visible scattering is caused by the hysteresis of the magnet, slight deviations in the beam path depending on quadrupole magnet settings and the extended aperture size at

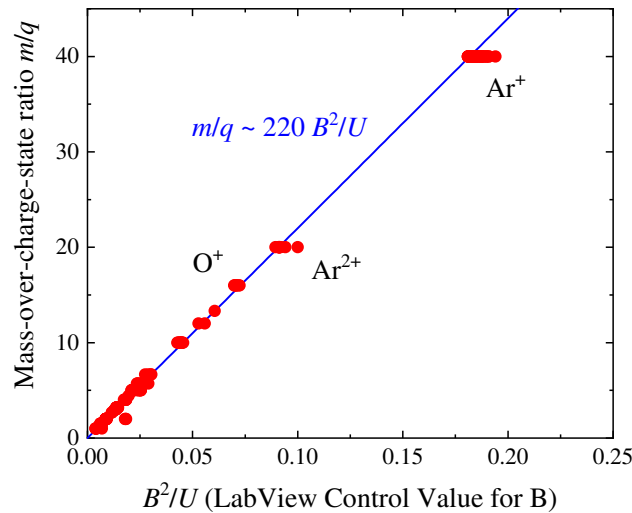


Fig. 3.4: This plot shows an analysis of past settings for ion beam irradiations at Beamline 3. The red dots represent the mass-over-charge-state ratio m/q plotted over the ratio B^2/U . The used settings clearly show the theoretically predicted proportionality of m/q to B^2/U from equation 3.4 (blue line).

the beamline entrance, allowing an extended range of B values. The observed trend in Figure 3.4 gives the following relation (blue line):

$$\frac{m}{q} = k \cdot \frac{B^2}{U} \quad (3.5)$$

Using the LabView control parameter for B , U in V and m in amu results in a value of $k \approx 220$. This can be used as a reference for future spectra and should also be very similar for Beamline 1 due to the mirrored geometry of both beamline's connection to the sector magnet.

Beamline After passing through the sector magnet, the ion beam enters the beamline. Directly at the beamline entrance, a Faraday Cup (FC) mounted on a pneumatically controlled manipulator is situated [64]. It can be moved into the ion beam's path to measure the ion beam current before optimizing it in sample chamber or recording a spectrum of different ion species or charge states by varying the sector magnetic field. The ion beam can then be steered and focused into the sample chamber using several sets of electrostatic deflection plates and two einzel lenses (see Figure 3.1). Between the two einzel lenses, an aperture ("L1", marked in Figure 3.1) is located where the beam current can also be measured. The current alignment of the beamline allows the ion beam to directly hit the L1 aperture using only the

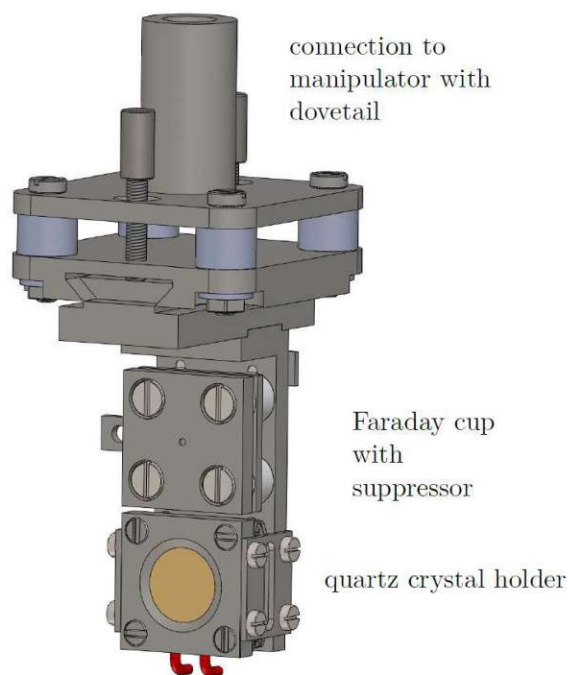


Fig. 3.5: This CAD model shows the structure of the QCM sample holder. The oscillating quartz is mounted in the bottom part of the holder, the segment above contains the FC for beam current measurements. The red segments represent the ohmic sample heating wire. This image is taken from [56].

sector magnet. As a result, the best practice for steering the ion beam into the sample chamber has been found to first maximize the ion beam onto the L1 aperture using the sector magnet and the quadrupole focusing magnets. Typically, currents in the lower 100 nA order can be achieved for Ar^+ and several μA for He^+ . Using the first set of deflection plate and the einzel lens, the current on the L1 aperture should then be minimized (typically to several nA) for the beam to be focused enough to pass through the aperture. Using the remaining set of deflection plates and the second einzel lens, the beam current in the sample holder FC can then be optimized. The focused ion beam is finally scanned across the sample using a set of scanning plates (1.6 kHz in one direction, 52 Hz in perpendicular direction [65]) to create a uniform beam profile across the whole QCM sample.

Sample Chamber In the sample chamber, the target holder for a QCM, which is shown in Figure 3.5 is situated. It contains a FC directly above the QCM to measure the ion beam current density exactly as it hits the sample. Recently, extensions

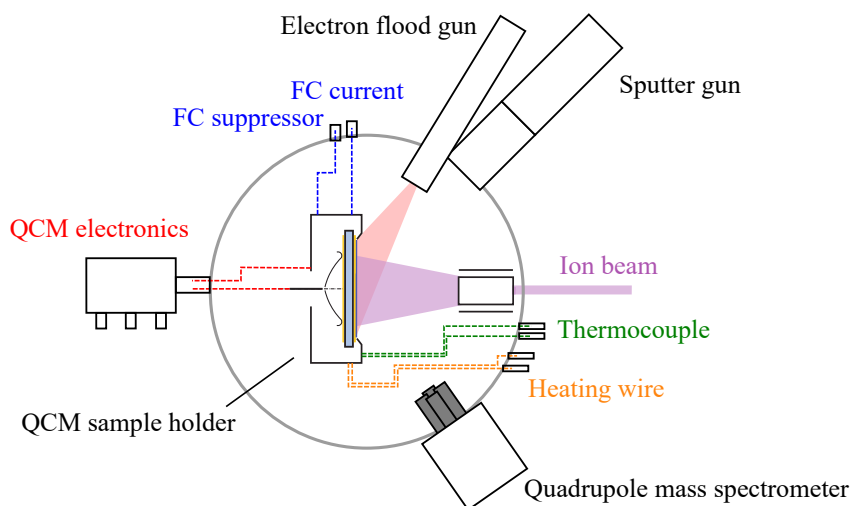


Fig. 3.6: This sketch shows the schematic structure and the components of the sample chamber. It is centered around the QCM sample holder that is shown in Figure 3.5. From the sample holder, several cables connect to outside of the vacuum chamber. This includes connectors for the QCM electronics (red), for FC current measurement as well as electron suppression (blue), for the heating wire (orange) and for the thermocouple (green). Several other components are connected to the sample chamber, such as an electron flood gun, a quadrupole mass spectrometer and a second sputter gun ion source. Parts of this sketch were adapted from [56].

to the established sample holder design have been made to include an additional sample slot for measurements with mineral pellets. The sample holder stage can be moved in all three directions controlled by stepper motors. This allows switching between the positions of the sample and the FC, which are placed directly above each other (see Figure 3.5). The motors are further used for automatically recording a laterally resolved beam profile. This is done before and after each measurement to check uniformity and stability of the ion beam current density. The sample holder is also mounted on a rotatable manipulator allowing measurements under angles of incidence up to about 70° with respect to the surface normal. The sample holder is further equipped with an ohmic heating wire enabling measurements at higher temperatures (red in Figure 3.5), and a K-type thermocouple for temperature measurements.

Figure 3.6 gives an overview of the main parts of the sample chamber setup, especially showing the different connectors to the sample holder. Furthermore, the sample chamber is also equipped with an electron flood gun for charge neutralization on insulating surfaces and a quadrupole mass spectrometer to measure the desorption of ions previously implanted in the target. Additionally, a second sputter

gun ion source has recently been installed and attached to the sample chamber under an angle of 45° in respect to the ion beam, which will be used for performing dual ion beam irradiations in the future.

The sample chamber is kept at ultra-high vacuum (UHV) conditions of pressures in the order of 10^{-10} mbar with an ion getter pump and a Ti sublimation pump. Similar to the whole vacuum system of the SOPHIE setup, the vacuum pumps are controlled via a programmable logic controller (PLC) that can be accessed over a central PC. The ion source, quadrupole magnets and sector magnet are controlled with a LabView program and most of the devices for operating experiments at the beamline have been made accessible with python programs, which allows remote access. This is used, for example, to automate the measurement of ion beam current profiles.

Uppsala University

The IBA experiments with fusion-relevant materials presented in this thesis were performed at the SIGMA (Set-up for In-situ Growth, Material modification and Analysis) chamber at Uppsala University [66]. This setup has previously been used for the investigation of in-situ grown photochromic films [67] and is now also applied for nuclear-fusion-relevant research [68]. Its schematics are shown in Figure 3.7: The SIGMA chamber allows the combination of in-situ material modification with IBA methods. For this purpose, it is connected to a 5 MV Pelletron Tandem Accelerator [69], which provides MeV ions (from the left in Figure 3.7) for the application in different analysis techniques such as Rutherford Backscattering Spectrometry (RBS), Elastic Recoil Detection Analysis (ERDA) or Nuclear Reaction Analysis (NRA). In the chamber, the sample holder is attached to a 5-axes goniometer, allowing movement in three translational and two rotational directions. Four different detectors (blue in Figure 3.7) allow IBA experiments: A rotatable Passivated Implanted Planar Silicon (PIPS) detector in backscattering direction allows RBS or Elastic Backscattering Spectrometry (EBS) measurements [70]. Another PIPS detector in forward scattering direction is used for ERDA and a Silicon-Drift Detector (SDD) is included for Particle-Induced X-ray Emission (PIXE) measurements. Furthermore, a High Purity Ge (HPGe) gamma detector can be positioned outside the viewport for $^1\text{H}(^{15}\text{N},\alpha\gamma)^{12}\text{C}$ NRA experiments to determine hydrogen profiles with precise depth resolution.

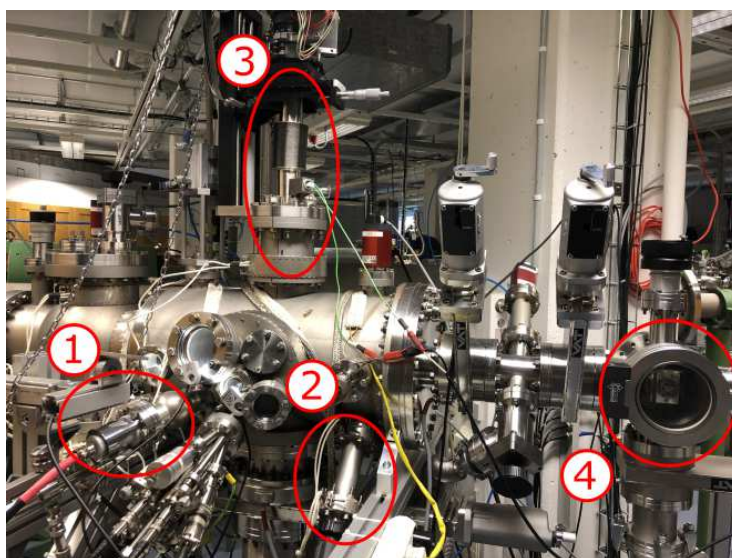
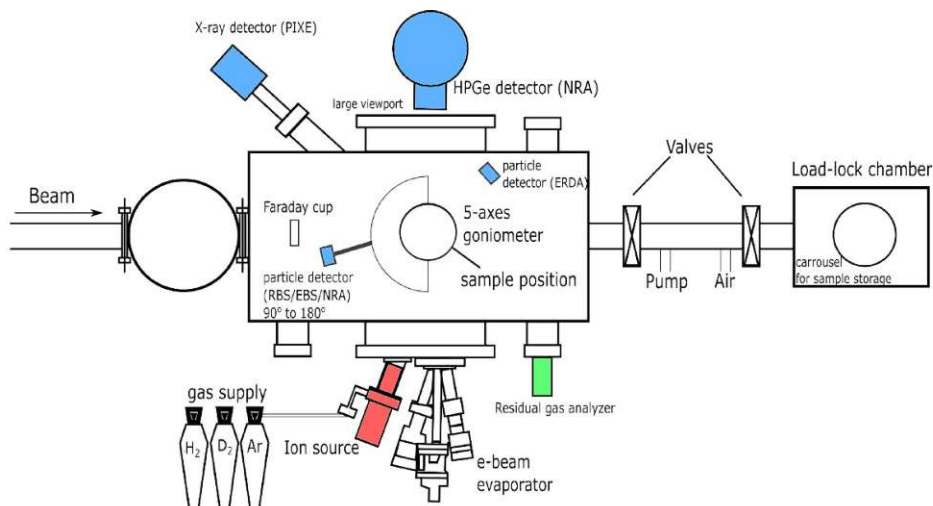


Fig. 3.7: Overview of the SIGMA setup at Uppsala University used for in-situ IBA experiments [66]. The chamber is connected to a 5 MV Pelletron Tandem Accelerator, providing an MeV ion beam necessary for IBA (here coming from the left). Using a sputter gun ion source (marked red in the sketch, (1) in the photo), sputtering and ion implantation can be performed. Available detectors (marked blue) allow subsequent in-situ analysis with a wide array of establish IBA techniques. These measurements can also be performed as the sample is heated by the included electron bombardment heating system and the desorbing gas is measured in a residual gas analyzer (marked green, (2)). In the chamber, the sample is mounted on a 5-axes goniometer that can be oriented depending on the required technique (3). Samples can be transferred into the chamber without ventilation via a load lock system (4). The sketch (upper image) was adapted from [66].

The SIGMA chamber also includes a Prevac IS40 extractor type ion source (red in Figure 3.7), which allows in-situ sputtering or the implantation of ions in the sample. Parallel monitoring of the sample's modification with IBA is possible during ion irradiation as well as during sample annealing. The goniometer is equipped with a filament for electron beam heating up to a temperature of about 1000 °C. As the sample is heated, the outgassing of previously implanted ions can then be monitored with a Residual Gas Analyzer (RGA) (green in Figure 3.7). At the time when the experiments presented in this thesis were performed, the used RGA did not allow mass-sweeping, meaning that only one mass-over-charge-state ratio m/q could be monitored.

3.1.2 Quartz Crystal Microbalance (QCM)

The main experimental technique for investigating ion-solid interaction in this thesis is the QCM, which is an established method for measuring ion-induced erosion in nuclear fusion research [65, 71, 72, 73] or potential sputtering [74, 75, 76]. QCM measurements are based on the mass dependent resonance frequency of an oscillating quartz and the high achievable precision of measuring this resonance frequency. This method can then be used to perform sputtering measurements on thin films deposited on top of such an oscillating quartz in real-time and in-situ, while the whole system is in vacuum. This represents a significant advantage over other experimental methods of determining sputtering yields: On one hand, it gives more insights than catching foils or ex-situ microbalance measurements [77, 78]. On the other hand, it also requires less costly equipment than determining sputtering yields from, for example, RBS analysis or even Scanning Tunneling Microscope (STM) measurements [79, 80].

In the following, the general working principles of sputtering experiments with a QCM are discussed at first. Afterwards, further aspects such as the effect of ion implantation on a QCM measurement or the QCM temperature dependence are discussed.

Measurement Principles for Sputtering Experiments

As mentioned above, the QCM technique is an established tool for sputtering measurements in the Atomic and Plasma Physics Group at IAP, but quartz crystals as microbalances have been used for several decades before. Its current applications are based on the formulation by Sauerbrey [81]: By applying an external voltage via two opposite electrodes, the piezoelectric quartz is excited into a thickness shear oscillation that creates a standing transversal wave. The resonance frequency f_Q is dependent on the thickness of the quartz and a sufficiently thin layer on top of the oscillating quartz influences it the same way a thicker quartz of the same mass would [81]. This then leads to a proportionality relation between changes of the resonance frequency Δf_Q and changes of the film mass Δm that is sometimes denoted as the "Sauerbrey equation" [81]:

$$\frac{\Delta f_Q}{f_Q} = -\frac{\Delta m}{m_Q} \quad (3.6)$$

Here m_Q represents the mass of the quartz.

Through the condition of uniform mass change, a QCM is suited for measuring its average mass change across its active area. For the SC-cut quartzes provided by KVG Quartz Crystal Technology GmbH that were used in the scope of this thesis, the lateral sensitivity on the mass change was measured: A radially symmetric gaussian shape was found in good agreement with theoretical predictions [82, 83]. In accordance with this calculation, the size of the quartz's circular active area was determined to have a diameter of 7 mm [65, 82]. Mass changes that occur outside of the active area do not cause a change of the quartz's resonance frequency. For this reason, the ion beam is scanned over the quartz surface during ion irradiation to cover the whole active area of the quartz. While a more focused ion beam would cause a more easily resolvable frequency change, the measurement would become extremely sensitive to beam shape and position.

In a sputtering measurement, the desired quantity is the sputtering yield Y , describing the number of sputtered atoms per irradiating ion, or alternatively for composite targets denoted as y describing the mass removal per ion. This mass removal per ion can be calculated from the mass change $\Delta m(\Delta t)$ during an irradiation time Δt and the number of ions $N_{\text{ions}}(\Delta t)$ hitting the target during the same time (see [84]):

$$y = -\frac{\Delta m(\Delta t)}{N_{\text{ions}}(\Delta t)} \quad (3.7)$$

The mass change can be expressed with equation 3.6 to include the measured frequency change $\Delta f_Q(\Delta t)$:

$$\Delta m(\Delta t) = -\frac{m_Q}{f_Q} \cdot \Delta f_Q(\Delta t) \quad (3.8)$$

The number of ions can be expressed with the ion beam current I , the ion charge state q and the elementary charge e as

$$N_{\text{ions}}(\Delta t) = \frac{\int I(t)dt}{q \cdot e} = \frac{I \cdot \Delta t}{q \cdot e} \quad (3.9)$$

assuming a temporally constant ion beam current I . As described above, given a large enough irradiated area, only mass changes on the active area of the quartz's oscillation A_Q are relevant. Therefore, also only the number of ions hitting the active area contribute to the measured mass change. The quartz mass $m_Q = \rho_Q \cdot d_Q \cdot A_Q$ can then be expressed as the product of quartz density ρ_Q , thickness d_Q and active area A_Q . Similarly the ion beam current $I = j \cdot A_Q$ can be written as the product of ion beam current density j and active area A_Q . The ion beam current density j can be obtained from measurements with the FC that is attached to the sample holder (see Figure 3.5). By moving the stepper motor-controlled manipulator, where the sample holder is mounted, a laterally resolved beam profile can be recorded. The before mentioned relations inserted into equation 3.7 gives the following expression where the active area A_Q crosses out:

$$y = q \cdot e \cdot \frac{1}{j} \cdot \frac{\Delta f_Q(\Delta t)}{\Delta t} \frac{\rho_Q \cdot d_Q}{f_Q} \quad (3.10)$$

If the sputtering yield is to be calculated in amu/ion, this leads to the following expression [84]:

$$y[\text{amu/ion}] = q \cdot \frac{1}{j} \cdot \frac{\Delta f_Q(\Delta t)}{\Delta t} \underbrace{\frac{\rho_Q \cdot d_Q \cdot e}{f_Q \cdot m_0}}_C \quad (3.11)$$

Here m_0 denotes the atomic mass unit and the quartz properties and natural constants can be combined into a factor C . For a mono-elemental sample, division by the target material's mass number m_i gives the sputtering yield Y in atoms/ion [84]:

$$Y[\text{atoms/ion}] = \frac{q}{m_i} \cdot \frac{C}{j} \cdot \frac{\Delta f_Q(\Delta t)}{\Delta t} \quad (3.12)$$

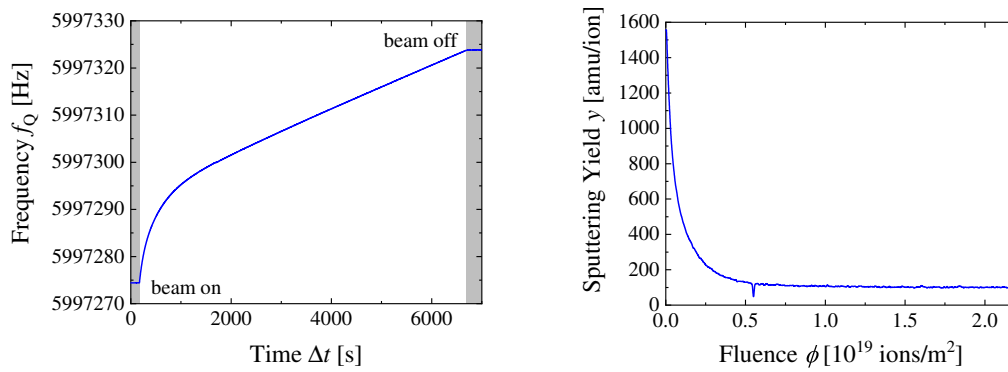


Fig. 3.8: These two figures show an example for a QCM measurement during sample cleaning of a CaSiO_3 layer with 2 keV Ar^+ ions under 60° . Left: The quartz frequency f_Q is plotted over time Δt and phases where the ion beam was turned off are marked in grey. After turning on the ion beam, the frequency increases as surface atoms are sputtered away. Right: The evaluated sputtering yield γ in amu/ion is plotted over fluence ϕ . The flattening of the frequency curve is connected to a decrease in the sputtering yield.

Sputtering yields from a QCM measurement can thus be obtained by combining two measurements of the ion beam current density j and the quartz's frequency slope $\Delta f_Q(\Delta t)/\Delta t$. Measurements with a good time resolution allow connecting changes of the slope over time to a fluence dependence of the sputtering yield. An example for such a QCM measurement can be seen in Figure 3.8, which shows a first cleaning irradiation of a wollastonite (CaSiO_3) sample after storage at air under 2 keV Ar^+ irradiation at 60° . The left image in Figure 3.8 shows the measurement of the quartz frequency f_Q over time Δt . Before and after the irradiation, the frequency drift was recorded (marked by the grey areas), which is negligible compared to the mass-change-induced frequency change in this example. When the ion beam is turned on, the frequency steeply increases corresponding to a mass decrease. After a sample is first inserted into vacuum, its top surface is still covered with loosely bound adsorbates, which explains the large amount of material being sputtered at the beginning of the irradiation. As the frequency change becomes flatter, the sputtering yield γ decreases. This is shown in the right image of Figure 3.8, where γ is plotted over the fluence ϕ , which denotes the number of ions that has hit the sample during the irradiation per area. When the contaminants are mostly sputtered away, the frequency change and sputtering yield become more stable and an actual sputtering yield for the irradiation of the sample can be determined.

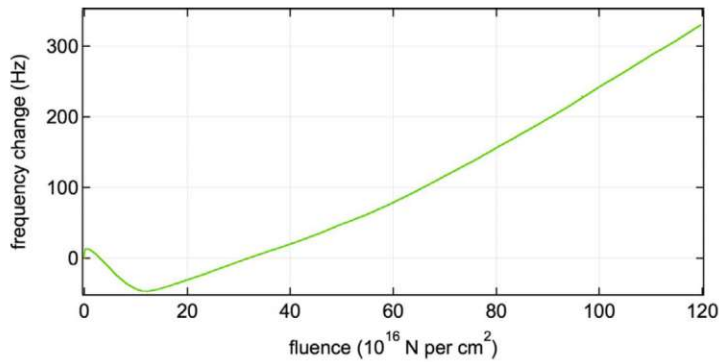


Fig. 3.9: This irradiation of a Be-coated QCM sample with 5 keV N_2 ions gives an example of an experiment, where both projectile implantation and sputtering play a role. Following a small initial increase, the frequency decreases due to a net mass increase: More weight is gained by implanted N than lost by sputtered Be. After the sample is saturated at a fluence of about $15 \cdot 10^{16}$ N/cm², sputtering overtakes as the more important mass-changing process and the frequency starts to increase. Figure taken from [85].

QCM Measurements of Ion Implantation

The mass dependence of the quartz frequency causes a possible combination of influences from mass decreases caused by sputtering and mass increase by ion implantation. This can be hindering in determining sputtering yields as the implantation coefficients are hard to estimate and likely show a significant fluence dependence. However, measuring both effects at the same time also represents a chance to get a more complete understanding of relevant ion-solid interactions [85, 86, 87, 88, 89]. Figure 3.9, shows an example for a such a measurement where both ion implantation and sputtering play an important role [85]. Here a Be-coated quartz sample is irradiated with 5 keV N_2^+ ions to investigate the interaction of seeding gas ions with fusion wall materials. The resulting frequency behavior is plotted over the ion fluence. Up until about 15×10^{16} N/cm², the frequency steadily decreases, which corresponds to a net mass increase due to N atoms being implanted into the Be layer. At some point, the Be within the ion implantation range (up to 20 nm according to simulations presented in [85]) becomes saturated and stopped N ions quickly outgas again. After this saturation, the mass decrease by sputtering takes over as the dominant contribution to the mass change and thus the quartz's frequency response. Here a stationary state is reached because there is an equilibrium between implantation of N projectiles and sputtering of previously implanted N. Therefore, only sputtered Be atoms contribute to the measured net mass decrease. The implantation probability at the beginning of the irradiation can be estimated by assuming that the sputtering measured after saturation is the same as before. This is reasonable

if only a small amount of projectiles are implanted and the surface concentration of the sample does not change significantly. In a case such as shown in Figure 3.9, comparison to numerical models such as dynamic SDTrimSP simulations will be helpful for understanding the implantation and saturation behavior. Additionally, effects such as ion-induced diffusion might lead to a more complex scenario [86, 90].

QCM Electronics

Currently, QCM measurements are controlled by two different setups (see [74, 89, 91]). The base UHV cabling, feedthroughs and phasebox electronics are the same for both approaches. The quartz is driven at a given input frequency and the phase shift of the quartz's oscillation is obtained by the phasebox electronics, which give a feedback if the currently driven frequency is above or below the quartz's resonance. This is used for controlling the frequency regulation with a feedback voltage V_C returned by the phasebox.

In the approach described by Hayderer et al. [74], an analog oscillator provides the input signal at the resonance frequency of about 6 MHz and performs the regulation based on the feedback voltage V_C . The frequency is continuously recorded with a frequency counter, which is then connected to PC via a USB cable. The recording of the frequency over time is done with a program written in LabView.

Recently, a second approach was established based on using a Tektronix frequency generator instead of an analogue oscillator [89, 91], which allows more flexibility in exciting different oscillation modes (see section 3.1.2). Regulation is here performed by a python script, which uses the V_C feedback read by an Analog Digital Converter (ADC) to control the frequency generator's output. This has the advantage of unlocking other QCM measurement modes, but was also found to be more unstable and less responsive due to slower regulation. The quality of the quartz resonance is also massively dependent on the parameters of the controller, which can also vary between different setups and phasebox electronics.

The current implementation of the electronics setup allows measurements with signal drifts as low as 2 mHz/min and a signal noise of as low as 5 mHz [74]. This corresponds to mass change rates in the order of 10 pg/s that can be resolved [91]. For mineral film samples such as CaSiO_3 , this means that sputtering of about one

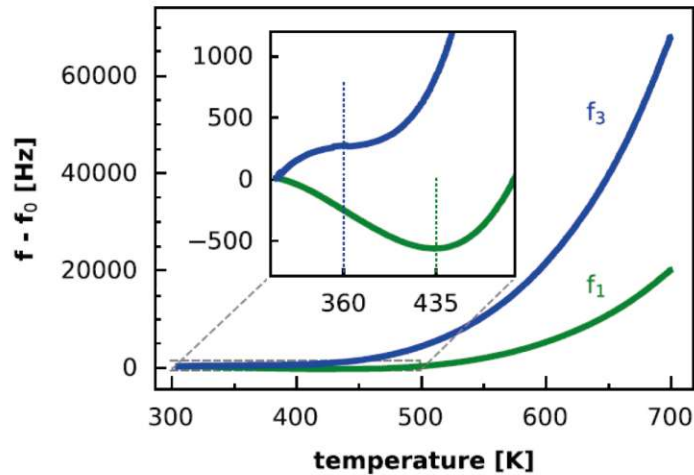


Fig. 3.10: This plot shows the temperature dependence of the QCM's fundamental (f_1 , green) and third overtone mode (f_3 , blue). Besides its stable working point at room temperature, the inset shows a minimum for f_1 at around 435 K (corresponding to 162 °C). In contrast, the temperature dependence of f_3 shows a saddle point at 360 K (87 °C). This figure is adapted from [89].

monolayer of material per hour can still be measured.

QCM Temperature Dependence and Dual Mode Compensation

Oscillating quartzes are frequently used sensory devices for many different applications. Besides being used as a microbalance for measuring mass changes during ion irradiations, they are also applied as sensors for several other applications, commonly as biosensors [92]. During measurements of ion-solid interactions, especially the sensitive temperature dependence of the QCM represents a challenge. Figure 3.10 shows an example measurement of the temperature dependence of the quartz's resonance frequency [89]. The green curve shows the fundamental frequency mode f_1 at a resonance frequency of around 6 MHz. The SC-cut quartzes are designed to have two stable working points at room temperature (20 °C) and in the frequency-over-temperature minimum at 435 K (162 °C), which is shown in the inset in Figure 3.10. Above the minimum, the frequency increases steeply with higher temperatures. Between the two working points, a frequency difference of up to 500 Hz exists, while the increase at higher temperatures is several kHz compared to the room temperature frequency. In comparison, frequency changes due to sputtering by ion bombardment are mostly below 1 Hz/min and as described

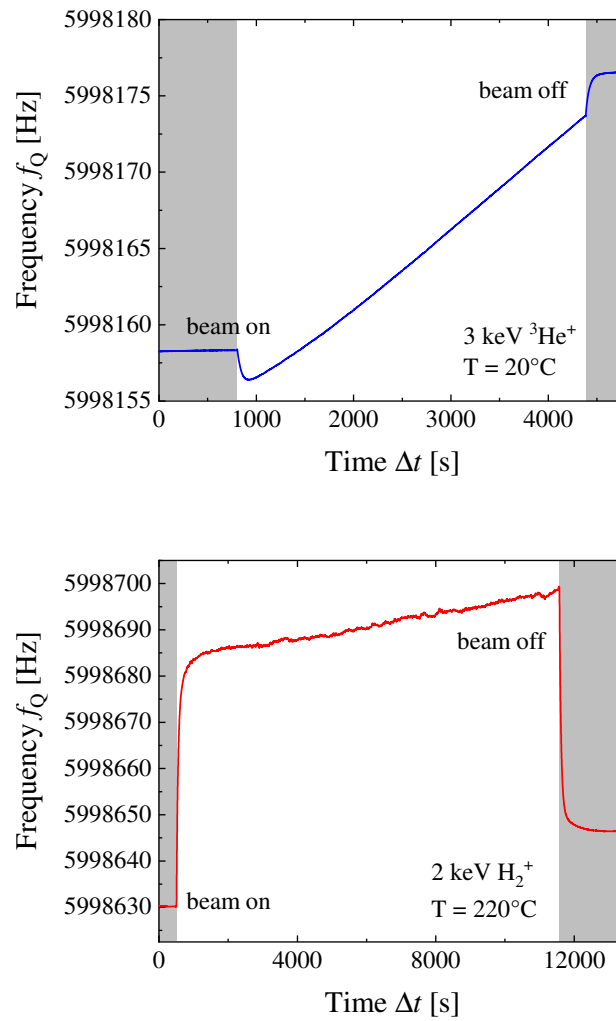


Fig. 3.11: Upper image: This figure shows an example of the transient frequency changes at the beginning and the end of an ion beam irradiation at room temperature. The measurement was performed with a CaSiO_3 sample being irradiated with 3 keV ${}^3\text{He}^+$ ions with an ion flux of $1.31 \times 10^{16} \text{ }^3\text{He}/\text{m}^2/\text{s}$ under normal incidence. Directly after the irradiation is started, the frequency drops by about 2 Hz and it takes in total several 100s until a stable frequency increase from sputtering dominates. When the ion beam is turned off, the opposite happens and the frequency increases again. Lower image: The observed transient behavior is different at higher temperatures as shown by the given example of a measurement with a CaSiO_3 sample that was heated to a temperature of 220°C with a heating current of 2.5 A. The sample was irradiated with 2 keV H_2^+ ions at an ion flux of $3.39 \times 10^{17} \text{ H}/\text{m}^2/\text{s}$. The sample temperature is above the minimum in the frequency-temperature characteristics (see Figure 3.10) and the frequency significantly jumps up when the ion beam is turned on. The steep increase is also in agreement with the less stable working point at this temperature.

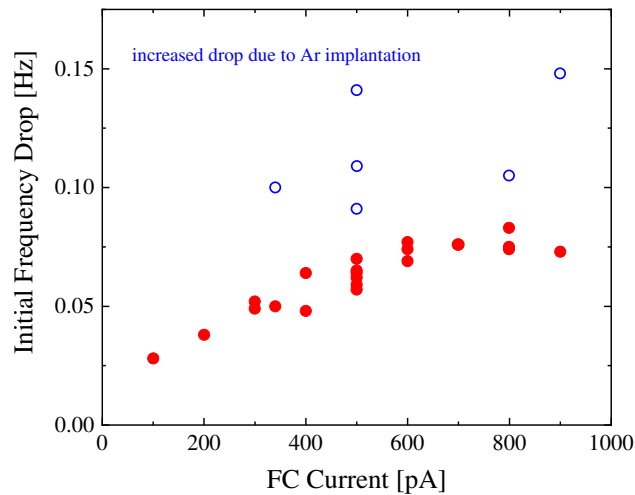


Fig. 3.12: This plot shows an analysis of the initial frequency drops at the beginning of irradiations at room temperature. For 4 keV Ar⁺ ions hitting a CaSiO₃ sample, measurements were performed at various ion currents showing that the amplitude of an exponential fit of the frequency drop increases with the ion current. Higher amplitudes after longer measurement breaks (blue) indicate a small amount of Ar implantation in the first few minutes of the irradiation. Figure adapted from [62].

before, the QCM sensitivity to mass-change-related frequency changes is in the range of mHz/min. Therefore, these measurements are reliant on a stable temperature of the sample and even then, experiments at temperatures apart from the two stable working points have proven to be challenging. On top of that, even turning on or turning off the ion beam irradiation of a QCM sample can lead to changes of the thermal equilibrium, which affect the measurement. This happens especially for light ions such as H or He, which cause significantly less sputtering than heavier ions at the same energy. The upper image in Figure 3.11 shows an example of the frequency, when a CaSiO₃ sample is irradiated with 3 keV ³He⁺ ions at room temperature under normal incidence at an ion flux of 1.31×10^{16} ³He/m²/s. When the ion beam is turned on, the frequency drops by about 2 Hz and it takes several 100 s until the slope of frequency increase due to sputtering becomes stable. An inverted behavior at a similar timescale can be observed after the ion beam is turned off. Measurements done in the scope of this thesis show that the observed initial behavior is inverted when the temperature lies above the position of the frequency-over-temperature minimum at 435 K (see Figure 3.11 showing an irradiation with 2 keV H₂⁺ at a temperature of 220 °C). It was also found that the transient behavior shows an exponential form, whose amplitude increases with the ion current, while its time constant is mostly independent of the ion current [62]. These measurements strongly indicate that the transient behaviors at the start and end of irradiations

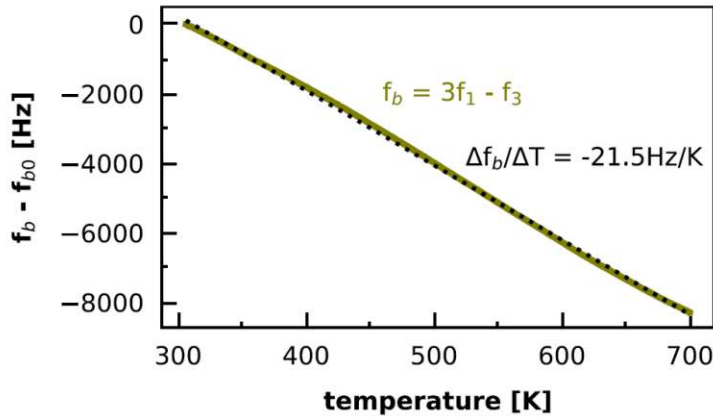


Fig. 3.13: This plot shows the dependence of the beat frequency $f_b = 3 \cdot f_1 - f_3$ on temperature. The dependence of f_1 and f_3 on f_b is obtained from a calibration measurement. Temperature compensation is then performed by recording f_b during a measurement and subtracting the known $f_1(f_b)$ or $f_3(f_b)$ function respectively. This figure is adapted from [89].

are caused by ion-beam-induced temperature changes of the sample (see Figure 3.12).

The crystal structure of quartz undergoes a phase change from the α phase present at lower temperatures to the β phase at 847 K [93]. In theory, conventional QCM experiments should be possible up to this temperature, but they are not feasible due to the increasing instability of the fundamental mode f_1 (see Figure 3.10). In order to enable measurements at higher temperatures and especially at varying temperatures, for example during a Thermal Desorption Spectroscopy (TDS) measurement, Stadlmayr et al. recently implemented a compensation method based on using two different oscillation modes of the quartz [89, 91]. Such techniques had been previously applied at lower temperatures (see for example [94] and other references given in [89]). Besides the fundamental C_1 mode at 6 MHz, the third overtone C_3 mode at almost 18 MHz is also excited. The C_3 mode has a different dependence on the temperature (see the blue curve in Figure 3.10), which can be used to separate frequency changes from temperature changes and those caused by mass changes. In particular, the beat frequency $f_b = 3 \cdot f_1 - f_3$ is close to linearly dependent on temperature (see Figure 3.13). With calibrated functions $f_1(f_b)$ or $f_3(f_b)$, the temperature component can be separated from frequency change measurements if the frequency f_b is also recorded over time. In the setup at IAP, this is realized by continuously switching between exciting the C_1 mode and the C_3 mode with the PC-controlled frequency generator at time steps of typically 5 to 10

seconds [91]. This approach was applied to measure D outgassing from Be samples during a TDS measurement [89].

Catcher-QCM Setups

The QCM technique is a very well-suited tool for sputtering measurements, but its applications for direct measurements are limited to thin film targets. For many cases, the exact phase of the target is not essential if it is not a single-crystal and therefore affected by ion channeling. Sputtering of polycrystalline targets is stated to be mostly comparable to sputtering by amorphous targets [24], and many materials amorphize anyway during long-term ion bombardment [95]. However, for polycrystalline W targets different behaviors due to linear collision sequences have been reported [96]. Additionally, in a realistic scenario, sputtering will be affected by surface roughness, which has a strong effect on the sputtering process [97]. In the most extreme cases, complex surface structures such as W fuzz or granular planetary regolith structures will be relevant and significant deviations in sputtering behaviors have been reported [98, 99, 100].

In order to perform sputtering investigations of more complex targets, a catcher-QCM setup has been developed [101]. Here a catcher-QCM is positioned next to the target and the mass increase due to sputtered atoms sticking to the quartz's surface are measured to deduce the sputtering of the target. The evaluation of such measurements becomes more challenging as the system is affected by different angular distributions of sputtered atoms, possibly unknown sticking coefficients and sputtering of the catcher-QCM surface by reflected ions. However, it removes almost any restriction on the target form and even the angular distribution of sputtered atoms can be probed. A linear catcher-setup has successfully been applied at IAP for reference-measurements with Au-coated samples [101], Fe-coated samples with oxide layers [84], CaSiO_3 films [84] as well as W films and W fuzz samples [100]. Furthermore, experiments with similar catcher setups have been performed for structured molybdenum surfaces by Li et al. [102] and ice surface by Galli et al. [103]. Recent developments at IAP have focused on upgrading existing catcher-QCM setups for circular motions around the target both in nuclear fusion and space weathering research [104, 105]. In doing so, the distance between target and catcher-QCM stays constant leading to higher signals and easier evaluation of the measurements as the distribution of sputtered particles can be measured more directly than in the previous linear setup.

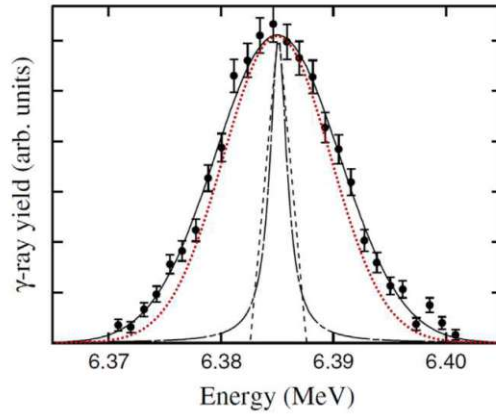


Fig. 3.14: This plot shows a measurement of the energy dependence of the γ yield of the nuclear reaction ${}^1\text{H}({}^{15}\text{N}, \alpha\gamma){}^{12}\text{C}$, on which ${}^{15}\text{N}$ NRA is based. Its narrow width of only 1.8 keV makes it a very important tool for high-resolution H depth profiling. The measured resonance width of the nuclear reaction as shown above is affected both by the natural resonance width as well as by Doppler broadening (red) [106].

Image taken from [106].

3.1.3 Ion Beam Analysis for H Isotope Retention

In the scope of this thesis, Ion Beam Analysis (IBA) was not only used as an important tool for the composition analysis of used samples (see section 3.1.5), but also applied for investigating the retention and outgassing behavior of H isotopes in W samples. For this purpose, W samples were investigated with NRA for depth profiling implanted ${}^1\text{H}$ and with Foil-ERDA to monitor the development of D concentrations during a TDS experiment (see chapter 6). The principles of these two IBA methods are described in the following sections.

${}^{15}\text{N}$ Nuclear Reaction Analysis (NRA) for Depth Profiling ${}^1\text{H}$

Nuclear Reaction Analysis (NRA) is a technique that is often used to measure depth-dependent concentrations with a unique precision [107]. It is based on measuring the secondary particles of nuclear reactions between the nuclei of the projectile ion and a target atom. Such nuclear reactions require small distances of closest approach and are therefore only possible for the analysis of light elements in typical MV accelerators. Heavier elements require higher energies to overcome the coulombic barrier, which is often not feasible. The cross sections for such nuclear reactions are usually governed by resonances and thus require a specific projectile energy.

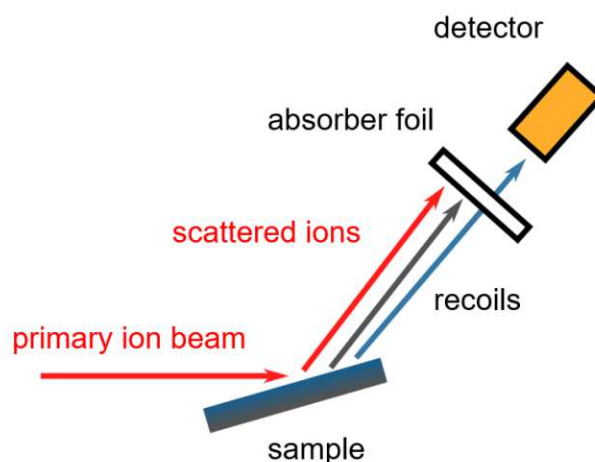


Fig. 3.15: This sketch shows the principle of a typical ERDA experiment. A multicomponent sample is irradiated with a primary ion beam, which creates recoils from large-angle scattering events. The energies of these recoils are measured with a detector in forward scattering direction. In order to filter specific species as well as scattered primary ions, an absorber foil is placed in front of the detector so that only light species can reach the detector.

As the ion loses energy while passing through the target mostly due to electronic stopping, different primary energies cause the nuclear reactions to be triggered at different depths. This can be used to extract a depth profile of a specific element by sweeping the primary beam energy. Here the width of the investigated nuclear resonance primarily determines the limit for the depth resolution of this analysis method.

For ^1H , the most common NRA technique uses ^{15}N ions as a primary beam [108]. It takes advantage of a resonance at the primary energy of 6.385 MeV, where the ^{15}N combines with a proton to form a ^{12}C nucleus under the emission of an α and a γ particle. During the NRA measurement, the γ particles are counted with a suitable detector and count rates allow the determination of the ^1H abundance. The $^1\text{H}(^{15}\text{N}, \alpha\gamma)^{12}\text{C}$ reaction has an extremely sharp resonance with a width of only 1.8 keV (see Figure 3.14), which allows precise H depth profiling [106]. As the analysis of H is difficult or even impossible with other commonly applied IBA techniques, ^{15}N NRA is regularly used as a complementary method to, for example, RBS and Time-of-Flight Elastic Recoil Detection Analysis (ToF-ERDA) [109].

Elastic Recoil Detection Analysis (ERDA)

For the in-situ investigation of D retention and outgassing in W samples (see section 6.2), the method of Elastic Recoil Detection Analysis (ERDA) was chosen [110]. Compared to RBS, ERDA is especially well suited for the investigation of light elements [111]. A detector setup with an absorber foil was used to filter out unwanted recoil species and scattered primary ions [67, 111]. The principle of such an experiment is sketched in Figure 3.15. The target of interest is irradiated with a primary beam, which probes the top layer of the sample of several 100 nm to several μm depending on ion species and energy. An energy-sensitive detector, usually placed in a forward-scattering geometry, is then used to analyze the recoils created by the probing beam. The recoil mass can be identified from the measured recoil energy and the scattering kinematics in the used setup geometry. Both the primary ions as well as the recoils lose energy to stopping as they move through the solid and therefore, recoils originating from deeper beneath the surface will have lower energies. This allows the measurement of depth-resolved concentrations with ERDA when the stopping of the recoil species in the sample material is known.

In multicomponent targets, the contributions from different elements will cause overlapping spectra and scattered primary ions are also not distinguishable in the detector. Therefore, placing an absorber foil with a known thickness of typically a few μm in front of the detector allows more precise investigation of light recoils [111]. These light atoms will have higher ranges than the heavier recoils and scattered ions. The foil is chosen so that the recoils of interest can pass through the foil and reach the detector, while the other particles are stopped. Of course, the energy and straggling in the absorber foil also have to be considered for the evaluation and result in a worsened depth resolution. For the particular case of D in W samples, a 3.4 MeV He^{2+} primary beam and an Al absorber foil with a thickness of 12.9 μm were used.

3.1.4 Thermal Desorption Spectroscopy (TDS)

TDS, or Temperature-Programmed Desorption (TPD), also represents an essential technique for investigating the desorption of H isotopes implanted in W samples (see section 6). It is commonly used in surface science to retrieve information on binding states of adsorbed or chemisorbed species [113, 114]. Similar information can be obtained for implanted atoms deeper in the sample, even though further

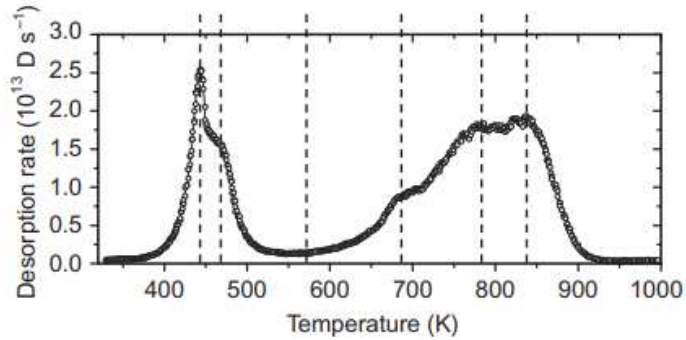


Fig. 3.16: This plot shows an example of a TDS measurement with a D-implanted single crystalline Be sample. During the heating, the RGA signal of $m = 4$ is recorded, which corresponds to the release of D_2 molecules. Several peaks and sub-peaks are visible, which correspond to different binding states of the implanted D. Figure taken from [112].

effects such as diffusion and re-trapping in defects affect the desorption behavior [115].

A TDS experiment is based on heating up a sample with a typically linear temperature ramp. At the same time, a RGA measures the amount of outgassing species correlated to the sample's temperature. The exponential behavior of binding states to the energy can result in very sharp desorption peaks that allow the determination of binding energies [112]. An example for such a measurement is shown in Figure 3.16. Even though TDS measurements are regularly used for quantifying the amount of an implanted species, they mostly give a unique insight into how these atoms are bound in a sample. In nuclear fusion research, this is especially of interest for the investigation of the retention of H isotopes in wall materials (e.g. [52]). However, it is also of interest in planetary science to find out whether implanted ions stay on the surface of a planetary body [86], or how hydroxyl and water molecules are formed as a result of the implantation of solar wind ions [116, 117].

3.1.5 Sample Preparation and Analysis

The experiments presented in this thesis were performed with different materials that are associated with the pyroxene mineral family for space weathering, as well as with W for nuclear fusion research. This subsection describes the principles of the most important used sample preparation and analysis techniques. Concrete

descriptions of the analysis results for the specific samples are given later in chapters 4, 5 and 6.

Pulsed Laser Deposition (PLD)

Pulsed Laser Deposition (PLD) was used as the main process to create thin films deposited from various mineral samples [118, 119]. PLD is based on a laser heating of a solid's near surface region to cause material ablation. The resulting plasma plume is directed towards a substrate, where emitted atoms form a thin film [120]. The main advantage of this technique is that it enables stoichiometric transfer even of complex target, which has made it an important tool for investigations with thin films of various oxides [121, 122]. PLD has also been applied for the deposition of minerals before: Such thin films were, for example, used to study growth kinetics [123, 124], or to improve the biocompatibility of medical implants by depositing wollastonite layers on top of them [125, 126, 127]. Hijazi et al. even used thin films of the mineral anorthite $\text{CaAl}_2\text{Si}_2\text{O}_8$ to perform sputtering measurements with a QCM in experiments similar to those presented in this thesis [43, 44].

The PLD of samples used in this thesis was done by Michael Doppler and Andreas Nennung at the Institute of Chemical Technologies and Analytics at TU Wien. For this purpose, a 248 nm KrF excimer laser was used at energies of a few $\text{J}/\text{cm}^2/\text{pulse}$ and a pulse frequency in the low Hz range [128]. These settings allowed the deposition of films with a thickness of a few 100 nm within one hour deposition time. More detailed descriptions of deposition parameters are later given in sections 4.2 and 5.2.

X-ray Photoelectron Spectroscopy (XPS)

Analysis of some samples from PLD was performed by X-ray Photoelectron Spectroscopy (XPS) to get information about the surface composition, which affects sputtering yields significantly. XPS is a common tool in surface science experiments, often used to investigate surface composition in-situ [129, 130]. It is based on irradiating the sample with X-rays, which causes the emission of inner-shell electrons from the sample's atoms via the photoelectric effect [131]. The energies of these electrons are then measured by, for example, a hemispherical sector analyzer [132].

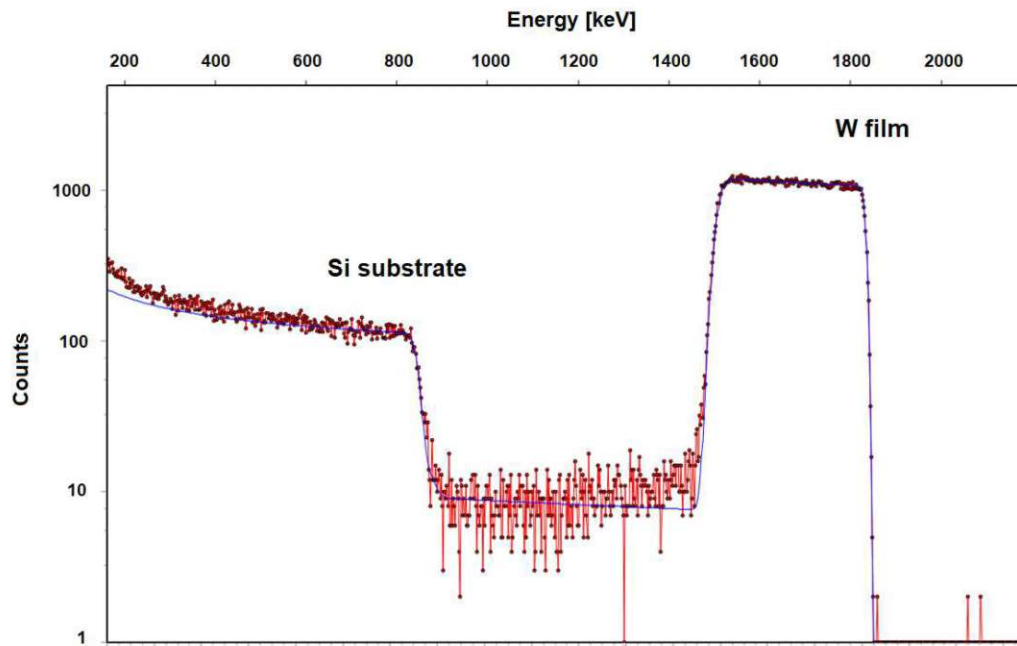


Fig. 3.17: This example spectrum shows the RBS analysis of a W film on a Si substrate with 2 MeV He ions, where counts are plotted over energy. The contributions from Si (left) and W (right) are clearly separated due to the differing energy transfer in backscattering. The energy width is caused by stopping of He ions in the solid and allows the determination of the thickness of the W film. For this case, the experimental spectrum (red) can be well reproduced by a simulation with the program SimNRA (blue) [133].

The electrons' energies are characteristic for the binding energies in the sample and thus allow identification and quantification of the sample's constituents [132]. Quantification is possible with a precision of sub-percent of atomic concentrations. Due to the limited range of the emitted electrons, the information is representative for about the top few nm of the sample [132]. Ex-situ XPS analysis has to be combined with sputter cleaning of the samples since they have to be transported at air between deposition and analysis and XPS results are sensitive to surface contaminations.

The XPS measurements of samples used for this thesis were performed by Markus Sauer at the Analytical Instrumentation Center at TU Wien. Detailed results are again given later in section 4.2.

Ion Beam Analysis Methods (RBS, ToF-ERDA)

Mineral films as well as W samples were also investigated using IBA methods, in particular with RBS and ToF-ERDA. These methods are very well suited for the analysis of thin films as they allow concurrent measurement of film thickness and depth-resolved concentrations. By using MeV ions as a primary beam, these methods are also mostly non-destructive, even though some influences on the samples might be caused by inducing additional vacancies (see section 6.1).

RBS uses a light primary ion species, for example He^+ at a few MeV, and analyzes the energies of backscattered ions [134]. At these energies, the scattering process can be well described with the Rutherford cross section:

$$\frac{d\sigma}{d\Omega} = \left(\frac{Z_1 Z_2 e^2}{4E}\right)^2 \frac{1}{(\sin \theta/2)^4} \quad (3.13)$$

The differential cross section $d\sigma/d\Omega$ is here given in the center-of-mass frame, Z_1 and Z_2 denote the atomic numbers of the scattering atoms, e is the elementary charge, E the ion incident energy and θ the scattering angle. Similar to other IBA methods, scattering kinematics give information of the target species and energy loss by stopping determines the depth resolution. Due to the well-known Rutherford cross section, quantitative analysis can be done precisely. It is best suited for investigating films of heavy materials on light substrates, as such a scenario leads to well-separated peaks. Figure 3.17 shows an example of such an RBS spectrum from a 2 MeV He analysis of a thin W film on a Si substrate used for H retention experiments (section 6.1), where detector counts are plotted over energy. Two main contributions are visible: The section at higher energies originates from scattering from W atoms, as the large mass difference between He and W prohibits efficient energy transfer. The left area results from scattering at the Si substrate, while the counts between result from multiple scattering events in the sample. The Si contribution clearly shows the $1/E^2$ behavior from the Rutherford cross section (equation 3.13).

Especially multi-component samples can lead to complex RBS spectra. Therefore, Time-of-Flight Elastic Recoil Detection Analysis (ToF-ERDA) analysis was also done for most samples as a complementary method. Contrary to RBS, heavier ions are used for the primary beam and it is better suited for examining light elements due to a worse mass resolution for heavy elements. ToF-ERDA is based on the same principles as described in section 3.1.3. Overlapping energy contributions from

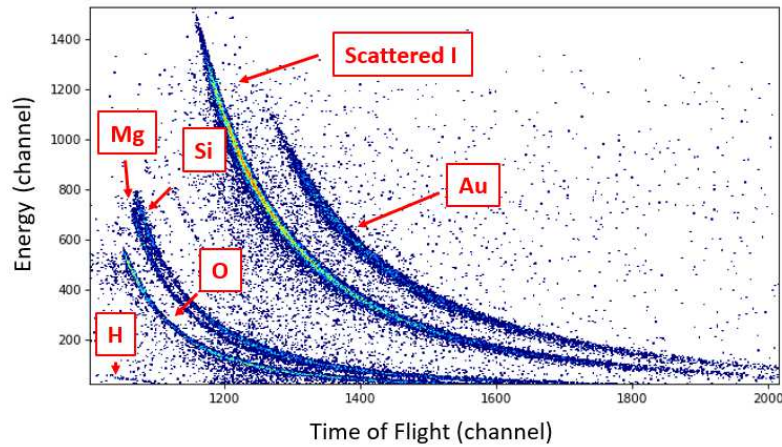


Fig. 3.18: This image shows the result of a ToF-ERDA analysis of a MgSiO_3 film with 36 MeV I^{8+} ions. The number of counts (given by the color) are plotted over time-of-flight (x-axis) and energy (y-axis), which are given as the discrete detector channels. Counts at higher energies come from recoils originating closer to the surface. Besides the sample elements, Au as well as Si and O in greater depths from the substrate are visible. A small amount of H was also found in the analysis.

different elements are avoided by additionally measuring the time of flight of the recoils on a defined length, which allow the determination of the target's atomic mass [135]. This is achieved, for example, by measuring pulses of emitted electrons as start and stop signal when the recoil passes through thin C foils [135, 136]. In a plot of energy over time-of-flight, each element contributes one curve, as it can be seen in the example in Figure 3.18. It shows the analysis of a MgSiO_3 film on a Au-coated Si wafer piece with a 36 MeV I^{8+} beam. The number of counts is given by the color and signals at higher energies correspond to locations closer to the surface, where the recoils have been less affected by stopping. Apart from the contribution of scattered primary ions, the elements from the sample (Mg, Si, O) and the substrate (Au as well as Si and O in deeper layers) are clearly visible. The energy-resolved spectra allow depth-resolved concentration analysis, quantification is given by the number of counts and the scattering cross section.

IBA of the samples used in the presented experiments were performed by Anna Niggas and Marcos V. Moro at Uppsala University. The results for specific samples are detailed in later sections discussing the respective experiments with these samples.

Atomic Force Microscopy (AFM)

As described before, the surface structure plays an important role for ion-surface interaction. Varying surface angles, shadowing and redeposition of sputtered material are responsible for different sputtering behaviors of rough surfaces. An Atomic Force Microscope (AFM) is very well suited for characterizing the surface on a nm scale [137] and it was therefore used for measuring the surface morphologies of the samples in this thesis. AFM measurements are based on moving a small tip across the sample and measuring the deformation of the tip cantilever caused by the interatomic interactions between the surface and the tip [138]. This deformation measurement is most commonly achieved by monitoring the deflection of a laser from the cantilever.

The Asylum Research Cypher AFM at IAP has been used for several studies of ion-induced surface modifications with swift heavy ions [139, 140] and fusion-relevant D ions [56]. In this thesis, AFM images were also recorded for the samples before and after irradiation to characterize surface roughness and to investigate its possible changes.

3.2 Theoretical Methods: Simulations with BCA-Codes

For the simulation of ion-solid interactions, two methods have become established: Molecular Dynamics (MD) and Binary Collision Approximation (BCA) codes. MD simulations solve the Newtonian equations for each atom in a given simulation cell based on interatomic potential [141]. This requires large computing power and has high demands on the potentials as they should reflect several properties of the investigated material. MD simulations are applied in different areas of research, but can also be used for a variety of calculations for the effects that occur when an ion hits a surface [142]. BCA simulations are somewhat simpler as they approximate the collision cascade in a solid as a series of random scattering events. Within a given energy range, this approximation yields accurate results if input parameters on the investigated material such as the surface binding energy are given. Due to the lower computing demands for good statistics, BCA simulations have become a common tool for sputtering research. For the cases studied in this thesis, BCA simulations were performed to compare experimental sputtering yields to numerical predictions. At the used ion energies in the range of several 100 eV to several keV,

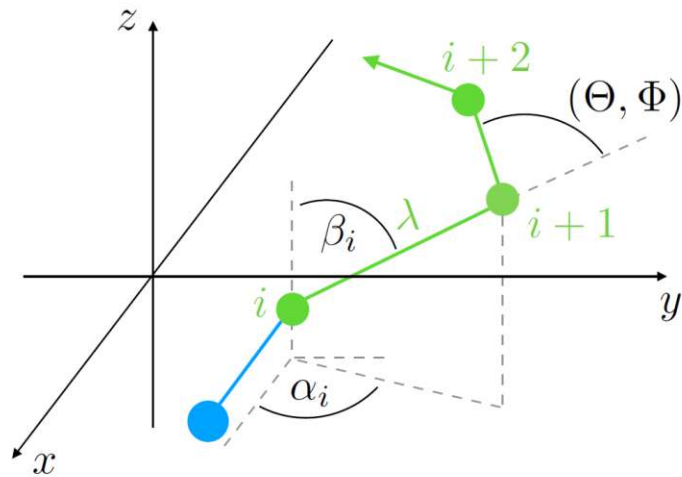


Fig. 3.19: This sketch gives an overview of the calculation procedure of programs that are based on the BCA. Instead of simulating all particle trajectories at the same time, interatomic collisions after a certain distance are calculated one after another. For each collision, energy transfer and scattering angles are determined, which is done for all atoms that take part in the collision cascade. Multi-body interactions and overlapping of collision cascades are neglected, which works well in an energy range of several 10 eV up to several 10 keV. Image taken from [10].

BCA codes are reasonably reliable for calculating sputtering yields, ion ranges and defect formations. This is, however, restricted to kinetic sputtering, while more complex effects such as potential sputtering are not included in BCA programs. The principles of such simulation codes are described in more detail below.

3.2.1 The Binary Collision Approximation (BCA)

As mentioned above, the Binary Collision Approximation (BCA) is the base for several established simulation codes of ion-solid interaction. Instead of calculating how all the atoms in a collision cascade are set into motion at the same time, the collision cascade is simulated in a step-by-step manner, which is sketched in Figure 3.19. An ion entering the solid moves a certain random distance depending on its mean free path length and scatters at a target atom. Scattering angles and energy transfer are calculated for the binary collision from a given interaction potential, usually a Coulomb potential with included screening by the electrons such as the KrC potential [12] or the universal ZBL potential [11, 26]. The ion then continues to move through the sample and more scattering steps are calculated until its energy falls below a

given cut-off energy of typically a few eV, where it is considered as stopped. The same calculation steps are done for the recoils that have been set in motion, where new recoils are created and also stopped in the target or sputtered from the surface. These steps are repeated until all trajectories for atoms participating in the collision cascade are calculated.

The BCA represents a comparatively fast way for simulating ion-solid interaction. However, one has to be aware of its limitations: Only including binary collisions results in a lower limit for the ion energy of about 30 eV to give accurate results [22]. For slower ions, collisions with multiple atoms should not be neglected and here MD simulations are advantageous. The step-wise calculation procedure neglects an overlapping of different branches of the collision cascades. Furthermore, the included treatment of electronic stopping as a friction force becomes less valid at higher energies where it represents the major mechanism of energy loss [22], which is, for example, relevant for swift heavy ions. At high projectile energies, therefore, other calculation methods such as the thermal spike model have to be used to appropriately reproduce experimental findings [143]. Additionally, the random steps between scattering events restrict the simulation to amorphous targets. Effects connected to the crystalline structure such as ion channeling [144] or linear collision sequences [96] are not included in conventional BCA codes, but have to be specifically implemented [145].

The BCA calculation process reproduces nuclear stopping, but electronic stopping has to be added artificially. This is usually done by using electronic stopping as a friction force [22]. Each moving particle loses energy between scattering events taken either from experimental data or approximations for the electronic stopping power, such as the Lindhard-Scharff-Schiøtt model or the Oen-Robinson model [146, 147].

Properties of the different elements such as mass or the density have to be included as external inputs. While most of them are well known, finding suitable values of the displacement energy or especially the surface binding energy are challenging. These energies respectively define the threshold necessary for an atom to leave its position in the bulk or to be sputtered from the surface. The surface binding energy strongly influences the sputtering yield [24] and is difficult to determine at the same time. It can be approximated with the heat of sublimation for mono-elemental targets [22], but for composite targets there still exists a lack of a valid formalism for calculating

the surface binding energies. In most cases, one therefore has to rely on fitting them to reproduce experimental results, which is further discussed in section 4.3.

Examples for BCA codes are the two programs SRIM and SDTrimSP [20, 26], which were both used in the scope of this thesis. While SRIM has become a common tool for sputtering inputs in planetary science, SDTrimSP and its extensions for 2D and 3D surfaces are more established in nuclear fusion research. Especially for space weathering-related investigations it was thus an important task to compare both programs and assess which is better suited for sputtering simulations.

3.2.2 SRIM

The Stopping and Range of Ions in Matter (SRIM) program suite is a very commonly used tool for calculating different effects of ion-solid interaction [11, 20]. It is publicly available online (<http://www.srim.org/>) and represents an easy-to-use tool for calculating ion ranges, stopping and doing BCA simulations. SRIM has regularly been chosen as the reference for providing sputtering yields in space weathering research [34, 148, 149], but its accuracy for sputtering has been contested [150, 151]. For the cases investigated in this thesis, it will therefore be further tested how well SRIM reproduces experimental sputtering yield results.

3.2.3 SDTrimSP

SDTrimSP is a code for BCA simulations, which is currently developed at Max-Planck-Institute of Plasma Physics (IPP) [26]. It represents a continuation on previous developments of the TRIM.SP and TRIDYN codes [152, 153, 154] and has focused on sputtering mechanisms that are relevant for plasma-facing components in a nuclear fusion reactor. In doing so, several important capabilities have been developed that open up more possibilities for sputtering simulations. Similar to TRIDYN, it includes dynamic changes of the target resulting from the ion bombardment. Such target changes can result from preferential sputtering as well as ion implantation and diffusion effects [78, 86, 155, 156], which can significantly influence the sputtering behavior during prolonged irradiation.

Recent developments of the code have focused on expanding it to allow 2D and 3D geometries for the simulation of rough surfaces [157, 158]. This is realized by discretizing the simulated target into columns or cubes respectively, which each have a specific local composition and can be affected by the incident ions individually. This discretization was found to be a well-suited approximation for a smooth surface if the grid dimensions are smaller than the dimensions of the collision cascade [158]. These new versions of SDTrimSP so far have been used to investigate the sputtering of rough Fe and W targets [73, 159], as well as the roughening and W enrichment of W-containing EUROFER steels [160, 161].

In planetary science, SDTrimSP is less commonly used. Schaible et al. compared SRIM and SDTrimSP simulation results for oxide surfaces and found better agreement with older experimental data for SDTrimSP [151]. The very good agreement between experiments and SDTrimSP simulations was also found for the studies in the scope of this thesis [87, 88, 162], which will be presented in detail in the following chapters.

Results: Sputtering of Lunar and Hermean Analogs by Solar Wind Ions

This chapter describes experimental and theoretical results on the sputtering of planetary analog samples by solar wind ions. Section 4.2 will first detail the sample preparation procedures as well as the sample analysis results. Section 4.3 will then describe the measurements of kinetic sputtering by singly charged ions and how this process can be simulated with BCA codes. Corresponding results for the potential sputtering by multiply charged ions are then presented in the following section 4.4, where both experiments and a model for the dynamic behavior of potential sputtering based on preferential sputtering of O atoms are included. Finally, section 4.5 combines the previously gained insights to calculate the sputtering effects of the H and He components of the solar wind.

Large parts of this chapter were published before this thesis was written: Some contents of section 4.2, the H^+ and some Ar^+ measurements from section 4.3 as well as some measurements with multiply charged Ar ions from section 4.4 were published in [162]. Further contents from section 4.2, the He results from section 4.3, experiments and modeling for potential sputtering by He and Ar from section 4.4, as well as the solar wind calculations in section 4.5 were published in [88].

4.1 Introduction

While other ion-induced erosion effects also occur in the solar system, ions from the solar wind, about 96% H^+ , 4% He^{2+} and a minor heavy ion component, represent the major source of erosion by sputtering on most small planetary bodies. Even though the solar wind flux of about 10^{12} ions/ m^2 at the Moon is small compared to typical laboratory ion beam fluxes, it significantly contributes to changing planetary

surfaces over astronomical timescales. Both for the understanding of space weathering as well as for modeling exosphere creation, a precise knowledge on different sputtering effects is needed. So far, most estimations based on previous experimental results or simulations are used as sputtering inputs that are not well constrained. Especially the prominent potential sputtering effect by multiply charged ions so far has been rarely investigated (see [42, 43, 44, 163, 164]) and requires further understanding and quantification.

For this purpose, the sputtering by different solar wind ions has been investigated in detail using the mineral wollastonite CaSiO_3 as an analog for the surface of the Moon and Mercury. Wollastonite is a pyroxenoid that has a similar crystal structure to the pyroxene mineral family that can be found on both bodies in large abundances [165, 166]. The composition of wollastonite with about 60% O and 20% Si is similarly found in many other minerals, sputtering yields for wollastonite should therefore give a good representation for solar wind sputtering on planetary bodies.

4.2 Sample Preparation Parameters and Analysis Results

The original wollastonite mineral piece for depositions on oscillating quartzes was provided by Peter Wurz and Klaus Mezger from the University of Bern. In order to create two smooth parallel facets, the mineral was polished using a wet-grinding machine. Afterwards, it was heated for three days at 320 °C in an evacuated environment under a pressure of 10^{-2} mbar to deplete the sample of remaining water from the polishing process. It was then used for the deposition of thin films onto QCMs with PLD at the Institute of Chemical Analytics and Technologies at TU Wien. PLD was performed with a 248 nm KrF excimer laser at a pulse frequency of 5 Hz with 2 J/cm²/pulse. PLD was performed at sample temperatures between 250 °C and 270 °C at background O₂ pressures of 0.04 mbar. The deposition times varied between 30 minutes and 2 hours.

The best suited sample-analysis procedures for PLD-deposited mineral films have been developed during recent years. One of the most important quantities is the sample composition, which will influence the sputtering yields significantly. For first depositions, the sample composition was checked with XPS showing in general a

	Ca	Si	O	H	C
Sample Composition	18.3%	19.6%	59.5%	1.6%	1.0%

Tab. 4.1: An overview of the average elemental concentrations in the wollastonite films from ToF-ERDA measurements. The composition is very close to the nominal composition of 20% Ca, 20% Si, 60% O and contamination from H and C were found to be low.

The data used for the average sample composition shown in this table was published in [88].

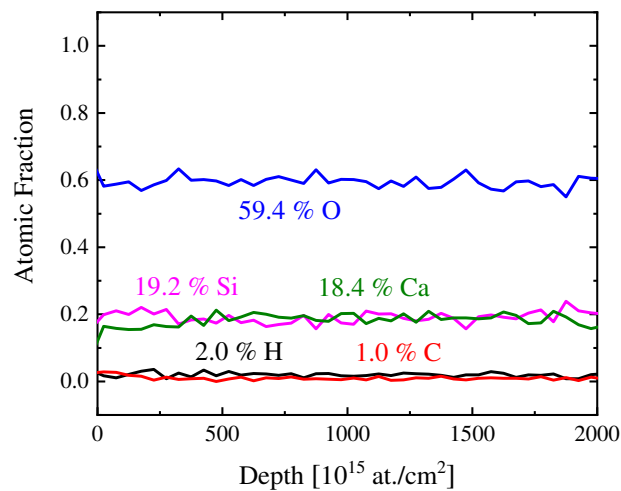


Fig. 4.1: The different elemental concentrations in a wollastonite film sample from ToF-ERDA show a very uniform distribution in depth. Depth on the x-axis is here given corresponding to thin-film units of 10^{15} at./ cm^2 . This figure was published in [88].

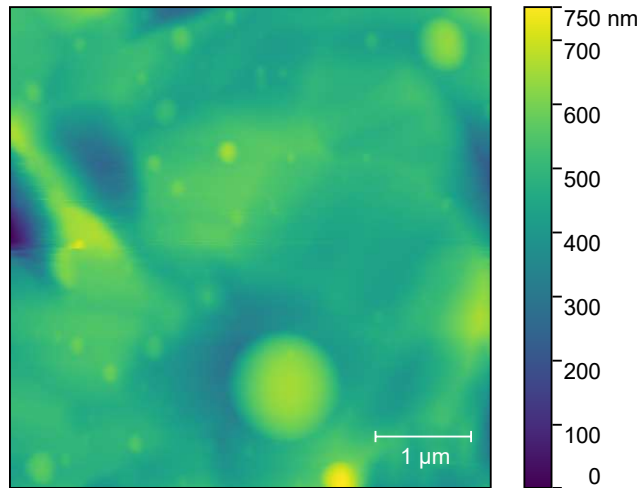


Fig. 4.2: This example for an AFM image of a wollastonite film shows a mostly smooth surface with only a small number of circular particles on top. This was published in an adapted form in [167].

good agreement with the nominal composition of CaSiO_3 , but a lower Ca content than the original material and C contamination was found [162]. This was later checked with IBA and ToF-ERDA revealed those deviations to be contained within the close surface region. In deeper layers and averaged over the bulk of the films, the composition of the wollastonite film samples was determined to be 18.3% Ca, 19.6% Si, 59.5% O [88]. Contamination from H and C makes up between 1% and 2%. The ToF-ERDA analysis results are tabulated in table 4.1 and an example for the depth-resolved concentration is shown in Figure 4.1, clearly showing no signs of any significant variations.

IBA measurements also give the possibility of evaluating the sample thickness. RBS of different samples revealed strongly varying thicknesses between 30 nm and 700 nm [88], which was calculated from RBS results assuming the nominal wollastonite density of 2.86 g/cm^3 [168]. The surface of the different samples was characterized with AFM measurements and mostly smooth surfaces were found for thinner films. Figure 4.2 shows an example for such a smooth surface, where only a few round structures are visible. The distribution of local inclination angles for the same sample as determined from the AFM measurement is shown in Figure 4.3. For the dominant low inclination angles below 20° , sputtering yields do not significantly change and overall, the surface roughness is neglected for later sputtering yield evaluations. For thicker films, rougher surfaces with more features and larger contributions from the high inclination angles were found. For these samples, sputtering yields were

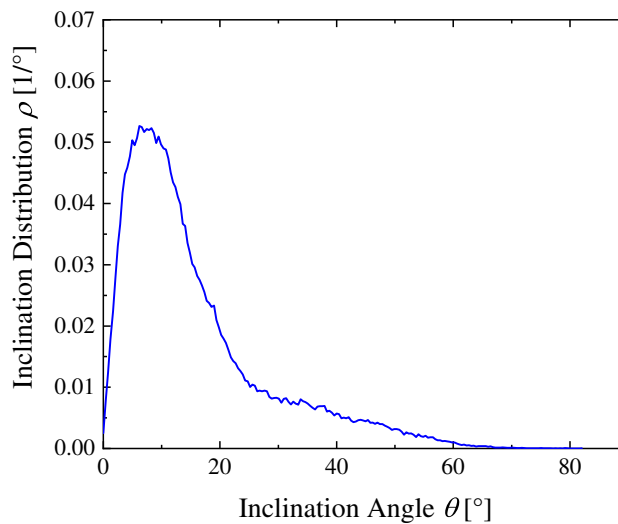


Fig. 4.3: The distribution of local inclination angles for the wollastonite sample depicted in Figure 4.2 shows mostly angles below 20°.

found to deviate due to surface roughness effects. Additionally, some experiments with thicker films were affected by apparent electrical charging up effects leading to massive spikes in the frequency signal that made the recording of sputtering yields almost impossible. For these reasons, mostly thinner films with smooth surfaces were used for the experimental investigation of the sputtering of wollastonite that is presented in the following sections.

The crystallinity of thin film samples was investigated with X-Ray Diffraction (XRD) (performed by Michael Doppler at the Institute of Chemical Technologies and Analytics of TU Wien) and under the polarization microscope (performed by Noah Jäggi at the University of Bern). Both methods showed no signs of the crystallinity of the original material being preserved and instead amorphous films were observed. This can most likely be connected to the deposition temperature, which was kept low in order to prevent possible harm to the quartz substrates.

4.3 Kinetic Sputtering

Sputtering measurements with the QCM technique allow the investigation of several different ion-solid interactions at the same time, which is a big advantage of this method. However, it can be challenging even at a stable QCM working point to split

up the contributions from different sputtering mechanisms or ion implantation to the measured frequency and thus mass changes. For the irradiations at energies in the low keV range presented in this thesis, the kinetic sputtering from the ion-impact-induced collision cascade will always cause significant mass changes of the samples. It is therefore important to gain an accurate understanding of kinetic sputtering to deduce the importance of other effects, such as potential sputtering by multiply charged ions. Kinetic sputtering is also the only sputtering mechanism that is accurately represented in BCA simulations. The first following section therefore examines how the kinetic sputtering of silicate materials can be simulated to achieve a good agreement with experiments. The subsequent sections will then present the measured sputtering for solar wind relevant ions.

4.3.1 Kinetic Sputtering by Ar⁺ from Experiment and Modeling

For the purpose of investigating kinetic sputtering of silicate minerals, Ar⁺ ions were chosen. Ar is not a major component of the solar wind with a concentration in the order of 10⁻⁶ [163], but it allows measurements with large signals that are not influenced by chemical effects due to Ar being a noble gas. Sputtering yields for Ar⁺ were measured under different angles of incidence α in respect to the surface normal. The results for energies of 1 keV, 2 keV (taken from [84]) and 4 keV are compiled in Figure 4.4, with measured values being shown as the red dots. In comparison to other materials, the observed angular dependence is very pronounced (compare for example sputtering yield compilations in [22]). Sputtering yields of around 20 amu/ion increase by up to a factor between 5 and 6 for oblique angles of incidence. For smaller angles of incidence, this represents a significant deviation from the angular dependence of $\cos(\alpha)^{(-5/3)}$, which results from the Sigmund model for mono-elemental targets [24]. Similarly, the peak of the angular dependence at around 70° is found at comparably high angles.

During the experiments with 4 keV Ar⁺, some signs of Ar implantation during the irradiations were observed. Similar to the He measurements described later and discussed in [86], lower yields were observed in the beginning until, before a steady state at a higher yield is reached when the sample becomes saturated with Ar. For lower energies, this behavior was not found to play a significant role, which is in accordance to observations by Wittmaack et al. [169]. In their work, no Ar implantation in undamaged SiO₂ was reported. Retention of Ar of a few % of the irradiation fluence was observed correlated to ion-induced damage loss and was

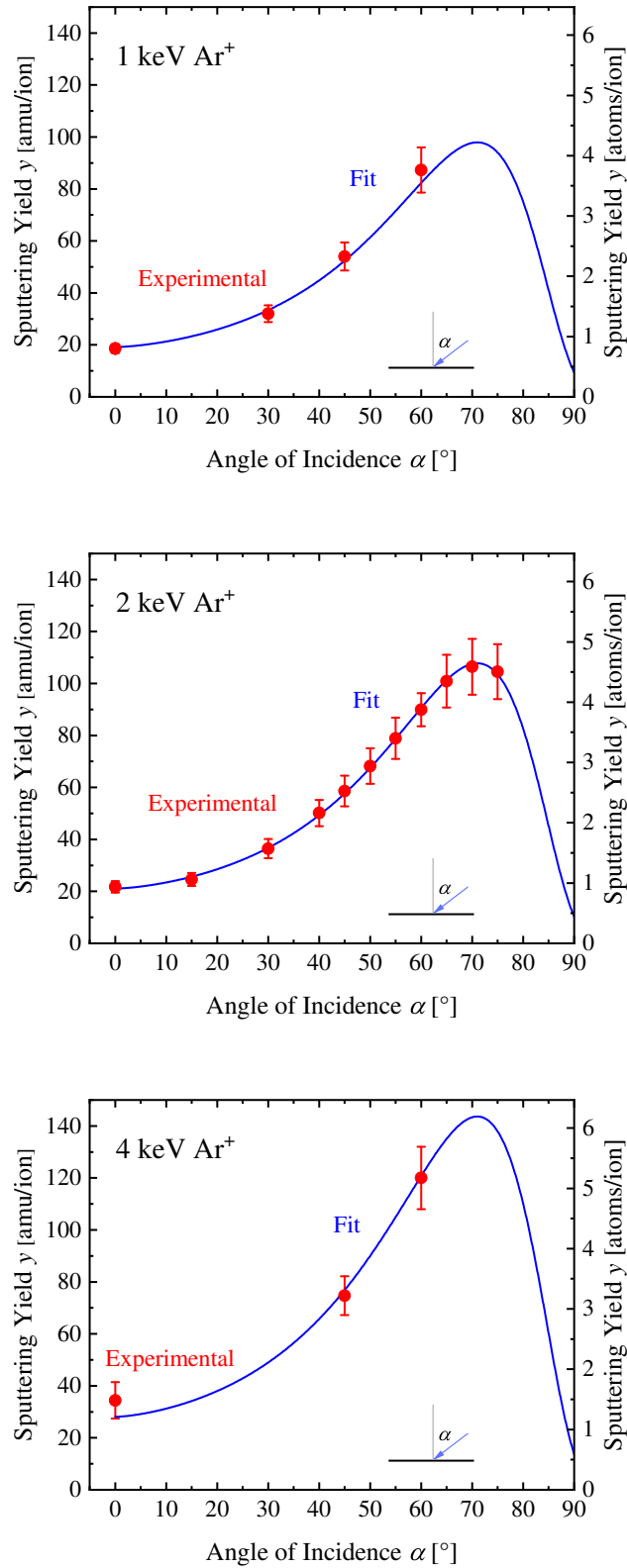


Fig. 4.4: Experimental results (red) and fits (blue) for sputtering yields of wollastonite by Ar⁺ irradiation at 1 keV, 2 keV and 4 keV are plotted over the angle of incidence α in respect to the surface normal. The used fit formula (see equation 4.1) is described in the text.

The experiments for 2 keV Ar⁺ were mostly performed in the scope of previous work [84] and have been published in [162].

	Y_0	α_0	b	c	f
1 keV Ar ⁺	19.14	$\pi/2$	1.85	0.75	4.81
2 keV Ar ⁺	21.06	$\pi/2$	1.85	0.75	4.81
4 keV Ar ⁺	28.48	$\pi/2$	1.85	0.75	4.81

Tab. 4.2: This table gives an overview of the used fitting parameters for sputtering yields of wollastonite samples under Ar⁺ bombardment, using the fitting formula by Eckstein and Preuss described in equation 4.1 [16]. For 1 and 4 keV the values of b , c and f were taken from the 2 keV fit and only Y_0 was used as a free parameter. α_0 is always set to $\pi/2$ following the suggestion by Eckstein and Preuss to neglect the effect of surface binding energies on incoming noble gas projectiles [16].

therefore higher for larger energies.

The blue curves in Figure 4.4 represent a fit by the formula proposed by Eckstein and Preuss [16], which represents an improved version of the original fit formula by Yamamura and Shindo [25]. This formula can be applied to describe the dependence of the sputtering yield Y on the angle of incidence α at an energy E and looks as follows:

$$Y(E, \alpha) = Y(E, 0) \left(\cos \left[\left(\frac{\alpha \pi}{\alpha_0 2} \right)^c \right] \right)^{-f} \exp \left(b \left[1 - \frac{1}{\cos \left[\left(\frac{\alpha \pi}{\alpha_0 2} \right)^c \right]} \right] \right) \quad (4.1)$$

Y_0 , c , b and f were used as fitting parameters, α_0 was set to $\pi/2$ following the description by Eckstein and Preuss to neglect binding energies to the surface for noble gas projectiles [16]. However, these binding energies are typically in the low eV range similar to surface binding energies and are negligible at the keV energies examined in the present thesis. $\alpha_0 = \pi/2$ is therefore used for all following fits. As a result from this approximation, no further energy dependence apart from $Y_0(E)$ is included in equation 4.1. The fit was first calculated for the 2 keV data with all free parameters. For 1 keV and 4 keV c , b and f were then fixed to the values derived for the 2 keV data because no experimental values are available that show the exact position, where the yield peaks. Only Y_0 was then used as a free fitting parameter and these results are compiled in table 4.2. In doing so, a consistent agreement can be derived for all measured angles at the three energies shown in Figure 4.4, which strongly supports the validity and consistency of the measurements.

For sputtering simulations, both SDTrimSP and SRIM were tested to simulate kinetic sputtering yields. Following the ToF-ERDA measurements that showed good agreement of the sample's composition to the original mineral, the nominal CaSiO₃

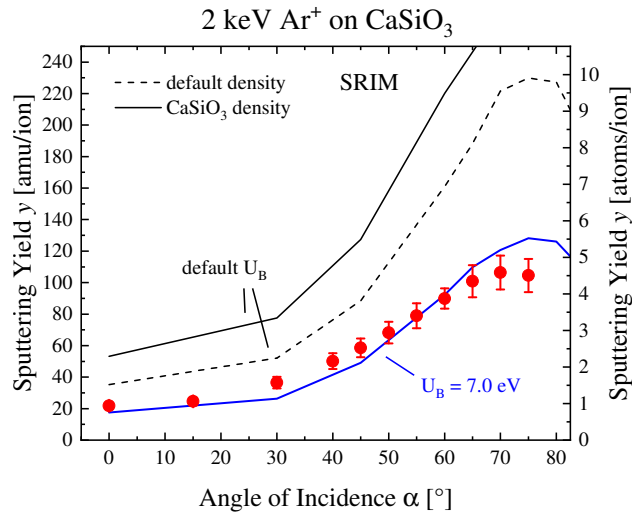


Fig. 4.5: This plot shows different SRIM modeling results for the sputtering of CaSiO_3 by 2 keV Ar irradiation compared to the experimental results (red dots). The measurement is significantly overestimated by a simulation with default parameters (dashed black line) and even more so when the nominal wollastonite density is used (full black line). A better agreement can be reached by increasing all surface binding energy values to 7 eV.

composition of 20% Ca, 20% Si and 60% O was used as an input. This mainly leaves the surface binding energies as possible free parameters in the simulation. Due to the inverse proportionality of the sputtering yield on this quantity [24], the choice of surface binding will have a large effect on the simulation. As mentioned before, the determination of surface binding energies can be difficult. For mono-elemental and especially metallic targets, setting the surface binding to the value of the sublimation enthalpy leads to good results [22]. For composite targets, no such valid approximations exist. Different formalisms have been suggested [170, 171, 172], but there still exists no universally applicable method to calculate surface binding energies. The most reliable method is to adapt the input parameters so that simulation results reproduce experimental data and ideally give a consistent theoretic description that holds for different irradiation scenarios. The O surface binding energy U_B^{O} represents the biggest unknown, which is reflected in the fact that different SDTrimSP versions use different default O surface binding energies. However, due to the different bonds in a composite material, the surface binding energies of the other components U_B^{Ca} and U_B^{Si} can also be expected to change in comparison to mono-elemental targets [173, 174].

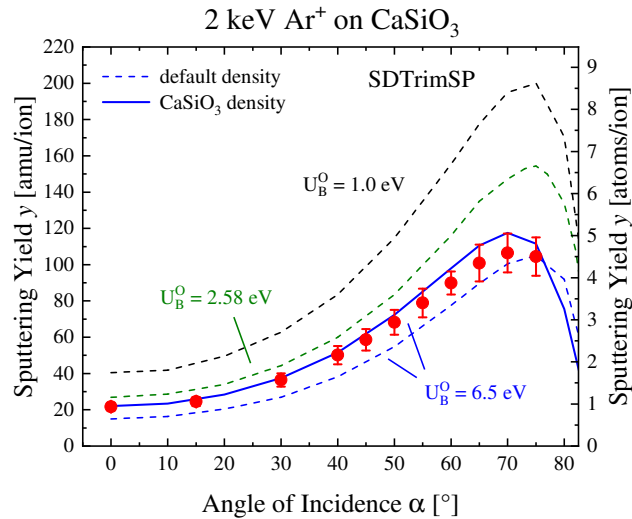


Fig. 4.6: This plot gives an overview of different SDTrimSP modeling results compared to the 2 keV Ar^+ experiments (red dots). Dashed lines use the default density from SDTrimSP for the given composition, while the blue full line uses the nominal wollastonite density. Default input values for the surface binding energy overestimate the experiments (dashed black and green lines). The best agreement is found by setting U_B^O to 6.5 eV and using the setting "isbv=2" that causes SDTrimSP to use an averaged surface binding energy for all elements. This simulation method also works very well for 1 keV and 4 keV (see Figure 4.7). This figure was published in an adapted form in [88].

For SRIM [20], Figure 4.5 shows a comparison between experimental sputtering yields (red dots) and simulation results with different input parameters. Evidently, SRIM significantly overestimates sputtering when the default parameters are used (dashed black line) and even more so when the nominal CaSiO_3 density of 2.86 g/cm^3 is considered (full black line). A reasonable improvement for agreement with the total sputtering yield can be achieved, for example, when the surface binding energy U_B^i for every element is increased from their original values between 1.8 and 4.7 eV to 7 eV (blue line). This does not completely reproduce the observed angular dependence of the sputtering yield, but further improvements might be possible with tweaking the specific elemental surface binding energies.

A similar comparison of experimental data and different simulations is presented in Figure 4.6 for SDTrimSP. As mentioned above, the default binding energies for O vary between program versions. Up to version 5 of SDTrimSP, a value of 2.58 eV was used as the default for U_B^O , representing half the oxygen dissociation enthalpy. In the recent version 6, U_B^O is decreased to 1 eV to fit experimental results for some oxide targets better [26]. Figure 4.6 compares the measured sputtering yields to

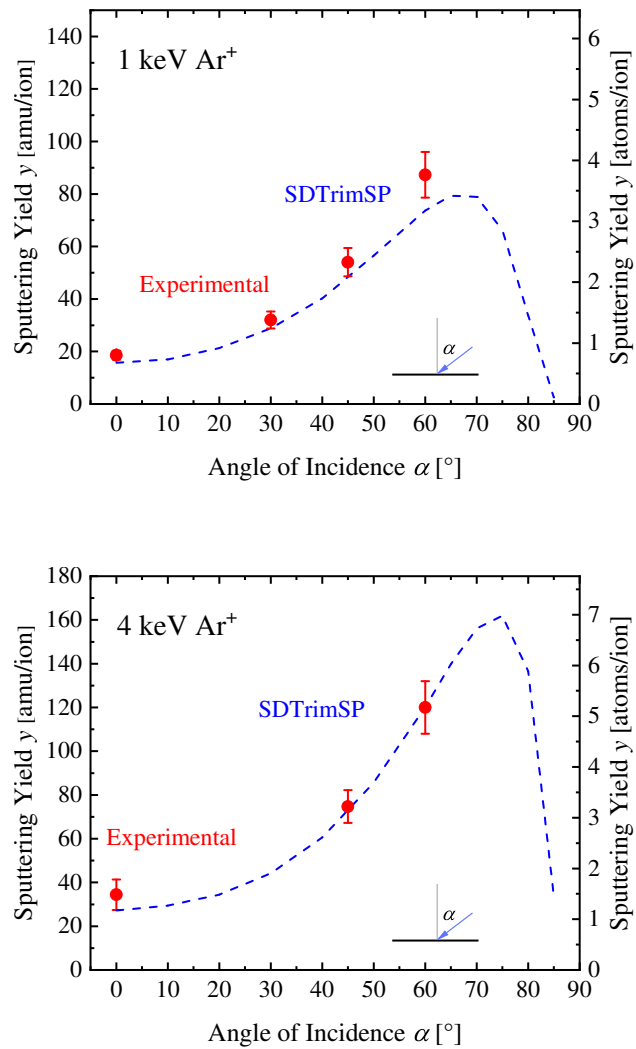


Fig. 4.7: The best-fitting SDTrimSP simulations for 2 keV Ar⁺ shown in Figure 4.6 consistently reproduce experimental findings also for the other investigated energies.

different static SDTrimSP simulations performed with the KrC interaction potential and as is shown there, both $U_B^O = 2.58$ eV (green dashed line) and $U_B^O = 1.0$ eV (black dashed line) overestimate experimental values. While older versions were not too far off, there are also significant changes to the inputs necessary compared to the newest version 6. The best agreement was found by using $U_B^O = 6.5$ eV as well as with the nominal CaSiO_3 density of 2.86 g/cm³ [88] (full blue line). The latter was realized by setting the density parameter "dns_0" of SDTrimSP for O to 0.7. The simulation shown in Figure 4.6 was also performed with the setting "isbv=2", which causes SDTrimSP to use the same averaged surface binding energies for all species (5.21 eV, calculated from the elemental surface binding energies weighted with the respective elemental concentrations in the target). This setting somewhat suppresses preferential sputtering, but good agreement with the SDTrimSP simulations was also found for longer irradiations as discussed in the following chapters. For the other Ar energies, sputtering yields are also consistently reproduced well (see Figure 4.7). Using the same inputs, even sputtering yields for other projectiles (discussed later in this thesis) and for other silicate samples have been simulated accurately [86, 87].

Some improvements to the modeling approach will be possible by measuring in-situ changes of the surface composition during ion bombardment. QCM measurements only give information on the mass removal per ion and thus the total sputtering yield. For example, in-situ XPS or Auger Electron Spectroscopy (AES) measurements could give additional information in this regard. Measuring the energy distribution of sputtered atoms would also give insights into the surface binding energies, but this requires a sophisticated experimental setup (see for example [175]). Otherwise, calculating surface binding energies with MD simulations also represents a promising approach [173, 176]. This method could be applied for other materials where suitable interatomic potentials exist and should be tried in the future. Nevertheless, the above described simulation inputs have now been tested for different sample materials and projectiles and have become established for simulating the kinetic sputtering yields of planetary analog samples at IAP.

4.3.2 Sputtering by H⁺ Ions

With a concentration of about 95%, H⁺ ions are the most prominent component in the solar wind. They occur at energies of around 1 keV, but due to their small mass, they will cause significantly less sputtering than heavier solar wind ions. It is important to quantify the sputtering yields by protons to compare them to the yields

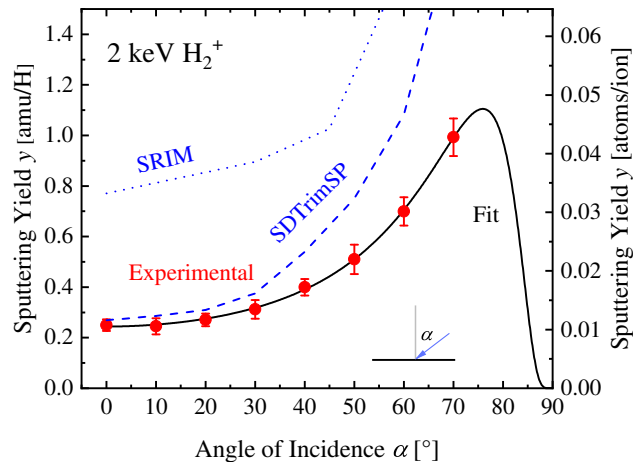


Fig. 4.8: This plot shows the angular dependence of the sputtering yield of CaSiO_3 irradiated by 2 keV H_2^+ . Yields are plotted in amu/H and experimental results (red) are compared to simulations (blue). While the data can be fitted well by the Eckstein formula (black), the angular dependence is overestimated by SDTrimSP simulations with adapted surface binding energies (dashed blue line). However, the agreement is still better than it would be for a SRIM simulation with default inputs, which is off by a factor of about 3. This image is adapted from [162].

	Y_0	α_0	b	c	f
2 keV H_2^+	0.24	$\pi/2$	0.62	0.97	2.43

Tab. 4.3: This table shows the fitting parameters (equation 4.1) for measured sputtering yields of CaSiO_3 by 2 keV H_2^+ irradiation shown in Figure 4.8.

of other ions. This is essential for the assessment of how much each ion species contributes to the total space weathering process.

In order to investigate the sputtering by 1 keV protons, CaSiO_3 samples were irradiated with 2 keV H_2^+ ions. The experiments were performed with molecular ions due to a larger available ion flux from the ion source compared to atomic H^+ ions. At these energies, no molecular effects have been reported at 1 keV/ion [177] and irradiation with 2 keV H_2^+ is regarded as equivalent to two 1 keV H^+ ions hitting the sample at the same time. First experiments with H projectiles showed an implantation behavior similar to that discussed in [86] for augite: A net mass increase or lower mass decrease, depending on the angle of incidence, was observed at the beginning of the irradiation leading to a saturation and a stable mass decrease (see Figure 4.9 for an example).

Sputtering yields were obtained from the steady state reached after a fluence of several 10^{21} H/m², which agrees with reports for forsterite as well as SiO₂ and olivine [178, 179]. The experimental results are presented for different angles of incidence as the red dots in Figure 4.8. The sputtering yields are given in amu/H to allow comparison to 1 keV H. The full black line shows the fit based on equation 4.1 and the resulting fitting parameters are summarized in table 4.3. Observed sputtering yields are about two orders of magnitude lower than the previously measured Ar sputtering yields. Additionally, the angular dependence is less significant as is shown by the lower fitting parameter f compared to the Ar case. Figure 4.8 also includes simulation results by SDTrimSP with the optimized input parameters discussed in the previous section (dashed blue line). The less pronounced angular dependence is here not reproduced by the simulation. The sputtering yields from the calculation agree very well with the experiment up to an angle of 30°, but then increase faster and deviate from the measurement data. Nevertheless, the agreement is much better than it would be for simply using a SRIM simulation with default parameters, which is included in Figure 4.8 as the dotted blue line. Here the experimental values are overestimated by a factor of about 3, which agrees with findings for SiO₂ and Al₂O₃ [151]. Interestingly, it was found that the agreement with SRIM simulation could be improved if the less precise "Detailed Calculation with Full Damage Cascades" mode is used instead of the recommended "Monolayer Collision Steps / Surface Sputtering" mode [162]. However, it remains questionable how feasible it is to apply SRIM in a calculation mode, where a full treatment of sputtering processes is not included.

Taking a closer look at the implantation effects, Figure 4.9 shows the development of the mass depletion of the wollastonite sample over fluence in red. This curve is taken from an irradiation under 60°, where the sample was first subjected to H irradiation. At the beginning, the mass depletion is high due to some further cleaning effects, which might indicate chemical sputtering of some remaining adsorbates after sample cleaning. Then it becomes lower and increases again to a steady state after about 2×10^{21} H/m². The steady state mass depletion is lower than the prediction of a static SDTrimSP simulation indicated by the dashed black line. With a dynamic SDTrimSP simulation (dashed blue line), a much better agreement is reached when implantation of H in the sample is included with a maximum local H concentration of 30%. Then both the fluence dependence and the absolute values of the mass depletion from sputtering and implantation reproduce the experimental observations. In the steady state, implantation of new H ions and sputtering of previously implanted H compensate each other and the net mass decrease is only caused by

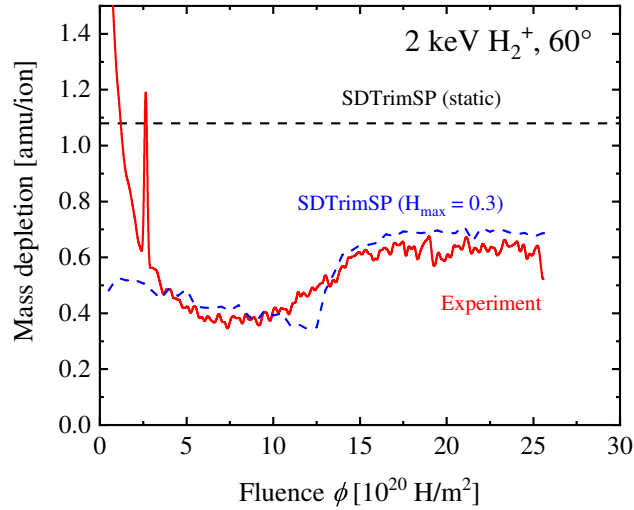


Fig. 4.9: For a first H irradiation, a significant fluence dependence can be observed as it is here shown for 60° (red line). Following an initially high mass depletion, lower values are observed before a steady state is reached. In the steady state, the measurement results are still lower than would be predicted by a static SDTrimSP simulation (dashed black line). The agreement with the experiment is significantly improved with a dynamic SDTrimSP simulation, where H implantation is included up to a maximum local concentration H_{\max} of 30% (dashed blue line).

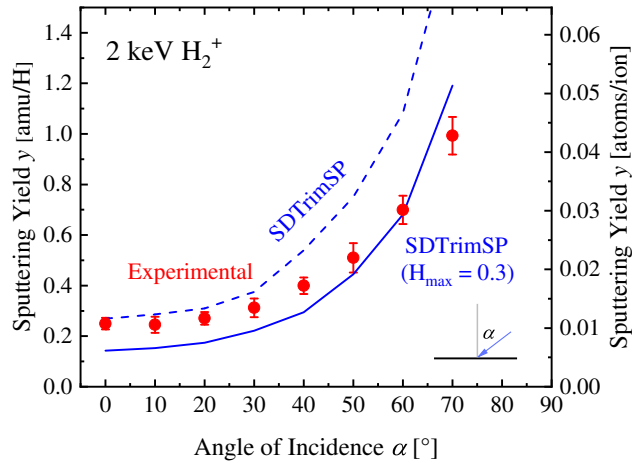


Fig. 4.10: When dynamic simulations with H implantation up to a concentration of 30% are performed for different angles of incidence, the agreement between experiment and simulated steady state values is improved for higher angles of incidence. However, at lower incidence the simulation predictions for the sputtering yields are also lower and deviate more from the experiment than before. This figure was published in an adapted form in [162].

sputtered wollastonite. Due to the significant H concentration near the surface, the sputtering of Ca, Si and O atoms is also suppressed. Therefore, the sputtering yields are lower than in a case where no implantation occurs. Dynamic simulations with the same parameters were performed for the whole range of investigated angles and the steady state sputtering yields (full blue line) are compared to the experimental steady state sputtering yields in Figure 4.10. The agreement at higher angles is much improved, but seemingly at the cost of agreement at the lower angles of incidence, where the simulation is too low.

Previous research on H⁺ bombardment of SiO₂ and olivine revealed an initial OH formation probability of close to one [179]. OH formation at each O atom would correspond to a local H concentration for a CaSiO₃ target of about 35%. This is consistent with the 30% H saturation concentration that was used to improve results with dynamic SDTrimSP simulations. It has to be noted that these apparent 30% of H concentration would represent the maximum capability of H that can be incorporated in the mineral. Realistic solar wind conditions consist of significantly lower fluxes and temperatures of up to several hundred °C, which will cause the desorption of at least a part of previously implanted H [178]. However, as similarly stated for solar wind He [86], regolith rims closer to saturation conditions might develop in permanently shadowed regions on the Moon, Mercury or other similar planetary bodies.

The worsened agreement for normal incidence irradiation after including implantation effects might be caused by variable maximal concentrations due to different defect densities, where more H might be implanted. Another effect that will play a role is the stopping of keV protons in the solid. Such protons are fast enough to lose a substantial amount of their energy to electronic stopping, SRIM suggests a factor of over 6 dominance of electronic stopping over nuclear stopping, while SDTrimSP gives a factor of about 3. Uncertainties in the electronic stopping inputs will affect the ion's range and how much energy is available in nuclear collisions. Therefore, it also plays a role for the exact sputtering yield. Stopping in BCA programs is calculated from tabulated values or from approximations such as the Lindhard-Scharff model or the Oen-Robinson model for mono-elemental targets. For the SDTrimSP simulations shown above, an average of the Lindhard-Scharff and the Oen-Robinson stopping was used (parameter "inel0=3"). For compounds, stopping is by default calculated by Bragg's rule, which simply consists of an average of the elemental stopping powers weighted by the concentrations in the sample. Some compounds, however, require correction factors and especially for oxides, significant deviations

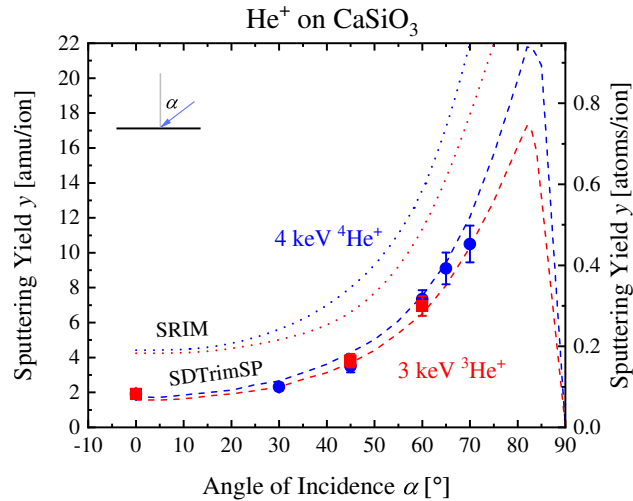


Fig. 4.11: This plot shows the angular dependence of sputtering yields by both 4 keV $^4\text{He}^+$ (blue) and 3 keV $^3\text{He}^+$ (red) irradiations. Experimental results (points) are presented together with SDTrimSP simulations (dashed lines) and SRIM simulations (dotted lines). For the investigated angles, both He isotopes have coinciding sputtering yields at solar wind velocity. The experimental observations are very well supported by SDTrimSP simulations. This figure was published in an adapted form in [88].

from Bragg's rule have been reported at low velocities [180]. It has yet to be checked how this varying stopping affects the exact sputtering yields by H ions.

4.3.3 Irradiations with $^4\text{He}^+$ and $^3\text{He}^+$ Ions

With a concentration of about 5%, He is the second most abundant element in the solar wind. Its greater mass and its energy of about 4 keV will cause higher sputtering yields, but more importantly He^{2+} ions will cause additional potential sputtering of oxide surfaces (see section 4.4). In order to quantify potential sputtering, first the kinetic sputtering by He^+ ions had to be measured. He^{2+} measurements require the use of ^3He as a working gas to separate He^{2+} from H_2^+ ions in the sector magnet, which have the same m/q for $^4\text{He}^{2+}$. For this reason, 3 keV ^3He ions at solar wind velocity were used for irradiations as well as 4 keV ^4He to compare their kinetic sputtering yields as a precursor for $^3\text{He}^{2+}$ measurements.

Similar to H irradiations with wollastonite and He irradiations with augite [86], initial He irradiation was affected by the implantation of He ions. Saturation was

	Y_0	α_0	b	c	f
4 keV $^4\text{He}^+$	1.75	$\pi/2$	0.42	0.93	2.59
3 keV $^3\text{He}^+$	1.56	$\pi/2$	0.49	0.93	2.70

Tab. 4.4: This table shows fitting parameters (equation 4.1) for the CaSiO_3 sputtering yield's angular dependence for both 4 keV $^4\text{He}^+$ and 3 keV $^3\text{He}^+$. In order to better fit the position of the yield's peak, the SDTrimSP simulation results were fitted instead of the measured yields.

reached after a fluence of about 10^{21} He/m². For similar experiments of He implantation in the mineral augite, Biber et al. calculated the concentration of implanted He from QCM measurements by assuming constant sputtering until saturation [86]. The resulting implanted He concentrations agreed well with subsequent TDS measurements, where the desorption of implanted He was investigated. For the present case of wollastonite, a He concentration of 6% or lower could be calculated.

Figure 4.11 shows the measured steady state sputtering yields (dots) for ^4He (blue) and ^3He (red). Very steep angular dependences are observed with an increase of sputtering by about a factor of 5 at 70° when compared to normal incidence. Absolute values of the sputtering yields are about one order of magnitude higher than those for H^+ ions and one order of magnitude lower than for Ar^+ ions. The yields by 4 keV ^4He and 3 keV ^3He ions were found to coincide for the investigated angle range, showing that 3 keV $^3\text{He}^{2+}$ will behave the same way as 4 keV $^4\text{He}^{2+}$ in regards to kinetic sputtering.

These experimental observations are also supported by BCA simulations. SRIM predicts similar sputtering yields for both He isotopes at the same velocity, but again massively overestimates the yield by about a factor of 2 (dotted lines in Figure 4.11). SDTrimSP with the previously described adapted input parameters, on the other hand, coincides with most of the measured sputtering yields for both 3 keV $^3\text{He}^+$ and 4 keV $^4\text{He}^+$ (dashed lines). The absolute values and the steep angular dependence are both well reproduced. Table 4.4 shows the fitting parameters for 3 keV $^3\text{He}^+$ and 4 keV $^4\text{He}^+$. Here the SDTrimSP simulation results were fitted to get a better fit of the peak position of the yield's angular dependence. This maximum is actually predicted to be at an oblique incidence angle between 80° and 85° , where the yield becomes about a factor of 10 higher than under normal incidence. Due to experimental limitations in the sample holder design, this peak position cannot be investigated by measurements. Nevertheless, for the available angles the agreement is very good and the peak position of the yield's angular dependence was, for exam-

ple, in agreement with 2 keV Ar measurements presented previously.

Due to the above stated experimental observations of He implantation, dynamic SDTrimSP simulations were also performed to check whether this would affect measured sputtering yields. For a maximum He concentration in the sample of 6%, SDTrimSP predicts sputtering yield changes of below 7%. This is in line with observations from Biber et al., where no significant changes to the total sputtering yields in the steady state were found for He implantation in augite at concentrations of 10% [86]. The yield variation of 7% for the wollastonite case are also lower than the experimental uncertainties. It is therefore feasible to take static SDTrimSP simulations as a reference for the kinetic sputtering of He ions.

4.4 Potential Sputtering

Due to most planetary minerals being insulating materials, additional sputtering effects have to be expected for the irradiation with multiply charged ions [7]. The most abundant multiply charged ion in the solar wind is He^{2+} , but also other ions such as O, C and Fe will be found with charge states of 5+ or higher. Therefore, a detailed experimental understanding is required to quantify their contribution to the total space weathering on bodies such as the Moon or Mercury.

4.4.1 Irradiations with ${}^3\text{He}^{2+}$ Ions

Potential sputtering measurements to assess the contribution by He^{2+} ions of the solar wind were performed with ${}^3\text{He}$ at solar wind velocity. In the sector magnet that is used to separate different ion species and charge states, ${}^4\text{He}^{2+}$ with mass-over-charge-state ratio $m/q = 2$ cannot be distinguished from molecular H_2^+ . Possible H contamination in the ion source could therefore influence the sputtering measurements. They would be registered in the current measurement, but hardly contribute to sputtering because H sputtering yields are about an order of magnitude lower than He sputtering yields at solar wind energies. This overestimation of the He ion flux would lead to an underestimation of the sputtering yield by He^{2+} that would be difficult to quantify. Thus, ${}^3\text{He}$ was chosen as a working gas because ${}^3\text{He}^{2+}$ with $m/q = 1.5$ can be easily distinguished from other ions. The measurements with

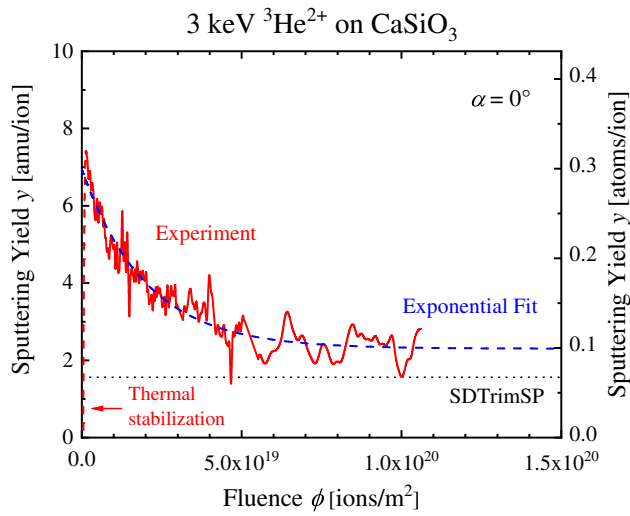


Fig. 4.12: The irradiation of CaSiO_3 by 3 keV ${}^3\text{He}^{2+}$ ions at normal incidence shows a significant fluence dependence (red line). Compared to the ${}^3\text{He}^+$ yield (dotted black line), the initial yield is more than three times higher and then decreases exponentially with the fluence. Steady state yields remain higher than for ${}^3\text{He}^+$. This figure was published in an adapted form in [88].

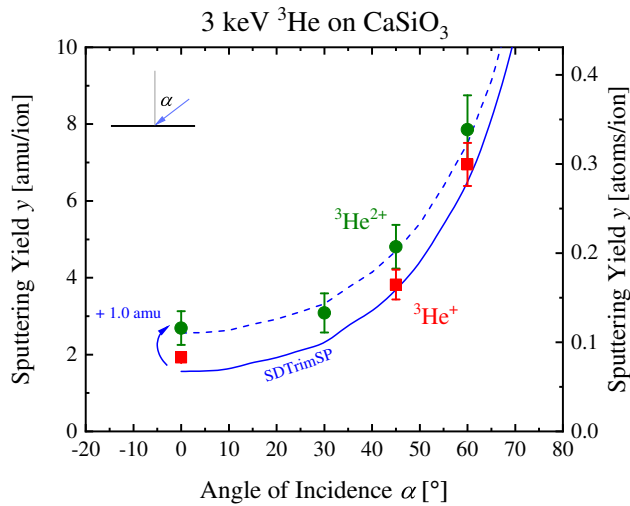


Fig. 4.13: Comparing measured steady state sputtering yields of CaSiO_3 by 3 keV ${}^3\text{He}^+$ and ${}^3\text{He}^{2+}$ irradiation reveals a constant increase of 1 amu/ion for all investigated angles of incidence. This figure was published in an adapted form in [88].

	A	ϕ_0	y_0
3 keV ${}^3\text{He}^{2+}$	4.64 amu/ion	1.998×10^{19} ions/m ²	2.30 amu/ion
8 keV Ar^{8+}	54.06 amu/ion	8.52×10^{17} ions/m ²	57.76 amu/ion

Tab. 4.5: Fitting parameters for the fluence dependence of the sputtering yield of CaSiO_3 under 3 keV ${}^3\text{He}^{2+}$ and 8 keV Ar^{8+} irradiation based on equation 4.2. The data shown in this table was published in [88].

3 keV ${}^3\text{He}^+$ presented in the previous section showed the same sputtering yields as 4 keV ${}^4\text{He}^+$. The potential energy of a ${}^3\text{He}^{2+}$ ion is also the same as for a ${}^4\text{He}^{2+}$ ion and consequently, 3 keV ${}^3\text{He}^{2+}$ ions will give a good representation of the sputtering effects of solar wind He.

CaSiO_3 samples were irradiated with ${}^3\text{He}^{2+}$ under angles of incidence between 0 and 60°. In order to minimize the influence of He implantation (described in the previous section), ${}^3\text{He}^{2+}$ irradiations were not done with unirradiated samples. Instead the sample was first irradiated with ${}^3\text{He}^+$ until steady state where the mass decrease from sputtering becomes constant. Then it can be assumed that the sample is saturated with He and only the mass changes resulting from sputtering are recorded. Figure 4.12 shows the fluence dependence for a following ${}^3\text{He}^{2+}$ irradiation under normal incidence. The first few minutes of the irradiation are affected by a heating of the QCM sample due to turning on the ion beam (dashed red line). Then a large sputtering yield is observed in the experiment, which quickly decreases during the irradiation (full red line). Compared to the sputtering yield of about 2 amu/ion under ${}^3\text{He}^+$ irradiation, the initial yield is increased by over a factor of 3 to about 7 amu. This difference of about 5 amu can be attributed to potential sputtering. In respect to the ion's potential energy, this corresponds to $\gamma_{\text{He}} \approx 81.3 \pm 20.0$ amu/keV. Even though the sputtering yield decreases during the irradiation, its steady state value is still higher than the sputtering yield by ${}^3\text{He}^+$ ions, which is represented by the SDTrimSP simulation result (dotted black line) in Figure 4.12. Figure 4.13 compares measured steady state yields for ${}^3\text{He}^+$ (red squares) and ${}^3\text{He}^{2+}$ (green dots) for different angles of incidence and finds a constant increase of about 1 amu/ion for all angles. This observation does not indicate a significant angular dependence of potential sputtering, which represents a large contrast to the pronounced angular dependence of kinetic sputtering. This indicates sputtering by energy deposition directly after ion impact, where the varying penetration depths at different angles do not play a significant role.

The steady state of the sputtering yield y shown in Figure 4.12 was reached by an exponential decrease with fluence ϕ with the following form:

$$y(\phi) = A \cdot e^{-\frac{\phi}{\phi_0}} + y_0 \quad (4.2)$$

A fit with this function is included in Figure 4.12 as the dashed blue line and follows the experimental results very well. The fitting parameters are shown in table 4.5. The characteristic fluence for the exponential decrease $\phi_0 = 1.998 \times 10^{19}$ ions/m² is found to be very short. After a fluence of $5 \times \phi_0$, the total mass decrease of the sample is calculated as $32 \cdot 10^{15}$ amu/cm². The wollastonite density of 2.86 g/cm³ corresponds to 172×10^{15} amu/cm²/nm. Steady state is therefore reached after only sputtering the first few monolayers of material.

Similar sputtering dynamics have been observed for previous experiments on the potential sputtering of oxides [75, 76]. The potential sputtering of these materials has also been connected to a sputtering of the surface O [27]. It can therefore be assumed that the observed fluence dependence is caused by a preferential sputtering of O atoms from the surface and therefore an O depletion. The same fluence dependence as shown in Figure 4.12 could actually be reproduced with used samples either by prolonged sputtering with 2 keV Ar⁺ or by subjecting the sample surface to an O₂ ambient pressure of 10⁻⁴ - 10⁻³ mbar for several hours at room temperature or heated to 200 °C. In doing so, a closer to stoichiometric surface should again be created by either sputtering away the depleted region or by re-oxidizing the surface.

4.4.2 Irradiations with Ar^{q+} Ions

To get a better understanding of the underlying effects of potential sputtering, experiments were also performed with Ar ions at various energies and charge states. An example for the fluence dependence of the sputtering yield for 8 keV Ar⁸⁺ under normal incidence is depicted in Figure 4.14, where a similar behavior as for ³He²⁺ is observed. This could again be reproduced with both sample surface refreshing methods of Ar⁺ sputtering and O flooding. For 8 keV, no Ar⁺ measurements were possible due to a maximum acceleration voltage of the ion source of 6 kV, but following the good agreement for other energies, SDTrimSP simulations (dotted black line) are taken as a reference for kinetic sputtering. Compared to the simulated kinetic sputtering yield, again a much increased yield at the beginning with a lower steady state yield is measured (red line). The fluence dependence also follows an

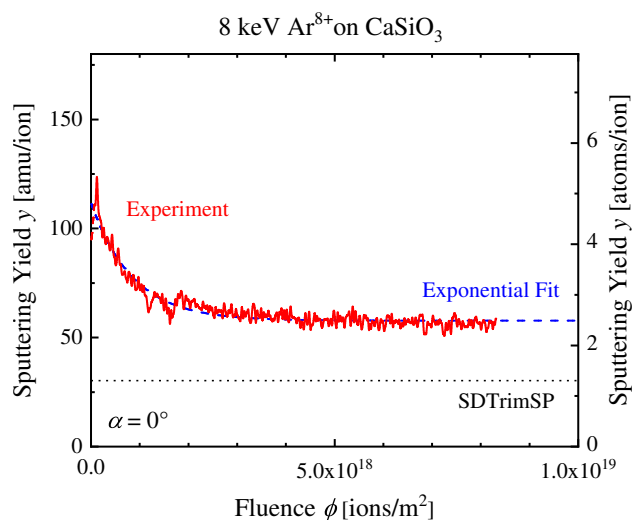


Fig. 4.14: The fluence dependence of sputtering of CaSiO_3 by 8 keV Ar^{8+} ions (red) shows a similar behavior as was previously observed for $^3\text{He}^{2+}$. It can again be described by an exponential decay (dashed blue line) and steady state yields remain significantly higher than the kinetic sputtering yields (dotted black lines). This figure was published in an adapted form in [88].

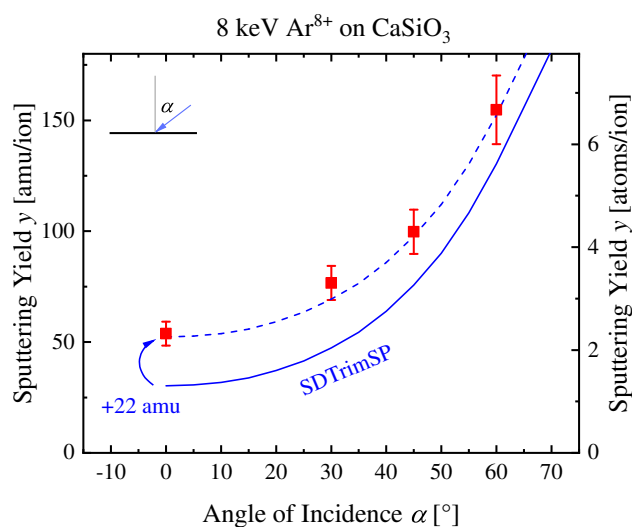


Fig. 4.15: In the steady state, the angular dependence of the sputtering yield of CaSiO_3 by 8 keV Ar^{8+} ions (red) shows a constant shift to higher values by 22 amu when compared to kinetic sputtering yields (blue full line). This figure was published in an adapted form in [88].

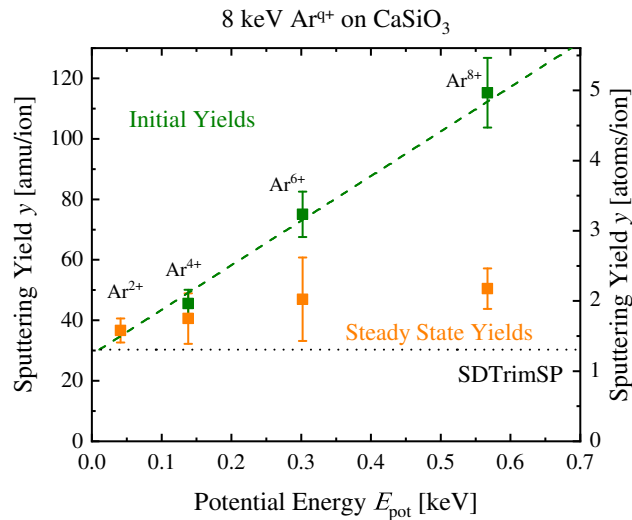


Fig. 4.16: Initial sputtering yields for different Ar charge states (green) show a different dependence on the potential energy E_{pot} than the steady state yields (orange). In particular, the potential sputtering contribution of the initial yields follows a linear dependence on E_{pot} as signified by the dashed green line. This figure was published in an adapted form in [88].

exponential decay described by equation 4.2 (blue line), with the fitting parameters given in table 4.5. Comparison to the ${}^3\text{He}^{2+}$ experiment reveals a similar relative increase of the initial yield, but a much shorter fluence required for the steady state. Compared to kinetic sputtering, the steady state yield is also higher than for the ${}^3\text{He}^{2+}$ case. After a fluence of five times the decay length ϕ_0 , the total mass loss of the sample was $29 \cdot 10^{15}$ amu/cm², which is almost the same as the $32 \cdot 10^{15}$ amu/cm² for ${}^3\text{He}^{2+}$. It is therefore a universal observation that the steady state of potential sputtering is reached after sputtering away a few monolayers, which is in line with the observations by Hayderer et al. for MgO and Al₂O₃ [75, 76].

Another result that is similar for ${}^3\text{He}^{2+}$ and Ar⁸⁺ is the angular dependence of potential sputtering, which becomes evident in Figure 4.15. As indicated by the dashed blue line, the measured sputtering yields (red squares) are all about 22 amu higher than the SDTrimSP simulation. This constant increase for all angles was also observed for ${}^3\text{He}^{2+}$ (see Figure 4.13), but now for Ar⁸⁺, the increase is more significant.

Initial yields and steady state sputtering yields were measured at the same kinetic energy of 8 keV for different Ar charge states, with the results being presented in Figure 4.16. Measured sputtering yields at the beginning of an irradiation (green)

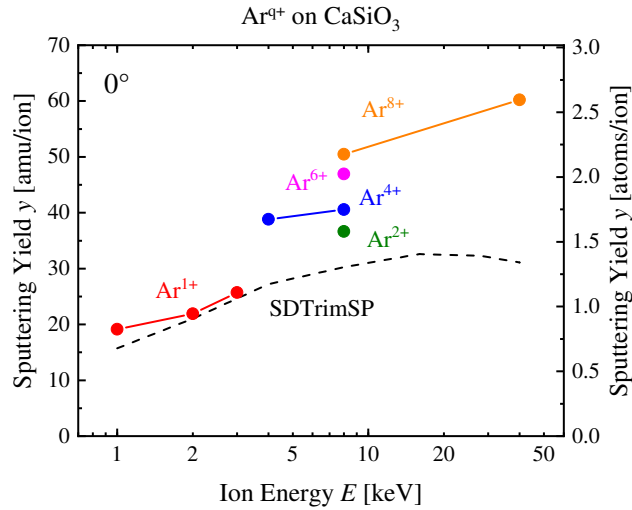


Fig. 4.17: This plot shows compilation of steady state sputtering yields of CaSiO_3 for different Ar charge states at different energies. Some measurement points for Ar^+ (no potential sputtering) are included as well as the energy dependence of kinetic sputtering from SDTrimSP simulations (dashed black line). This figure was published in an adapted form in [162].

as well as in the equilibrium (orange) are plotted over the ion's potential energy E_{pot} (values taken from the DREEBIT ionization energy database [181]). The initial potential sputtering yields are found to be proportional to E_{pot} , as indicated by the dashed green line, while the steady state yields' dependence is much less pronounced. Steady state sputtering yields were also recorded at other energies for some charge state, a respective compilation of measurement results is presented in Figure 4.17.

The potential sputtering yield per potential energy (E_{pot}) γ_{Ar} can be extracted from yield's linear dependence on E_{pot} . This gives a value of $\gamma_{\text{Ar}} \approx 147.4 \pm 29.5$ amu/keV. This is close to the 120 amu/keV for Ar and Xe on SiO_2 found by Sporn et al. [27]. However, γ_{Ar} is found to be almost twice as high as the slope γ_{He} from $^3\text{He}^{2+}$ measurements. This observation would disagree with the findings by Hijazi et al. [44], who reported a universal potential energy scaling for He and Ar ions sputtering anorthite films. However, their measurements correspond to an even lower slope with about 51.2 amu/keV. This might hint to a material dependence of the potential sputtering yield, but could also be an effect of the new differentiation between initial and steady state sputtering yields in the present work.

4.4.3 Potential Sputtering Model

Previous literature on the potential sputtering of oxides allow a qualitative explanation of the experimental observations. According to the so-called defect-mediated theory of potential sputtering, for an oxide sample only O anions are sputtered by the potential energy [27]. The electron capture causes the formation of localized electronic defects, self-trapped holes and self-trapped excitons, that promote the desorption of neutral atoms [182]. This theory has been successful in explaining the potential sputtering of alkali-halides [7, 183, 184]. Similarly, electron bombardment of SiO₂ was found to only lead to the desorption of O atoms [7, 27].

For the above presented experiments, the defect-mediated theory of potential sputtering predicts an increased sputtering of O atoms. This preferential sputtering of O would cause a depletion of O at the surface until a steady state is reached, where the effective elemental sputtering yield ratios again correspond to the bulk element ratios of Ca:Si:O = 1:1:3. Qualitatively, this image aligns with the measurements. However, a detailed calculation is required to actually check the quantitative agreement and also possibly explain the different steady state levels that were observed for He and Ar.

A model connecting changes in sputtering yields to changes in the composition of the top surface layer is applied for this purpose, similar to previously used models for potential sputtering [44, 163, 164]. It is based around following differential equations for the elemental surface concentrations C_{Ca} , C_{Si} and C_O of the wollastonite elements Ca, Si and O:

$$\begin{aligned}\frac{dC_{Ca}}{d\phi} &= \frac{1}{n_A} \left[-Y_{Ca}(\phi) + C_{Ca}^b \left(\sum_{i=Ca, Si, O} Y_i(\phi) \right) \right] \\ \frac{dC_{Si}}{d\phi} &= \frac{1}{n_A} \left[-Y_{Si}(\phi) + C_{Si}^b \left(\sum_{i=Ca, Si, O} Y_i(\phi) \right) \right] \\ \frac{dC_O}{d\phi} &= \frac{1}{n_A} \left[-Y_O(\phi) + C_O^b \left(\sum_{i=Ca, Si, O} Y_i(\phi) \right) \right]\end{aligned}\quad (4.3)$$

The change of the elemental surface concentration over fluence ϕ , which is denoted as $dC_i/d\phi$, results here from two contributions. On one hand, the concentration C_i decreases when element i is sputtered with a sputtering yield of Y_i (in the units of atoms/ion). On the other hand, the surface content of element i can be refreshed

from deeper layers. The rate of this refreshing process is given by the total sputtering yield, which is the sum over all elemental yields Y_i . The probability of an atom of element i newly reaching the top surface layer is equal to the bulk concentration C_i^b . This approach restricts composition changes to the uppermost surface layer with a number of atoms per monolayer $n_A = 1.763 \cdot 10^{15}$ atoms/cm² for wollastonite. Including a concentration gradient over depth beneath the surface would require a more detailed calculation.

For the sputtering yields Y_i , kinetic sputtering yields Y_i^{kin} are taken from SDTrimSP with an included proportionality to the surface concentration C_i :

$$Y_i^{\text{kin}}(\phi) = Y_i^{\text{SDTrimSP}} \frac{C_i(\phi)}{C_i^b} \quad (4.4)$$

Following the assumption based on reports by Sporn et al. [27], stating that the potential energy only sputters O atoms, an additional potential sputtering is included for Y_O :

$$\begin{aligned} Y_{\text{Ca}}(\phi) &= Y_{\text{Ca}}^{\text{kin}}(\phi) \\ Y_{\text{Si}}(\phi) &= Y_{\text{Si}}^{\text{kin}}(\phi) \\ Y_{\text{O}}(\phi) &= Y_{\text{O}}^{\text{kin}}(\phi) + Y_{\text{O}}^{\text{pot}}(\phi) \end{aligned} \quad (4.5)$$

Ar^{q+} measurements revealed a linear behavior of the initial sputtering yield on the potential energy E_{pot} , which is described by the slope γ . Similar to the approach by Hijazi et al. [44], twice the material's band gap E_B was chosen as a threshold for potential sputtering to occur. Together with an added proportionality to C_O , the potential sputtering term looks as follows:

$$Y_{\text{O}}^{\text{pot}}(\phi) = \gamma \frac{C_{\text{O}}(\phi)}{C_{\text{O}}^b} (E_{\text{pot}} - 2E_B) \quad (4.6)$$

Inserting equations 4.4, 4.5 and 4.6 into equations 4.3 gives a set of coupled differential equations to solve for C_{Ca} , C_{Si} and C_{O} with the additional condition of $C_{\text{Ca}} + C_{\text{Si}} + C_{\text{O}} = 1$. For comparisons with the measurements, the total sputtering yield y in amu/ion, is simply calculated by summing up the products of individual elemental sputtering yields with the respective atomic masses m_i :

$$y(\phi) = Y_{\text{Ca}}(\phi) \cdot m_{\text{Ca}} + Y_{\text{Si}}(\phi) \cdot m_{\text{Si}} + Y_{\text{O}}(\phi) \cdot m_{\text{O}} \quad (4.7)$$

By taking experimental values for $\gamma_{\text{Ar}} \approx 147.4 \pm 29.5$ amu/keV = 9.2 ± 1.8 O/keV and $\gamma_{\text{He}} \approx 81.3 \pm 20.0$ amu/keV = 5.1 ± 1.3 O/keV, the initial sputtering yield from

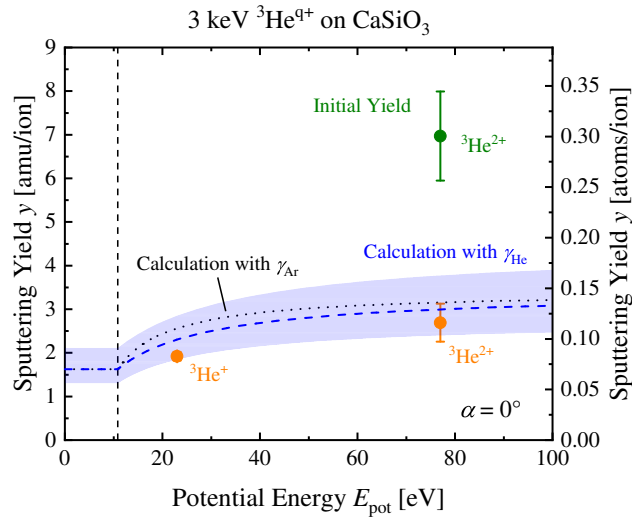


Fig. 4.18: The potential sputtering model for the steady state yields of He using γ_{He} (dashed blue line) agrees very well with the measured values (orange). A calculation with the scaling parameter γ_{Ar} also gives a good prediction for ${}^3\text{He}^{2+}$ (dotted black line), but overestimates the sputtering by ${}^3\text{He}^+$. This figure was published in an adapted form in [88].

the experiment is inserted as a starting point. It can then be checked if steady state sputtering yields $\lim_{\phi \rightarrow \infty} y(\phi)$ are correctly reproduced by the model and thus the assumption that the ions' potential energy only sputters O atoms can be tested.

Equations 4.3 were numerically solved with Wolfram Mathematica 11.2 for the cases of 3 keV ${}^3\text{He}$ and 8 keV Ar. Figure 4.18 compiles the results for ${}^3\text{He}$: Sputtering yields y are plotted over the potential energy E_{pot} , the initial yield for ${}^3\text{He}^{2+}$ is shown in green, steady state yields for both charge states in orange. The dashed blue line represents a calculation result using γ_{He} , which reproduces the experimental findings very well. The blue shaded area gives an error estimate for the calculation based on errors from determining γ_{He} as well as from SDTrimSP simulations for kinetic sputtering yields (see Figure 4.19, for He a conservative error estimate of 30% was chosen). As previously discussed, the experimental results show no universal scaling for potential sputtering. In principle, steady state values could also be reasonably well reproduced by using the same γ_{Ar} as for Ar (black dashed line). Steady state yields for He^{2+} are only 5% higher than with γ_{He} . The discrepancy of two different γ values for He and Ar could be caused by a small potential sputtering effect during the He^+ irradiation, causing some O depletion before the He^{2+} irradiation has even started. Lower O content at the surface would lead to less potential sputtering. The calculation with γ_{Ar} would then, however, predict significantly higher yields for

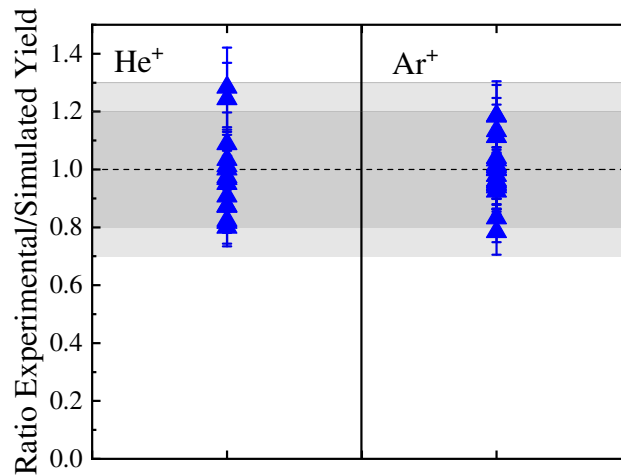


Fig. 4.19: This plot shows the ratio of experimental and simulated kinetic sputtering yields for He^+ (left) and Ar^+ (right). For the case of He, all simulations agree with measured sputtering yields within an uncertainty of 30% (light gray area), for Ar within 20% (dark gray area). These uncertainties are used as a basis for the error estimates of the potential sputtering model shown in Figures 4.18 and 4.20. This figure was published in an adapted form in [88].

singly charged He. On the other hand, different γ values for 3 keV ^3He and 8 keV Ar could be an effect of kinetically assisted potential sputtering, which might introduce an additional dependence on the kinetic energy [75]. For now, not enough data is available to definitively answer this problem. However, the comparison in Figure 4.18 makes it evident that the preferential sputtering of O due to the ion's potential energy gives a good quantitative prediction of the steady state sputtering yields. Fluences needed to reach this steady state are overestimated by a factor of about 2, which shows that further improvements to the model are still possible.

In the same way, steady state sputtering yields were calculated for 8 keV Ar and a comparison to experimental sputtering yields is presented in Figure 4.20. Initial yields are again depicted in green, while the orange squares represent the steady state yields from the measurements. The blue dashed line shows the calculation result for the steady state of 8 keV Ar at different potential energies and the model again reproduces all experimental values very well. The universal agreement for both He and Ar experiments is therefore a very strong indication that potential sputtering drives the O depletion of the surface. With the diminishing of surface O content, the potential sputtering becomes less significant. This causes the change of a linear dependence for initial sputtering yields to a less steep dependence in the steady state. Similar to the He case, the fluence dependence is not completely

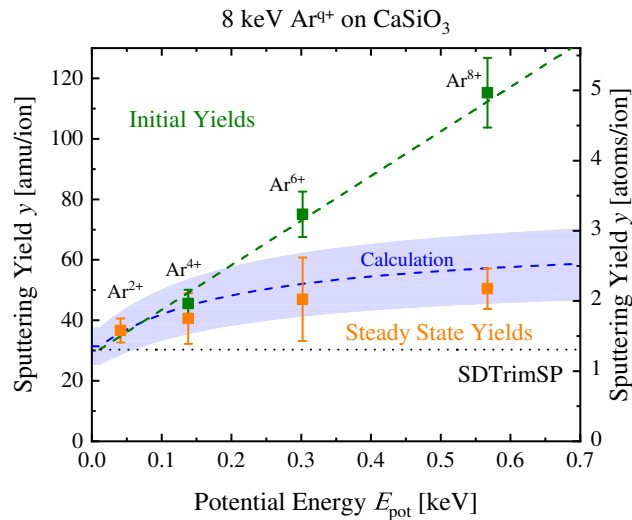


Fig. 4.20: The potential sputtering model (blue) also reproduces the steady state behavior for all investigated Ar charge states at 8 keV. It clearly shows how the linear dependence on the potential energy E_{pot} for the initial yields (green) transforms to a much less pronounced dependence in the steady state (orange). This figure was published in an adapted form in [88].

reproduced: The model overestimates the fluence until steady state by about a factor of 5. This is probably connected to concentration changes not being confined to the uppermost monolayers and an extension of the model here should be tried to find possible improvements.

In the model, one can also take a look at the predicted extent of O depletion due to potential sputtering. Figure 4.21 shows a comparison of the steady state O concentration C_{O} at different potential energies for He (red) and Ar (blue). A stark contrast is observed, where C_{O} drops much quicker for He than Ar at the same potential energy. The reason for this discrepancy can be found in the different kinetic sputtering yields compared to the potential sputtering. For He^{2+} , initial sputtering yields were about 4 times higher than for He^+ causing a quick depletion of surface O. For Ar with the same potential energy, the relative contribution of kinetic sputtering is much higher and represents an efficient way of getting more O to the surface by efficiently sputtering away surface Ca and Si. Only at Ar^{8+} , the same dominance of potential sputtering as for He^{2+} is reached and consequently, a similar steady state O concentration is reached.

The exact values predicted by the calculation should be tested experimentally to get more confidence in the oxygen concentrations, but another more important

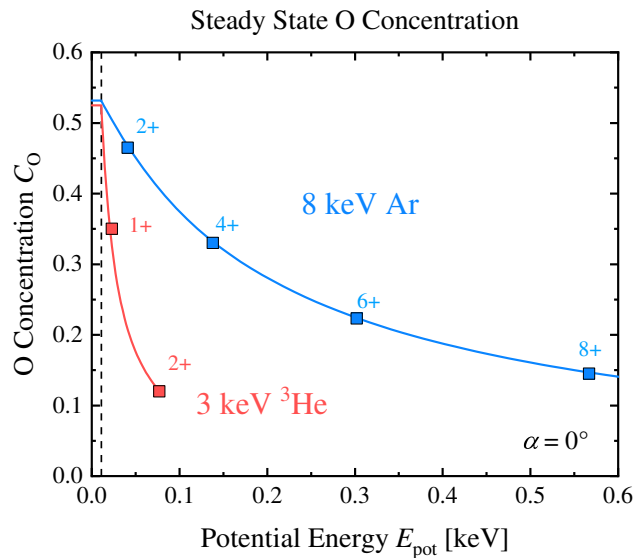


Fig. 4.21: This plot shows predictions for the steady state O concentrations for He (red) and Ar (blue) at different potential energies. At the same potential energy, the O depletion for Ar is less significant because the higher contribution of kinetic sputtering brings more O from the bulk to the surface. This figure was published in an adapted form in [88].

conclusion can be derived from Figure 4.21: Especially for the long-term space weathering behavior kinetic sputtering and potential sputtering do not act independently. Instead, the combination of different sputtering effects has to be taken into account. Initially dominant potential sputtering will quickly deplete the surface of O and not be effective in the steady state, while a significant kinetic sputtering will keep the surface O concentration higher, causing more potential sputtering in the equilibrium.

4.5 Conclusions for Solar Wind Sputtering

The interplay of kinetic and potential sputtering also plays a role for solar wind sputtering in a realistic ion impact scenario. Both major solar wind ion species, 1 keV H^+ and 4 keV He^{2+} , will significantly contribute to the total solar wind sputtering. Kinetic sputtering yields by He are about an order of magnitude higher than H yields, potential sputtering gives an even further increase that will make up a large part of the lower He fluxes. In order to investigate the expected effects for total solar wind sputtering in more detail, the fluence dependence of the sputtering of

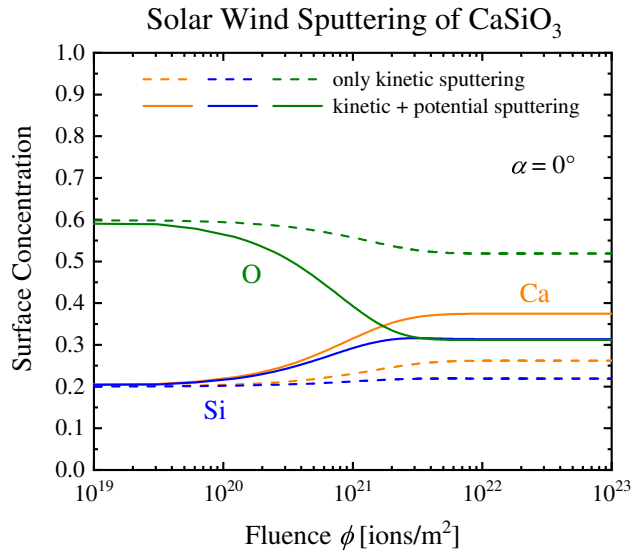


Fig. 4.22: This plot shows the development of the surface concentrations of CaSiO_3 subjected to solar wind irradiation of H^+ and He^{2+} over fluence as calculated by the potentials sputtering model. Results are shown for the complete model (full lines) as well as for a case where only kinetic sputtering is included (dashed lines). The potential sputtering by He^{2+} leads to a significant depletion of the O concentration (green).

This figure was published in an adapted form in [88].

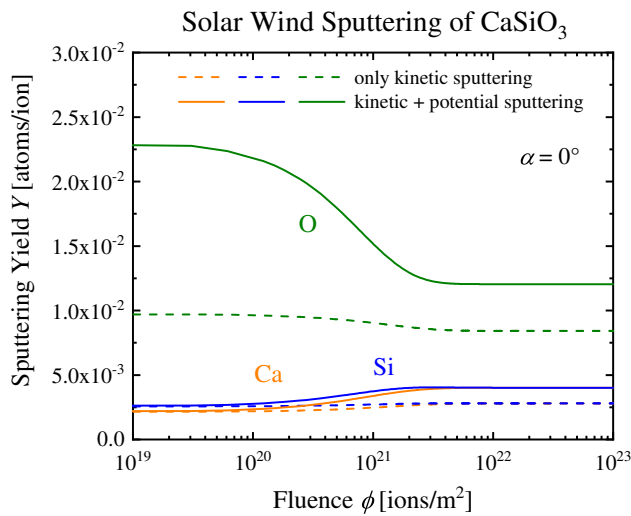


Fig. 4.23: This figure presents the sputtering yields for the different elements over fluence from the same solar wind sputtering model of CaSiO_3 as shown in Figure 4.22. The potential sputtering of O dominates for low fluences, but in the steady state all sputtering yields are increased by 43% compared to a calculation without potential sputtering.

This figure was published in an adapted form in [88].

	H	H, He (KS)	H, He (KS and PS)
C_{Ca}	0.263	0.262(-0.4%)	0.374(+42%)
C_{Si}	0.219	0.219($\pm 0.0\%$)	0.314(+43%)
C_O	0.518	0.519(+0.2%)	0.312(-40%)
Y_{Ca}	$2.34 \cdot 10^{-3}$	$2.81 \cdot 10^{-3}$ (+20%)	$4.01 \cdot 10^{-3}$ (+71%)
Y_{Si}	$2.34 \cdot 10^{-3}$	$2.81 \cdot 10^{-3}$ (+20%)	$4.01 \cdot 10^{-3}$ (+71%)
Y_O	$7.02 \cdot 10^{-3}$	$8.42 \cdot 10^{-3}$ (+20%)	$1.20 \cdot 10^{-2}$ (+71%)

Tab. 4.6: This table shows calculated steady state surface concentrations and sputtering yields of $CaSiO_3$ for a solar wind composition of 96% H^+ and 4% He^{2+} . Three cases are compared: sputtering only by H ions, kinetic sputtering by H and He ("H, He (KS)"), H and He sputtering with included potential sputtering by He^{2+} ("H, He (KS and PS)"). Numbers in brackets describe changes compared to the proton sputtering case.

This table is taken from [88].

$CaSiO_3$ under irradiation of 96% 1 keV H^+ and 4% 4 keV He^{2+} was calculated with the model described in the previous section 4.4.3. The calculation was done for normal incidence, kinetic sputtering yields were taken from SDTrimSP and potential sputtering for He^{2+} was included with the γ_{He} parameter.

The resulting effects of this solar wind sputtering to the surface concentrations of Ca (orange), Si (blue) and O (green) are shown in Figure 4.22. Results from the complete model (full lines) are compared to a calculation where only kinetic sputtering from H and He is taken into account (dashed lines). The large influence of potential sputtering becomes evident, causing a significant depletion of surface O to about 30% in the steady state. The fluence that is needed to reach this steady state is in the order of 10^{22} ions/ m^2 . At the Moon, the flux of precipitating solar wind ions is about 10^{12} ions/ m^2/s and therefore, such a fluence is reached within several 100 years. As previously discussed, some errors can be expected for the fluence dependence of the model, but the right order of magnitude should be predicted. It can therefore be estimated that the potential sputtering-related O depletion is in an equilibrium on most planetary bodies because the surface refreshing rates would need to be very high to bring enough new material to the surface within this time span.

Several other studies have performed predictions of the steady state O depletion due to potential sputtering compared to only proton sputtering. These estimations give a reduction of the surface O concentration by 22% for the lunar analogue material KREEP [163], 27% for anorthite [44] and 26% for the JSC-1A lunar regolith simu-

lant [164]. For the presented calculation, the O concentrations become lower by about 40% compared to proton sputtering (see Table 4.6), which is in line with the previous estimates. The presented findings also agree with the other studies about the O surface content reduction being nearly completely caused by He^{2+} potential sputtering.

Figure 4.23 shows the fluence dependence of the elemental sputtering yields. Again, results with only kinetic sputtering (dashed lines) and kinetic as well as potential sputtering are presented. The potential sputtering by only 4% He^{2+} significantly increases the erosion of the surface. Not only O yields are increased, but Ca and Si are also sputtered more due to their higher surface concentrations. Compared to the kinetic sputtering case, the increase is 43% for all steady state sputtering yields because the ratio of the elemental yields has to be the same as the ratio of the bulk concentrations. When compared to the case of only proton sputtering, the increase is even 71% (see Table 4.6). This value again reasonably agrees with previous estimations for KREEP (52% [163]) and anorthite (46% [44]). The new differentiation between initial and steady state sputtering yields in this thesis will play a significant role for the existing discrepancies that are observed to other studies.

The above presented calculation results once again show the need for potential sputtering to be taken into account for space weathering research. Not only will surface concentrations be affected, but the flux of sputtered material into the exosphere will also be significantly increased for all elements - given an equilibrium state. Further effects can also be expected by the solar wind minor ions that are heavier and have higher charge states. These properties could therefore also somewhat compensate their small abundances, for example, Nénon et al. estimate the contribution to total sputtering by ions heavier than He to be between 8% and 14% [149].

4.6 Discussion and Outlook

Using wollastonite (CaSiO_3) as the main analogue samples for the surfaces of the Moon and Mercury, a wide range of ion-interaction effects with different ion species was investigated to assess the interaction of the solar wind with planetary surfaces.

Sputtering yields were measured with the major solar wind ions as well as for heavier minor solar wind ions. Detailed experiments were performed under an array of different angles of incidence, where a steeper angular dependence of the sputtering yield was found than was previously assumed [99]. This will affect the sputtering of rough surfaces, where a distribution of local incidence angles always determines the sputtering yield. Comparison with the commonly used SRIM program show, that its simulated sputtering yields have to be expected to be off by a factor of 2. Using the different BCA program SDTrimSP, a set of input parameters was optimized to consistently reproduce total kinetic sputtering yields of silicate film samples. This will be helpful for future space weathering models, which still heavily rely on such simulations.

Potential sputtering of He^{2+} and multiply charged Ar ions was investigated, showing the dynamic process of potential sputtering on planetary analogs for the first time. Modelling efforts support that this transient behavior is driven by a preferential sputtering of surface O in accordance with the defect mediated theory of potential sputtering. The amount of O that is depleted from the surface determines the sputtering yields in the steady state, which means that kinetic and potential sputtering cannot be regarded completely separated from each other. For the H and He solar wind components, the total sputtering increase due to potential sputtering was calculated to be 43%, showing that He^{2+} is a very important contribution to space weathering.

Using the advantages of the QCM system, implantation of ions into planetary analogs could also be observed. Implantation is of particular interest for solar wind protons, which are assumed to be a key driver for OH and water cycles on the lunar surface [185]. Maximum local concentrations of about 30% for H and about 6% for He were found. For a solar wind irradiation scenario, these values will correspond to maximum possible concentrations. The complex dynamic of low solar wind fluxes and varying temperatures will lead to diffusion and desorption of previously implanted solar wind ions. However, permanently shadowed regions might indeed have regolith grains with solar wind-saturated rims.

So far, these investigations have been done with thin amorphous films deposited from minerals of interest for planetary surfaces. The achieved results are conform with previous investigations, where the possibility of comparison exists. Nevertheless, an important focus for future solar-wind-interaction studies will be the

use of more realistic pellet targets from pressed mineral powder. Here additional properties of the lunar and hermean regolith will be better reflected such as the crystal structure, grain size or porosity and it will be possible to investigate how these quantities influence the interaction with solar wind ions. Sputtering yield measurements will be performed with an upgraded catcher setup compared to the work by Berger et al. [56], so that the advantages of the QCM technique can also be applied for different samples. Beyond the investigation of sputtering, a further look should be taken into the implantation of ions in planetary surfaces. While proton implantation has been an established topic of research for OH and H₂O formation, recent space observations and calculations have also put the spotlight on the implantation of heavier ions. For example, it has been assumed that traces of planetary atmospheres will be in bodies like the Moon or Phobos [186, 187, 188]. While signs of O implantation were observed for Phobos analogs (see next chapter), additional experiments that can directly trace implanted ions in planetary analogs will give important understanding to the possibilities of regolith as historic records of ancient planetary atmospheres.

Results: Sputtering of Phobos by Martian Atmospheric Ions

This chapter describes research on the space weathering of Phobos by planetary ions from the Martian atmosphere. First a more detailed introduction into this topic is given in section 5.1, as well as previous research on the expected space weathering effects for the larger of the two Martian moons. Section 5.2 presents analysis results for the used samples. Section 5.3 discusses sputtering by atomic O ions followed by results on molecular O₂ ions in section 5.4. Implications for other molecular ions that might play a role are presented in section 5.5, before the general consequences for the space weathering of Phobos are summarized in section 5.6.

Large parts of the work presented in this chapter have been published in [87].

5.1 Introduction

As discussed in the previous chapter, space weathering by ion impact is a current topic of investigation on the planet Mercury and the Moon for its cause of surface modification and exosphere formation. However, it also plays a role in the development on much smaller bodies, such as the Martian moon Phobos. Phobos only has a diameter of about 11 km and its irregular shape is more reminiscent of an asteroid than the moons of other planets (see Figure 5.1). The origins of Phobos and the other Martian moon Deimos are still unclear, but from observations of their cratered surfaces have led to the assumption that both bodies are several billion years old [189]. One theory of their formation is that Phobos and Deimos are asteroids that were caught in the Martian gravitational field. This theory is supported by Phobos' spectral features, which were found to be similar to those of D-type asteroids [190, 191]. Another theory assumes the origin of the Martian moons in a collision of Mars with another body [192], which could have had about a thousandth of the mass of Mars [193]. Such a scenario would be similar to the favored theory of the origin for Earth's Moon on a smaller scale [194]. Recent simulation studies on the



Fig. 5.1: This image of Phobos from the Mars Reconnaissance orbiter shows its shape and cratered surface.

Image Credit: NASA / JPL-Caltech / University of Arizona

development of the orbits of Phobos and Deimos indicate that both moons originated from a common body [195], but much of their history is still unknown.

To further investigate the possible origins of Phobos, knowledge on its composition is essential. Spacecrafts such as the JAXA's Martian Moons eXploration (MMX) mission (launching in the mid-2020s) will provide essential insights by returning a soil sample from Phobos to Earth [196]. Remote measurements of Phobos mostly probe its surface, which has been changed by space weathering. Interpretation of these analyses therefore requires an understanding of the space weathering processes on Phobos. These processes are also of interest for the MMX mission and its possible sample pickup locations. Phobos is tidally locked, which leads to the same side always facing Mars, and this will result in locally very different space weathering histories [197].

Space weathering of Phobos was modelled by Cipriani et al., who found that sputtering by solar wind H^+ and He^{2+} ions mostly dominates over micrometeorite vaporization [199]. Poppe and Curry later proposed that planetary ions escaping from the Martian atmosphere also significantly contribute to the sputtering of the surface of Phobos [200]. Such planetary ions are mostly created by photoionization in the upper atmosphere layers and subsequently accelerated [201, 202]. These atmospheric losses primarily affect O, O_2 and CO_2 [203], due to oxygen being more abundant in the upper atmosphere of Mars than the otherwise strongly dominant

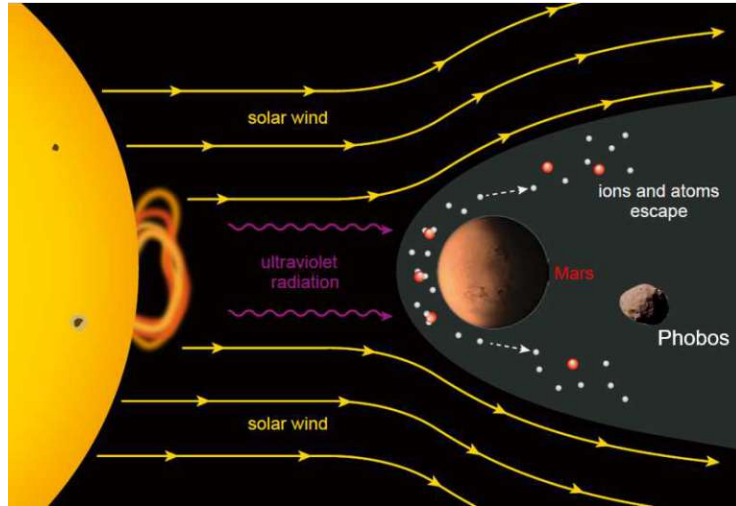


Fig. 5.2: This sketch illustrates the space weathering on Phobos, when it moves through the Martian magnetotail. Due to its proximity to Mars, the planet shadows the solar wind efficiently from reaching the surface of Phobos. Instead it is sputtered by O ions escaping from the Martian atmosphere. This image is adapted from [198], (C) Sterne und Weltraum.

carbon-dioxide [204, 205]. Nénon et al. continued the modeling of sputtering of Phobos basing their calculations on analysis results of the ion environment around Phobos from the MAVEN mission [206, 207]. They found that Phobos is indeed mostly sputtered by solar wind ions on its orbit around Mars. However, when Phobos passes through the Martian magnetotail, the solar wind is shadowed from reaching the surface of the moon due to its proximity to Mars of about 6000 km. Additionally, Phobos' surface is impinged by a stream of planetary atomic and molecular oxygen ions with energies up to several 10s of keV [206], with this scenario being sketched in Figure 5.2. According to modeling by Nénon et al. [206], the sputtering by O ions massively dominates the sputtering from the shadowed solar wind in the Martian magnetotail region and this effect mostly concerns the Mars-facing side of Phobos [197].

For their calculations, Nénon et al. use sputtering yields by O ions for monoatomic Ni targets [206] or SRIM simulations [197] as inputs due to there being no measurements with relevant analog samples available. For these sputtering inputs, the authors estimate an error of about a factor of 2 [206]. Additionally, there is no information available on possible chemical sputtering or O ion implantation. The sputtering by molecular ions should also be quantified because atomic and molecular oxygen ions were estimated to contribute a similar amount of sputtering [206].

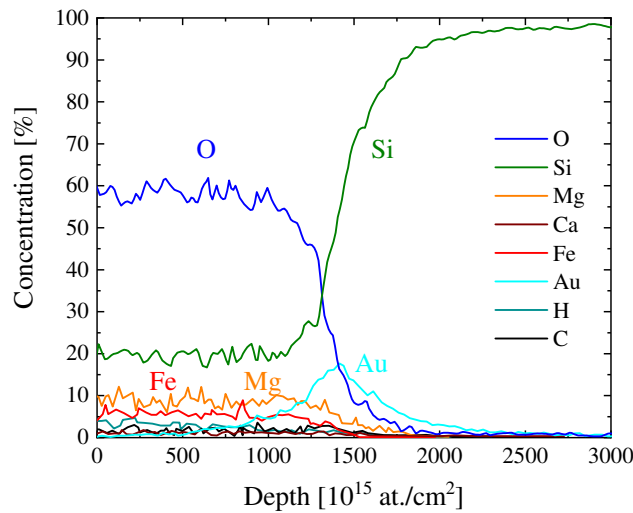


Fig. 5.3: This plot shows an example of IBA results for an augite film on a Au-covered Si wafer piece, which was coated in PLD at the same time as a QCM sample. ToF-ERDA analysis shows a uniform film composition as well as elemental concentrations close to the expected values. The transition to the Au interlayer and the Si substrate are clearly visible, but smeared out due to limits in the depth resolution.

Molecular sputtering effects could also have implications for CO_2 ions, which have been neglected so far due to their low fluxes in the MAVEN measurements.

For this reason, ion irradiation experiments with O^+ , O_2^+ , C^+ and CO_2^+ ions and thin augite films as analogs for the surface of Phobos were performed [87]. The results of these investigations are described in the following sections.

5.2 Sample Preparation Parameters and Analysis Results

For the investigation of space weathering of Phobos by planetary ions, thin films deposited on a QCM from the Mg- and Fe-rich pyroxene mineral augite $(\text{Ca,Mg,Fe})_2\text{Si}_2\text{O}_6$ were used. The original mineral was cut and polished by R. Miletich-Pawliczek at the Institute of Mineralogy and Crystallography at the University of Vienna. Film deposition was done with PLD at the Institute of Chemical Technologies and Analytics with a 248 nm KrF laser. Pulse frequencies of 5 Hz were chosen as well as a pulse energy of $1 \text{ J/cm}^2/\text{pulse}$. The deposition time was 60 minutes and the sample was

	Ca	Mg	Fe	Si	O
Augite	1.8 ± 0.1 %	8.9 ± 0.3 %	6.0 ± 0.2 %	20.5 ± 0.5 %	60.3±0.9 %
Phobos	0.1 %	14 %	9 %	11 %	64 %
	H	C	Al	Na	
Augite	1.4±0.1 %	1.1±0.1 %	-	-	
Phobos	-	-	1.5 %	0.5 %	

Tab. 5.1: This table shows a comparison between the compositions of the augite samples (average from two films analyzed with ToF-ERDA) and Phobos' surface. Mg, Fe, Si and O represent the most significant elements both in the samples as well as in the estimations for Phobos.

This table is adapted from [87], augite analysis results were reported in [86], Phobos atomic elemental abundances are taken from [200] based on [199, 208].

kept at a temperature of 300 °C.

IBA of two different augite film samples was done at Uppsala University with RBS using a 2 MeV He⁺ beam and ToF-ERDA with a 36 MeV I⁸⁺ beam. On the samples, areal densities of $1100 \cdot 10^{15}$ atoms/cm² and $1270 \cdot 10^{15}$ atoms/cm² were observed, which correspond to film thicknesses between 120 nm and 139 nm when the density of the close, well-defined pyroxene end member enstatite (Mg₂Si₂O₆) of 3.3 g/cm³ is assumed [86]. The compositions of the samples were found to be homogeneous across a large part of the film (see Figure 5.3 for an analysis example) and close to the nominal pyroxene composition of 20% Si and 60% O content (see Table 5.1). Mg and Fe contributions dominate over Ca and contamination of H (1.4%) and C (1.1%) was found to be small. Table 5.1 also contains an estimation for the elemental abundances on the surface of Phobos based on asteroid compositions [199, 208], which was taken as the input by Poppe and Curry to model the space weathering of Phobos [200]. Absolute values vary compared to the augite sample, but the major elements are reflected well, which validates using the thin augite films as an analog for the surface of Phobos.

AFM images were recorded to assess the surface roughness, where a root mean square (RMS) roughness of 5.6 ± 3.5 nm was observed [86]. This is low enough to mostly neglect the influence of roughness on sputtering [158], which was validated during Ar and He irradiations of samples from the same deposition batch [86]. An augite sample was also analyzed in a polarization microscope and an amorphous structure was observed, similar to the wollastonite samples due to the comparably

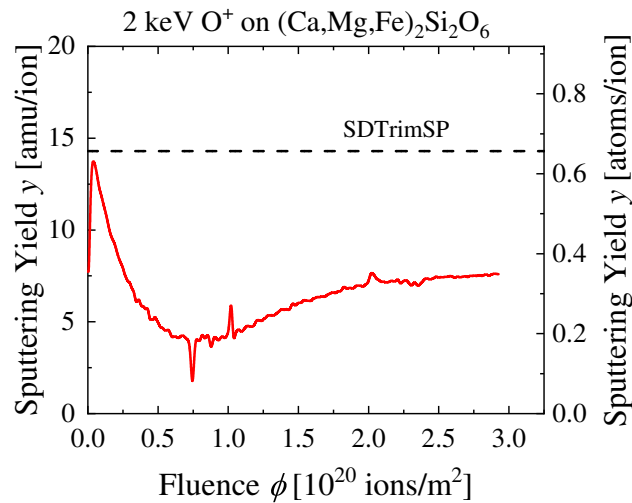


Fig. 5.4: This image shows the fluence dependent QCM measurements during a 2 keV O^+ irradiation of augite under normal incidence converted into sputtering yield y in amu/ion. Experimental results (red full line) are compared to a static SDTrimSP simulation (black dashed line) as a reference. This figure was published in [87].

low sample temperature during deposition.

5.3 Sputtering by Atomic Oxygen Ions

5.3.1 Measurement Results

After cleaning the augite sample with 2 keV Ar^+ ions under 0° or 60° , the samples were irradiated with 2 keV O^+ ions under normal incidence and a significant fluence dependence was observed in the QCM signal. Figure 5.4 shows an example for such a fluence dependence, where the sputtering yield y as derived from the measured mass change is plotted. The experimental value (red) decreases at first, only to then increase again and become stable after several $10^{20} O/m^2$. A static SDTrimSP simulation is included in Figure 5.4 (dashed black line), which shows that even in the steady state the measured value is lower than the simulation. Further O irradiations did not reveal any other fluence dependent behaviors, but the initial fluence dependence shown in Figure 5.4 could be reproduced after the target was sputtered with Ar^+ ions.

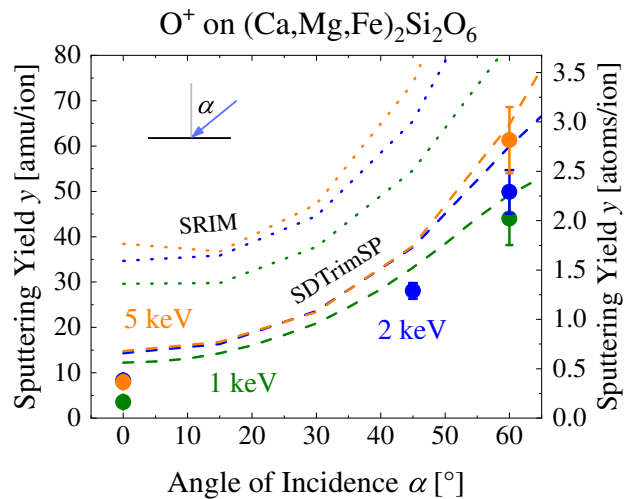


Fig. 5.5: The angular dependence of the sputtering yield of augite under O^+ irradiation was measured (dots) for 1 keV (green), 2 keV (blue) and 5 keV (orange). For comparison, simulations with SRIM (dotted lines) and SDTrimSP (dashed lines) are included.

This figure was published in [87].

From the steady state reached by prolonged O^+ irradiation, the sputtering yields under different angles were recorded. Figure 5.5 compiles the measurement results for O^+ ion irradiation at 1 keV (green), 2 keV (blue) and 5 keV (orange). The sputtering yields slightly increase with energy and show a pronounced angular dependence, similar as it was observed for other projectiles on wollastonite (see chapter 4).

Figure 5.5 also includes simulations with SRIM and SDTrimSP for the different O ion energies. SRIM simulations with the augite composition from ToF-ERDA (see Table 5.1), shown as the dotted lines massively overestimate the sputtering of augite by O^+ ions for all angles and energies, which agrees with the findings for wollastonite presented in chapter 4. SDTrimSP with the adapted input parameters and ToF-ERDA analysis inputs for the composition gives a much better agreement for the sputtering by O ions, as is shown by the dashed lines. For these simulations, surface binding energies and densities were adapted following the same procedure that was used for consistent descriptions of wollastonite sputtering yields (see section 4.3.1), with the density being approximated by the enstatite density of 3.3 g/cm^3 [86]. These simulation inputs were also applied by Biber et al. for similar augite samples [86], where the interaction with He ions could be very well simulated. For the O^+ irradiations shown in Figure 5.5, SDTrimSP also significantly better reproduces the measured values compared to SRIM. However, there are still differences visible as

	Averaged difference (absolute) (amu/ion)
1 keV O ⁺	8.54 ± 2.71
2 keV O ⁺	6.46 ± 2.49
5 keV O ⁺	6.70 ± 3.24

Tab. 5.2: The overview of the difference between experimental and simulated results for the sputtering yields shows that they are similar for all investigated angles and energies.

This table was adapted from [87].

the measured sputtering yields are consistently lower than the SDTrimSP results (see Table 5.2). These differences are similar for all angles, even though the larger absolute errors for the 60° measurements have to be noted.

5.3.2 Discussion

The observed offsets between experimental results and SDTrimSP simulations allow several possible explanations: Different sputtering effects could play a role for O irradiations, SDTrimSP might not be as suitable for simulating augite as it is for wollastonite or implantation of O could be taking place counteracting the mass changes caused by sputtering.

In order to investigate a general behavior under O irradiation, the sputtering yields of wollastonite (CaSiO₃) were also measured under O⁺ irradiation. Their angular dependence is plotted in Figure 5.6 for 2 keV (blue) and 5 keV (orange). SRIM simulations are included as dotted lines and SDTrimSP simulations are shown as dashed lines. Contrary to the experiments with augite targets, measurements and SDTrimSP simulations show a very good agreement for both energies at all angles. This observation coincides with previously presented findings for wollastonite with other projectiles (chapter 4). These measurements also show that there are per-se no indications for a fundamentally different sputtering behavior for O⁺ projectiles. When the sputtering yields by 2 keV O⁺ ions are compared for the two different materials (see Figure 5.7), it becomes evident that SDTrimSP predicts practically identical yields. This is caused by the small compositional differences between wollastonite (CaSiO₃) and augite ((Ca,Mg,Fe)₂Si₂O₆). The only outlier in Figure 5.7 are the measurement results for augite.

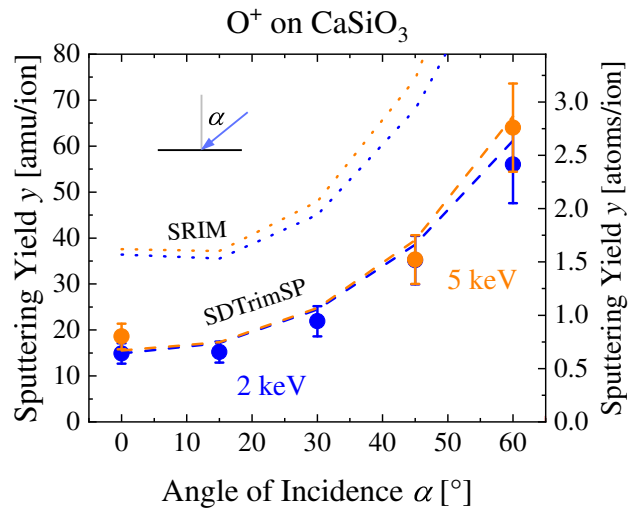


Fig. 5.6: Sputtering yields of wollastonite irradiated with 2 keV (blue) and 5 keV (orange) O⁺ ions are compared to simulation results. SRIM (dotted line) again overestimates the sputtering, SDTrimSP (dashed lines) with adapted input parameters reproduces the experimental values (dots) very well in accordance to experiments with other projectile species. This figure was published in [87].

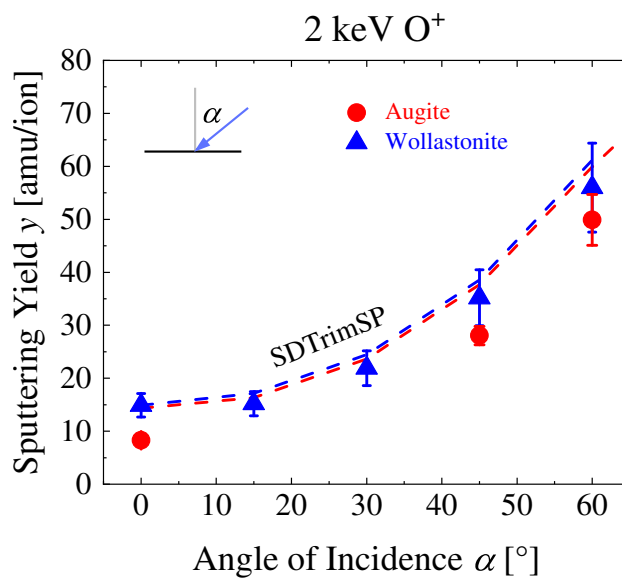


Fig. 5.7: When sputtering yields for 2 keV O⁺ are compared for augite (red) and wollastonite (blue), SDTrimSP (dashed lines) shows the same results for both materials. The measured yields for augite do not fit to this prediction. This figure was published in [87].

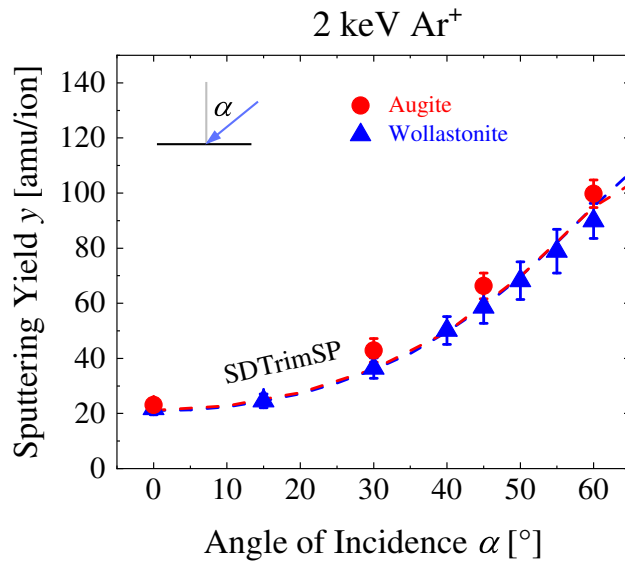


Fig. 5.8: For 2 keV Ar⁺, SDTrimSP (dashed lines) again predicts almost identical sputtering behaviors for wollastonite (blue) and augite (red). Contrary to the O irradiations, this is also observed in the experiment (dots). This figure was published in [87].

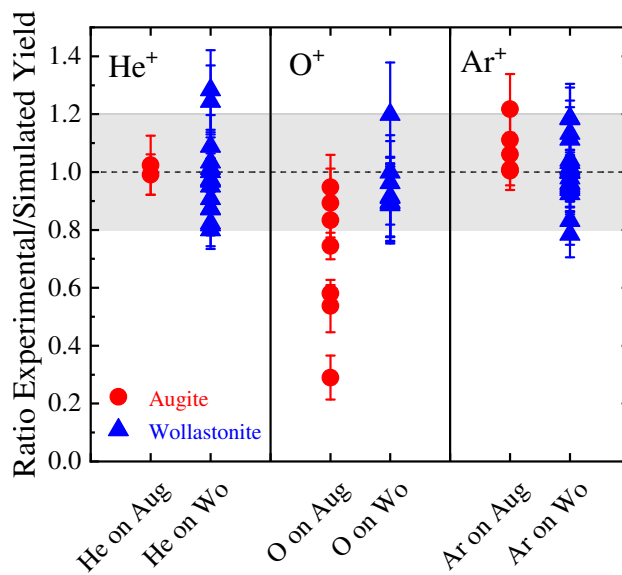


Fig. 5.9: When the ratio of experimental to simulated sputtering is compared for both materials and for He, O and Ar projectiles, the sputtering of augite by O⁺ is the only projectile-target combination showing a different behavior. This figure was published in [87].

To further check the accuracy of SDTrimSP simulations for augite, additional 2 keV Ar⁺ irradiations were performed. The sputtering yields at different angles are presented in Figure 5.8 as the red dots, where they are shown together with wollastonite measurements (blue triangles) and SDTrimSP simulations (dashed lines). Again, SDTrimSP simulations result in very similar sputtering yields for both targets, but now this behavior is also in very good agreement with the measured sputtering yields for both sample materials. In general, the ratio of experimentally observed sputtering yields and simulation results from SDTrimSP give a consistent agreement (see Figure 5.9), with the only outlier being again the O⁺ irradiations of augite. These measurements can thus not be explained by fundamentally different target properties such as the surface binding energies or densities. SDTrimSP simulations with the optimized input parameters should also be valid for simulating the kinetic sputtering of augite.

These observations indicate a different effect playing a role for the sputtering of augite by O ions. The most likely explanation is the implantation of O ions in the sample. As shown for He⁺ irradiations of augite samples [86], QCM measurements can show a significantly different behavior at the beginning of an irradiation if ion implantation occurs. A QCM measurement only allows direct insights on the mass change of the sample and the mass depletion per ion from sputtering at low keV energies is in the same order of magnitude as the ion's mass. For example, the observed differences in augite experiments and simulations shown in table 5.2 would correspond to an implantation of about 40 to 50% of the impinging O ions. Implantation could also offer an explanation for the close-to-constant offsets over different angles of incidence, as a less pronounced angular dependence of the implantation probability can be expected.

In order to investigate the effect of implantation, dynamic SDTrimSP simulations were performed for O irradiations of augite. The mass changes of the target were calculated from the mass depletion by sputtering and the mass increase by implantation. Figure 5.10 shows the fluence dependence originally depicted in Figure 5.4 in red, but it is now compared to the net mass depletion calculated from such a dynamic SDTrimSP simulation (blue). In this simulation, the maximum local O concentration was limited to 67%, similar as for the SDTrimSP simulations of H irradiation of wollastonite (section 4.3.2). At the beginning of the irradiation, all O ions get implanted and a net mass increase is predicted. This behavior clearly contradicts the findings in the experiment indicating the presence of another effect. However, for fluences higher than 10²⁰ ions/m² both the fluence dependence and

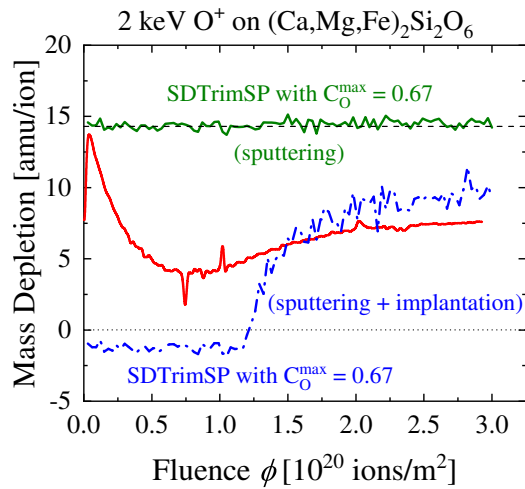


Fig. 5.10: The experimental fluence dependence for 2 keV O^+ irradiations of augite under normal incidence (red) is compared to a dynamic SDTrimSP simulation, where both sputtering and O implantation up to a local concentration 67% are included (blue). The agreement towards the steady state is much improved. This is largely attributed to changes in the O implantation behavior, as the sputtering contribution mostly stays constant in the same simulation (green). This figure was published in [87].

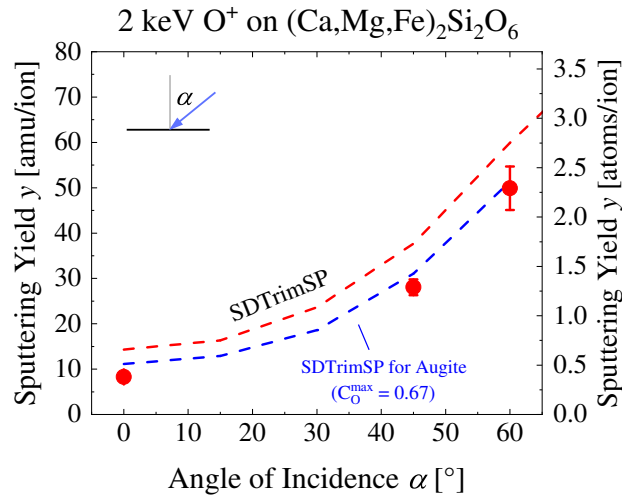


Fig. 5.11: For different angles of incidence, the dynamic simulations with included O implantation (blue) consistently improve the agreement with the measured values (red) for the sputtering of augite under 2 keV O^+ irradiation. This figure was published in an adapted form in [87].

the absolute values agree quite well with the experiment. At this fluence, local saturation occurs as the artificial limit of 67% concentration is reached. As a result, the amount of implanted O ions decreases and the net mass depletion increases. The implantation of O ions does, however, not completely go to zero because in the steady state a dynamic equilibrium is formed, where both implantation and sputtering still occur. The green line shows the mass depletion contribution from the same simulation just from sputtering, which is constant. The composition changes due to preferential sputtering and O implantation are too small to significantly affect the sputtering behavior. The changes of the mass depletion per ion in the simulation are thus only caused by the change of implantation behavior. Figure 5.11 depicts the steady state results from dynamic SDTrimSP simulations with O implantation as the blue line and the agreement is consistently improved for all angles. This would mean that the measured sputtering yields appear lower than the actual sputtering as there always occurs some implantation, which affects the QCM measurement. While a direct detection of implanted O should also be aimed for in the future, for example by IBA of implanted ^{18}O , the simulation of implantation gives a consistent description of otherwise unexplained behavior in the experiment.

Comparison with the wollastonite experiment shows that O ion implantation as observed for augite is not universal for silicate minerals. The presence of Ca, Si and O in the sample is not sufficient for O implantation to occur. Mg and Ca can be expected to act similar as both elements are earth-alkalines. For augite, this would only leave its Fe content as responsible for O implantation. The additional O content needed for 67% atomic concentrations would be similar to the Fe in the sample changing from FeO bonds to Fe_2O_3 bonds. In a recent publication, the presence of hematite (Fe_2O_3) on the Moon was reported [187], which was attributed to be caused by O ions from an earth wind similar to the O ion precipitation on Phobos. The authors state that additional reduction processes from solar wind H^+ are necessary for the hematite formation to occur. However, Kuhlman et al. showed that the formation of Fe nanoparticles also occurs under He irradiation and not only under H irradiation [209]. Similarly, keV O^+ ions could also cause the nucleation of Fe nanoparticles themselves, which could then react to stopped O ions to form Fe_2O_3 . Such a process could even explain the observed fluence dependence, where Fe nucleation has to occur first to make O implantation possible. However, this explanation is contested by the Ar irradiations before the O irradiations. Both ions have similar ranges and thus similar volumes of interaction and the Fe nanoparticle formation would therefore already have started before the O irradiations. As stated

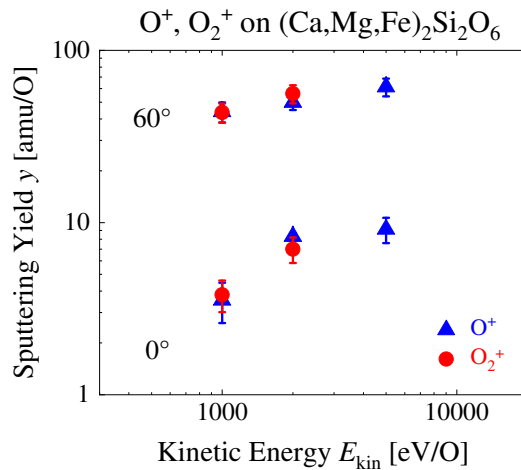


Fig. 5.12: The comparison between measured sputtering yields of augite for atomic (blue triangles) and molecular (red dots) O ions shows a coinciding sputtering behavior in respect to the number of O atoms in the ion. In the investigated energy ranges, molecular effects are thus negligible for O ions. This figure was published in [87].

before, ideally further in-situ analysis could help clear up the occurring processes.

5.4 Sputtering by Molecular Oxygen Ions

In their analysis of Mars Atmosphere and Volatile Evolution (MAVEN) measurements, Nénon et al. found that the flux of O_2^+ ions is similar to the flux of O^+ ions [206]. For evaluating sputtering yields by those O_2^+ ions, they neglected any molecular effect and it was assumed that a molecular ion behaves the same as two independent atomic ions at half the energy. This assumption is reasonable if the molecular ion immediately dissociates upon impact and was found to be valid for molecular ions in the low keV range [177]. For slower ions, molecular dissociation might not happen immediately and for faster ions additional sputtering effects due to overlapping collision cascades will occur [177, 210, 211, 212]. However, irradiations with molecular O ions should also be performed for O_2 ions on silicate targets to test whether molecular effects play a role for space weathering processes.

Irradiations of augite with O_2^+ ions were performed at kinetic energies of 2 keV and 4 keV under normal incidence and 60° incidence. The measurement results are compared to those with O^+ ions in Figure 5.12. Both the yields and energies are

plotted in respect to each O atom in the ion. For all investigated cases, there exists a good agreement for atomic and molecular O ions showing that an O₂ ion behaves the same as two O ions at the same velocity in the low keV range, which contributes a significant part to the sputtering on Phobos [206]. These results therefore indicate that the assumption of negligible molecular effects is also reasonable for the sputtering of Phobos.

5.5 Contributions from other Molecular Ions

Fluxes of other molecular ions hitting the surface of Phobos will be much lower than for O ions [206]. However, some CO₂⁺ ions will impinge the surface of Phobos. Recent new analysis of MAVEN measurements also shows significant atmospheric escape of ions with a mass between 28 and 31 amu [213], even though only energies up to 100 eV were analyzed. For the space weathering of Phobos, it is of interest to check whether any unexpected sputtering effects could occur here or if their contributions are negligible to the total sputtering of the surface of Phobos.

5.5.1 Measurements with C⁺ and CO₂⁺ ions

Measurements of the sputtering yield of augite under the irradiation of C⁺ and CO₂⁺ were performed under different angles of incidence. Results for C⁺ irradiations as a basis for subsequent experiment with CO₂⁺ are shown in Figure 5.13. Sputtering was measured under 0° and 60° for 2 keV (blue) and 5 keV (orange) and is compared to simulations with SRIM (dotted lines) and SDTrimSP (dashed). The observed behavior is comparable to the O⁺ measurements indicating that C⁺ ions are also implanted in augite, even though no saturation was observed in the experiments. In contrast to irradiations with O ions, lower sputtering yields than expected from SDTrimSP are now also observed when wollastonite is irradiated with C⁺ ions, as is shown in Figure 5.14. The experimental values were recorded after initial irradiation up to a fluence of 1.6×10^{20} C/m². Almost constant shifts to lower measured mass depletion in the experiment occur for 2 keV (green) and 5 keV (orange) in comparison to SDTrimSP (dashed lines). For both targets, SRIM once more significantly overestimates the sputtering yields in accordance with observations for most other projectiles.

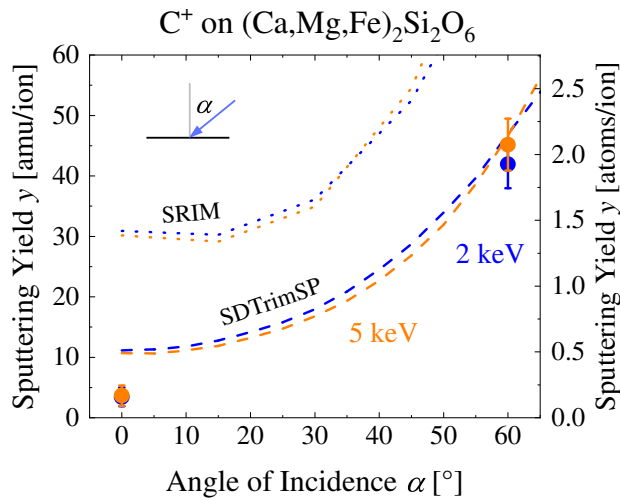


Fig. 5.13: The angular dependence of the sputtering yields for C^+ irradiations of augite (dots) is compared to SDTrimSP (dashed lines) and SRIM simulations (dotted lines). Yields are almost identical for 2 keV (orange) and 5 keV (blue). Lower measured values at normal incidence indicate C implantation as it was similarly observed for O projectiles. This figure was published in [87].

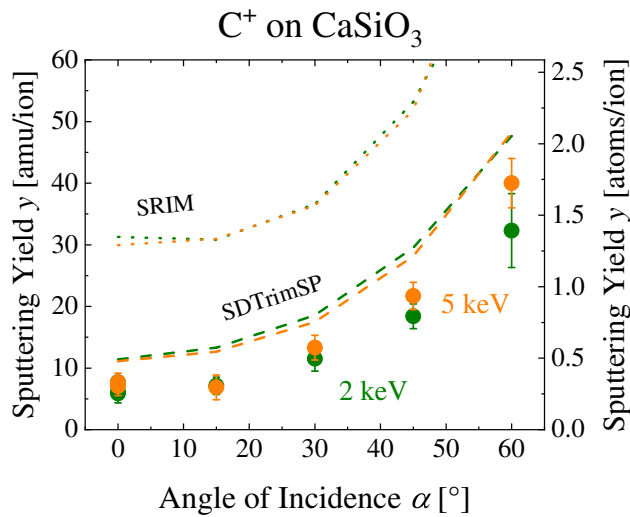


Fig. 5.14: With C^+ ions, implantation is also observed for the irradiation of wollastonite. Experimental values (dots) for 2 keV (green) and 5 keV (orange) are consistently lower than SDTrimSP simulations (dashed lines).

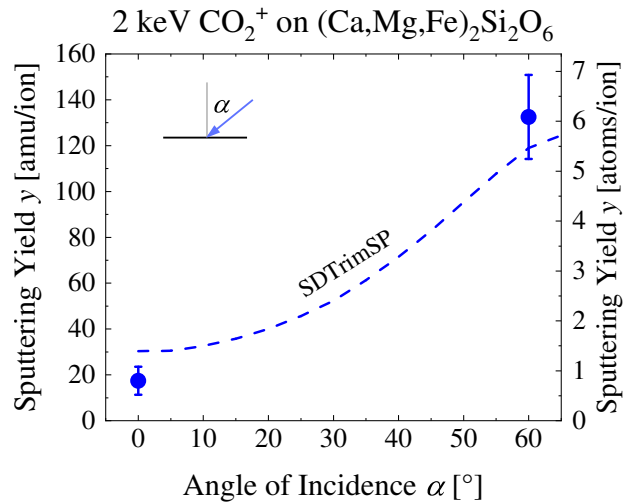


Fig. 5.15: For 2 keV CO_2^+ irradiations under normal incidence and 60° , the experimental values (dots) are close to simulated sputtering when molecular effects are disregarded (dashed lines). This is calculated by summing up individual SDTrimSP results for one C and two O atoms at the same velocity as the CO_2 ion (corresponding to 545 eV for C and 727 eV for O). This figure was published in [87].

With the basis of O^+ and C^+ experiments, augite samples were also irradiated with 2 keV CO_2^+ ions under 0° and 60° . QCM measurement results are compared to an SDTrimSP simulation in Figure 5.15. For the simulation, it was again assumed that no molecular effects play a role and the three atomic constituents split up upon impact and keep their velocity. Therefore, the curve represents the sum of sputtering by a 545 eV C ion and two 727 eV O ions. The achieved agreement with the experiment is reasonable, as can be seen in Figure 5.15. Normal incidence measurements are again lower, probably due to the implantation that was also observed for O and C ions. What is more relevant for CO_2^+ ions hitting Phobos, is that its sputtering has not been fundamentally underestimated before. Therefore, the low fluxes of CO_2^+ reaching Phobos will not significantly contribute to the space weathering of the Martian moon. Instead, it is reasonable to primarily consider O^+ and O_2^+ ions for space weathering models.

5.5.2 Simulations of Sputtering by Molecular Ions

As discussed previously, the differences between experiment and SDTrimSP simulation can be attributed to ion implantation effects. Then SDTrimSP simulations give

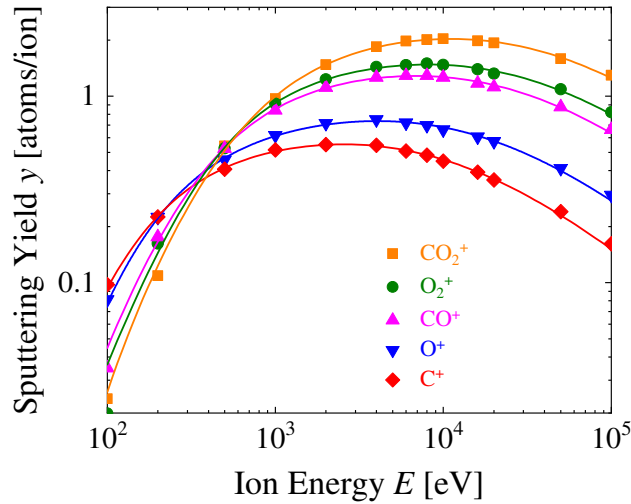


Fig. 5.16: This figure shows simulated sputtering yields under normal incidence for C^+ , O^+ , CO^+ , O_2^+ and CO_2^+ ions. SDTrimSP simulations (symbols) are included as well as fits by equation 5.1. The resulting fitting parameters are shown in table 5.3. This figure was published in [87].

very good representations for the sputtering of silicate targets, even for molecular ions as no signs of significant molecular effects were found in the low keV range. To provide possible sputtering inputs for future investigations, sputtering yields for augite at a wide energy range were simulated for different ions consisting of C and O atoms. Figure 5.16 show the total sputtering yields in atoms/ion for different projectiles and different energies at normal incidence, the dots represent SDTrimSP results. C^+ and O^+ results are directly derived from the simulations, sputtering yields by CO^+ , O_2^+ and CO_2^+ bombardment are calculated as the sum of the yields from the atomic constituents at the same impact velocity. The energy dependence of the sputtering yields shows a typical behavior with a maximum in the low keV range.

The full lines shown in Figure 5.16 represent fits to the simulated data with a formula from Eckstein and Preuss [16], which is very well suited for fitting the energy dependence of kinetic sputtering yields. Following the description in [16], the fitting formula for the sputtering yield Y dependent on the incident energy E looks as follows:

$$Y(E) = q s_n^{\text{KrC}}(\varepsilon) \frac{\left(\frac{E}{E_{\text{th}}} - 1\right)^\mu}{\lambda + \left(\frac{E}{E_{\text{th}}} - 1\right)^\mu} \quad (5.1)$$

	q	λ	μ	E_{th}	ε_{L}
C^+	1.43484	13.4059	1.45022	22.7426	1.26802×10^{-4}
O^+	1.89964	20.3068	1.50222	22.882	7.55614×10^{-5}
CO^+	3.32419	69.2758	1.5104	21.2016	4.57931×10^{-5}
O_2^+	3.81371	335.877	1.64781	12.0068	3.7848×10^{-5}
CO_2^+	5.27316	41.0917	1.4027	39.2853	2.89859×10^{-5}

Tab. 5.3: This table shows the derived fitting parameters for describing sputtering yields of atomic and molecular ions with equation 5.1. The data in this table was published in [87].

The threshold energy E_{th} as well as q , μ and λ are fitting parameters. $s_n^{\text{KrC}}(\varepsilon)$ represents the nuclear stopping power calculated with the KrC screened interaction potential and has the following dependence on the reduced energy ε :

$$s_n^{\text{KrC}}(\varepsilon) = \frac{0.5 \ln(1 + 1.2288\varepsilon)}{\varepsilon + 0.1728\sqrt{\varepsilon} + 0.008\varepsilon^{0.1504}} \quad (5.2)$$

The reduced energy ε is defined as

$$\varepsilon = E \frac{M_2}{M_1 + M_2} \frac{a_{\text{L}}}{Z_1 Z_2 e^2} = E \varepsilon_{\text{L}} \quad (5.3)$$

for an ion with mass M_1 and atomic number Z_1 and a mono-elemental target with M_2 and Z_2 . Similarly, the Lindhard screening length a_{L} is

$$a_{\text{L}} = \left(\frac{9\pi^2}{128} \right)^{1/3} a_{\text{B}} \left(Z_1^{2/3} + Z_2^{2/3} \right)^{-1/2} \quad (5.4)$$

with the Bohr radius a_{B} . For composite targets that are of interest for space weathering and also for molecular ions, the restriction to specific projectile and target atomic properties is not completely applicable. For this reason, the proportionality factor ε_{L} in equation 5.3 describing the ratio ε/E was used as an additional fifth fitting parameter. In doing so, all simulated sputtering yields from SDTrimSP simulations could be fitted quite well indicated by the full lines in Figure 5.16. The resulting parameters for the fitting function are shown for the different projectiles in table 5.3.

	Yields used in [206] (atoms/ion)	Simulation (Phobos) (atoms/ion)	Scaling	Simulation (augite) (atoms/ion)	Scaling
1 keV H	<i>0.015</i>	0.015	1.0	0.013	0.888
4 keV He	<i>0.14</i>	0.092	0.657	0.087	0.624
Solar wind sputtering (H + He)	0.01852	0.01717	0.927	0.0154	0.832
16 keV O	<i>1.3</i>	0.642	0.494	0.605	0.465
Ratio of 16 keV O / solar wind sputtering	70.2	37.4	0.533	39.3	0.559

Tab. 5.4: This table shows sputtering yields from the different erosion contributions on Phobos. Values used by Nénon et al. in [206] are shown in the second column, where the explicitly stated values are shown in italics font. They are compared to SDTrimSP simulations with Phobos and augite concentrations. Scaling factors are given in respect to the yields from [206].
 This table was in part published in [87].

5.6 Conclusions for the Sputtering of Phobos

5.6.1 Sputtering by Planetary O ions

With the newly measured sputtering yields for the Phobos analog augite, more representative information on the erosion yields on Phobos have become available. The consequences of these new findings on the total space weathering of Phobos should be evaluated, especially in respect to the ratio of sputtering by O ions to sputtering by solar wind ions. Previous assumptions on neglecting molecular effects from O_2^+ ions and the sputtering by CO_2^+ ions are supported by the augite measurements shown in the previous sections. However, the absolute values of sputtering yields have to be corrected.

With the assumption of O implantation occurring, all relevant measured yields can be reproduced by SDTrimSP simulations. For He, this was shown in the work by Biber et al. [86] and for H, additional measurements were performed, finding a good agreement with SDTrimSP as well. For their work on the sputtering of Phobos

[206], Nénon et al. state that they used sputtering yields of 0.015 atoms/ion for 1 keV H, 0.14 atoms/ion for 4 keV He and 1.3 atoms/ion for 16 keV O ions. They base their inputs on Ni sputtering yields from [214] and use an energy dependence shown by Poppe and Curry [200]. SDTrimSP simulations using the estimated Phobos composition (table 5.1) as an input give the following values: 0.015 atoms/ion for 1 keV H, 0.092 atoms/ion for 4 keV He and 0.642 atoms/ion for 16 keV O ions. The comparison with previously used input parameters shows lower sputtering yields for He and O ions, as is summarized in table 5.4. With the He/H ratio measured by MAVEN for the ion fluxes on Phobos of 2.9% [206], the total kinetic sputtering by solar wind ions is calculated to 0.0172 atoms/ion. This is only by about 8% smaller than the respective value used by Nénon et al. of 0.0185 atoms/ion (calculated from the values given in [206]). For the sputtering by O ions, a more significant correction is necessary because the calculated sputtering yield of 0.642 by 16 keV O ions is 50.6% smaller than the previous sputtering input of 1.3. The used energy dependence depicted in [200] fits well to the SDTrimSP energy dependence and therefore all O sputtering yields can be rescaled by the same value. In total, the ratio of O sputtering to solar wind sputtering is predicted to be 46.7% or by factor of 1.88 lower than previously assumed (see table 5.4).

The above presented calculations were performed based on the experimental findings for augite, but simulations were done with the slightly different Phobos composition (table 5.1) as an input. This composition is of course not well constrained and it should therefore be tested, how sensitive the achieved results are on different composition inputs. For this reason, the ratio of O sputtering to solar wind sputtering was also calculated for the augite composition. The result of a similar reduction by 44.1% or a factor of 1.79 was found, which strongly indicates that the presented comparison of sputtering by O ions and sputtering by solar wind ions is quite robust. The individual results of the simulation steps are also included in table 5.4.

Ultimately, sputtering by O ions has been overestimated and Figure 5.17 shows the effect of the sputter yield rescaling based on the previously presented findings. Here the ratio of total sputtering by O ions and total sputtering by solar wind (SW) ions is plotted over the Mars-Solar-Orbital (MSO) longitude, representing one orbit of Phobos around Mars. Originally, this ratio was calculated by Nénon et al. and their results are shown as the black dotted line [206]. While solar wind sputtering is the dominant erosion process over most of the orbit, planetary O ions significantly dominate in the Martian magnetotail. This is a result from the emission direction of the planetary ions as well as shadowing of the solar wind [206]. The correction of

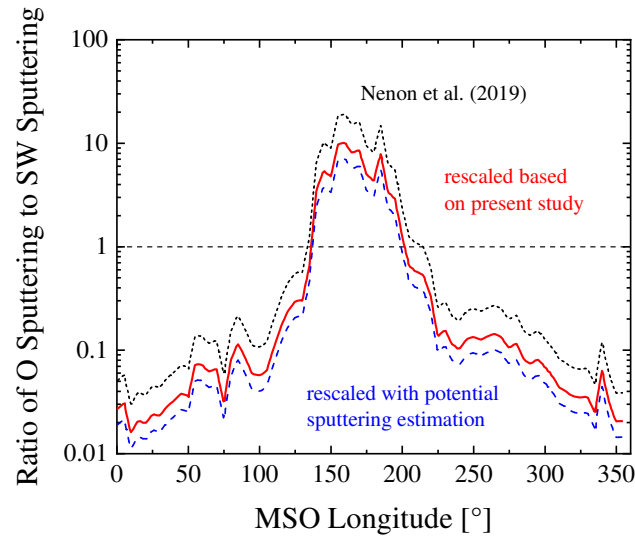


Fig. 5.17: The ratio of sputtering by O ions to sputtering by solar wind (SW) ions is here plotted over the longitude of a Phobos orbit around Mars. The original result from Nénon et al. is shown as the dotted black line. The rescaling based on experimental values for the sputtering by O ions is shown as the red line. An additional estimation for potential sputtering by He^{2+} ions is included as the dashed blue line (see section 5.6.2). While the total contribution of the planetary O decreases, it is still significantly dominant in the Martian tail region around an MSO longitude of 180° . This figure was published in [87].

this ratio based on the presented findings on the sputtering of Phobos is shown as the full red line. As described above, it is lower by a factor of 1.88, but this does not affect the general trend of planetary O ions sputtering up to a factor of 10 more than solar wind ions at MSO longitudes around 180°.

In total, planetary O ions can be calculated to contribute 13% of the total sputtering of the surface of Phobos, compared to about 23% based on previous assumptions. These numbers represent the sputtering averaged over the whole surface and does not take into account the tidal locking of Phobos. The Mars-facing side will be affected more by the sputtering due to the influx of planetary O ions as discussed by Nénon et al. [188]. Their analysis based on further spatially resolved MAVEN ion maps results in the estimation that 49% of sputtering on the Mars-facing hemisphere on Phobos is caused by planetary O ions, while the contribution on the other hemisphere is only 3%. Ultimately, space weathering is estimated to be accelerated by a factor of 2 due to the Martian ion precipitation on the Mars-facing side [188]. In combination with possible implantation effects, the space weathering history of the Mars-facing side of Phobos will be more interesting, which should be taken into account for future missions to the Martian moon such as the upcoming MMX lander [188].

5.6.2 Potential Sputtering by He²⁺ Ions

Another effect that will influence the ratio of sputtering by planetary O ions and solar wind ions is depicted in Figure 5.17. As discussed in the previous chapter, the sputtering by multiply charged solar wind ions will be a dynamic process that even causes an increase of the total sputtering in the steady state. Based on the wollastonite findings, this increase was calculated to be 43% based on a solar wind He concentration of 4%. Solar wind He ratios reported by MAVEN measurements are somewhat lower at about 3% and no extended potential sputtering experiments have been done for augite. Nevertheless, these results can be used as an approximation for the potential sputtering effects of the solar wind, as they are also consistent with other findings for different materials. For this reason, Figure 5.17 also includes the O/SW ratio with included potential sputtering as the blue line. It leads to a further decreased dominance of planetary O ions in the magnetotail and in total, O ions would then cause 10% to the total sputtering of Phobos. Adding potential sputtering does, however, not change the result that planetary O ions still significantly con-

tribute to the space weathering of the Mars-facing hemisphere of Phobos.

5.7 Conclusions and Outlook

Using thin films deposited from the Mg- and Fe-rich pyroxene augite as an analog for the surface of Phobos, sputtering yields under irradiation of O^+ , O_2^+ , C^+ and CO_2^+ were measured with the QCM technique. Supported by SDTrimSP simulations, a good agreement could be found as well as strong indications of ion implantation. Sputtering yields by planetary O ions were found to be smaller than previously assumed and no signs of molecular effects were observed for O_2^+ and CO_2^+ ions. With these better constrained sputtering yields, the total effect of the sputtering of Phobos by planetary ions could be reassessed and is found to be between 10 and 15%. However, due to the tidal locking of Phobos, the Mars-facing side will be more affected by this flux of planetary O ions [188], which should be taken into account for future exploration of the Martian moon.

From an experimental point of view, more detailed investigations of O ion implantation would be of great interest. Due to planetary minerals already containing a large amount of O, this requires a specially designed experimental procedure to separate implanted O from bulk O. For example, in-situ ERDA with the irradiation of ^{18}O would allow the quantification of implanted projectiles. Such experiments with O and other possibly escaping atmospheric ions would help in assessing the importance of ion implantation in the solar system. For moons close to their parent planets such as Phobos, one could find traces of the history of the planet's atmosphere buried within its regolith. Such investigations would be of great relevance for MMX or other future sample return missions. It will also play a role for other bodies in the solar system, such as Earth's Moon, where a similar scenario of an earth wind has been reported [215]. The resulting flux of O ions is the proposed driver for the formation of hematite Fe_2O_3 on the Moon [187]. Additionally, accelerated O ions are also assumed to play a role in the formation of specific components of Mercury's exosphere [216]. Heavy ions from the solar wind will also contribute to sputtering and the formation of amorphous rims on planetary bodies [149]. All these effects will require more experimental investigations to better understand the role that also ions beyond H and He play for space weathering.

Results: Retention and Release of Hydrogen Isotopes in Tungsten

The research on the application of in-situ IBA for investigating the retention of H isotopes in W described in this chapter was performed in the scope of the EURO-FUSION work package Plasma-Facing Components (WP PFC Subproject 3.1). All described experiments were performed in cooperation with the Uppsala University at the SIGMA chamber, which is described in section 3.1.1. Some parts of section 6.2 were compiled in a manuscript [217], but have not yet been published.

6.1 NRA of H-Implanted W Samples

The goal of the measurements presented in this section was to investigate H implantation in W film targets by combining TDS and NRA based on the ${}^1\text{H}({}^{15}\text{N}, \alpha\gamma){}^{12}\text{C}$ reaction. As described in section 3.1.3, its sharp resonance with a width of 1.8 keV allows profiling of the ${}^1\text{H}$ content of a sample with precise depth resolution. For a W target, the stopping of ${}^{15}\text{N}$ with an energy of 6.385 MeV, where the nuclear reaction with H atoms is triggered, is given by SRIM as 4.1 keV/nm. Taking into account Doppler broadening and detector properties, a depth resolution in the low nm range can be achieved [66]. However, measuring the whole H inventory in the sample over an extended depth range requires irradiation with several different energies of the ${}^{15}\text{N}$ primary beam. Additionally, the γ detector at the used setup has to be placed outside of the vacuum chamber and thus its solid angle is limited. Therefore, the sample is subjected to a higher fluence of MeV ions than it is otherwise usual for IBA. This factor was observed to significantly influence how a W film sample behaves under H implantation and subsequent annealing, which is discussed in the following.

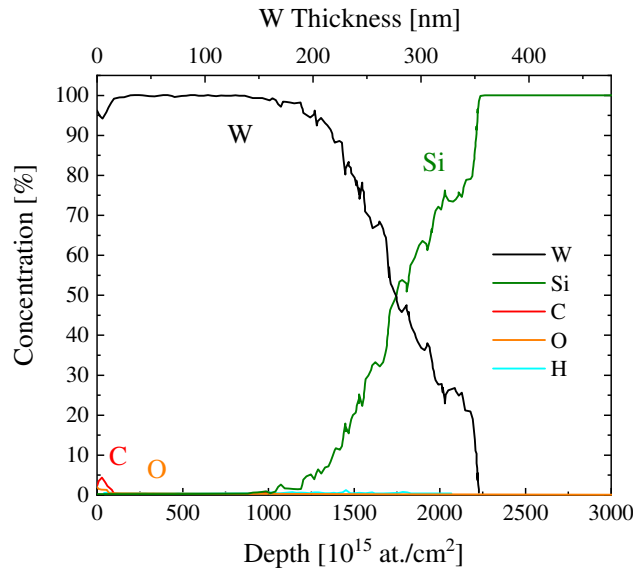


Fig. 6.1: This plot shows the ToF-ERDA analysis of the thin W films used for investigating H retention in W with ¹⁵N NRA. The W film (black) is clearly visible with a high purity on top of the Si substrate (green). Significant contamination is only found in the form of a C- and O-containing layer with a thickness of about 10 nm on top of the sample.

6.1.1 Sample Preparation and Analysis

For the in-situ measurements of H depth-profiling with ¹⁵N NRA and outgassing at Uppsala University, thin W films were used. These films were sputter-deposited on Si wafer pieces at IPP in Garching. ToF-ERDA measurements at Uppsala University showed a film composition of close to 100% W apart from a contaminated surface layer with a thickness of about 10 nm (see Figure 6.1). The total thickness of the W layer was found to be 245 nm from RBS measurements (see Figure 3.17 in section 3.1.5), which allows more precise thickness determination than ToF-ERDA. The surface roughness was investigated with an AFM by Christian Cupak at IAP, finding a negligible RMS roughness value of 2.4 nm.

6.1.2 Experimental Procedure

After insertion into the SIGMA chamber, the W film sample was cleaned by 5 keV Ar irradiation at an angle of incidence of 50° for 10 minutes to remove any surface contamination. The effect of the cleaning was checked with in-situ RBS analysis in the SIGMA chamber. Subsequently, first ¹⁵N NRA experiments were performed,

using energies around 6.4 MeV and $^{15}\text{N}^{2+}$ ions. Calibration measurements of the detector solid angle were done with a Si sample with a pre-defined H concentration of 18.5% and background gamma signals were regularly recorded throughout the whole experimental procedure. A first analysis of the W film sample was done before any H irradiations and no H in the W sample was observed apart from a water adsorption peak at the surface.

The W film was then irradiated with H ions at 5 keV in two steps to a total fluence of 5.3×10^{22} H/m², assuming a $\text{H}^+:\text{H}_2^+$ ratio of 7:93 corresponding to the reported fraction of dissociation during electron impact ionization of H₂ [218]. After H implantation, a TDS measurement was performed up to a temperature of about 330°C. H profiles were monitored with ^{15}N NRA between the implantation steps, after the full implantation as well as during and after the sample heating process. Profiles were recorded by varying the energy of the primary ^{15}N beam and the probed depth can be calculated with the stopping of ^{15}N in W of 4.1 keV/nm as calculated with SRIM. Typical measurement times for each spot were between 10 to 20 minutes at ion beam currents of about 2 nA.

6.1.3 Results

H Profiles

Figure 6.2 gives an overview of the NRA results after both the implantation (blue) and the subsequent heating (red). The recorded H profiles are compared to the H ion range distribution (green), corresponding to a ratio of molecular and atomic ions of 93:7. At an acceleration voltage of 5 kV, the molecular H_2^+ ions will have an energy of 2.5 keV/H and therefore have a lower implantation depth than the 5 keV atomic H^+ ions. After the irradiation with 5.3×10^{22} H/m², the H content of the sample is clearly visible. Near the surface, a H concentration between 10 and 15% is observed, while deeper layers mostly contain around 5%. H is also found deeper than the expected ion ranges from SDTrimSP, which shows the diffusion of H after being implanted. Measurements near the interface between W film and Si substrate indicate less H in the W film there, but an increased H content at the W-Si interface. Due to low count rates, the experimental error bars are however too large to assess this with certainty.

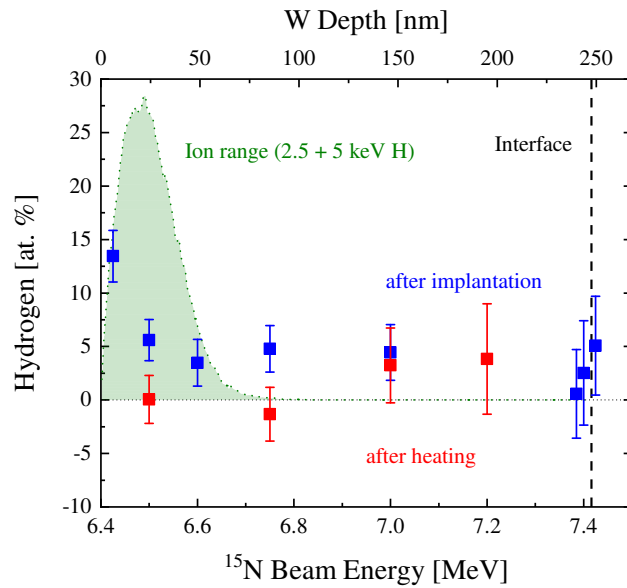


Fig. 6.2: This plot shows the measured NRA H profiles after the H irradiation with 5.3×10^{22} H/m² (blue). The green area represents the range distribution of H ions from SDTrimSP, accounting for both atomic and molecular contributions. H concentrations of a few % are found across the whole implantation range and even in deeper layers. After heating up the sample, H in the near-surface region is depleted (red), while the H content deeper in the sample is less affected.

After heating the sample up to about 330°C, it becomes depleted of H at depths between 0 and 100 nm. However at around 150 nm and deeper, there are still H concentrations of about 5% measured, even though again low counting rates result in large error bars. Nevertheless, the results strongly indicate that H closer to the surface is affected differently by the heating than H in deeper layers.

Blister Formation

After the experiments, clear optical changes of the irradiated parts of the sample surface could be observed, as it is shown in Figure 6.3. The area that was not covered by the sample holder shows a significant darkening following the H implantation. Additionally, a black spot can be seen where the ¹⁵N ion beam hit the sample during the NRA measurements. The latter effect is, however, a common occurrence for IBA in high vacuum due to deposition of carbon from adsorbed carbohydrate molecules (from pump oil) cracked by the ion beam.

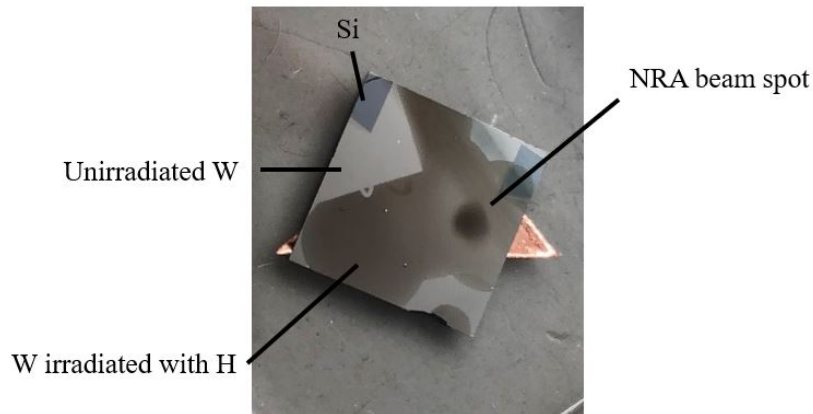


Fig. 6.3: This photo of the W sample after irradiation shows strong changes in its optical properties. Both the area that was affected by H implantation as well as the beam spot of the ^{15}N ion beam are darkened compared to the unirradiated area.

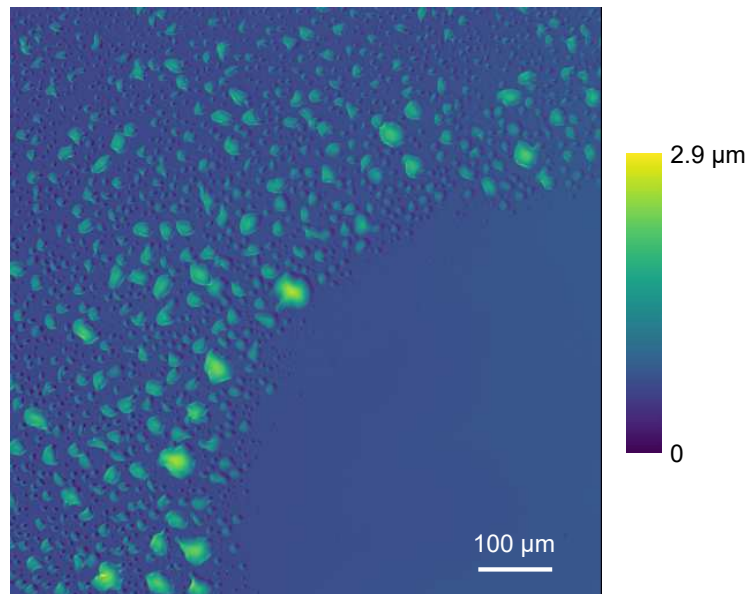


Fig. 6.4: This confocal microscopy image shows the edge of the NRA beam spot. The change from a blister-covered morphology to a smoother surface, where the sample was irradiated with the ^{15}N ion beam (lower right), is clearly visible.

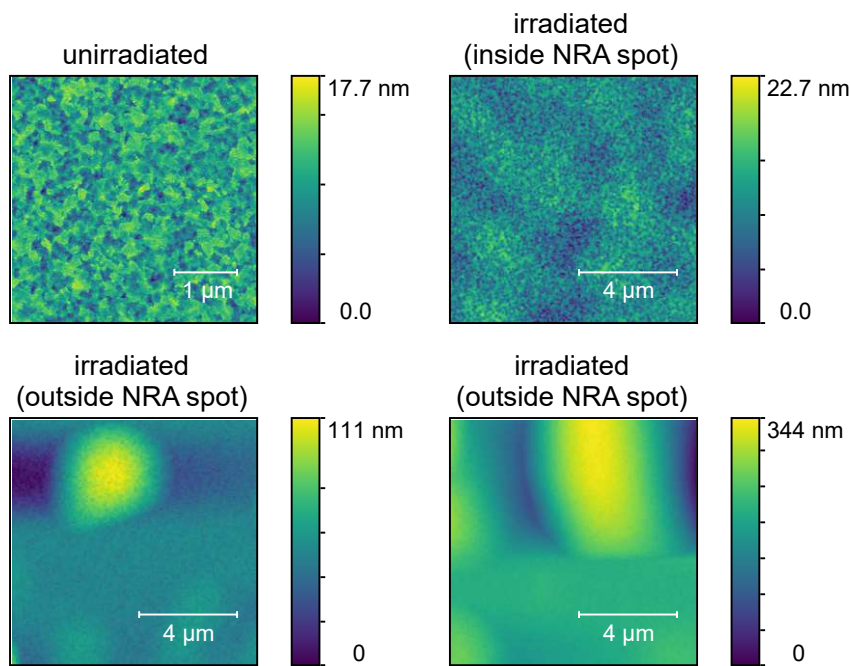


Fig. 6.5: A compilation of AFM images of the W film sample after the experiments. The color bars next to the picture denote the height scales of the respective sample morphology.

Upper left: The surface of the unirradiated sample. Upper right: On the spot where the NRA beam hit the sample, no blister formation can be observed. Instead the surface looks similar to unirradiated W. Lower images: Examples of formed blister structures on a H-irradiated area.

Further differences in the surface properties become visible, when the sample is investigated under the confocal microscope. Figure 6.4 shows a picture from the edge of the ^{15}N ion beam spot, which can be clearly distinguished from the rest of the sample by its surface morphology. In the ^{15}N beam spot in the lower right part of the image, a smooth surface is visible, while the surface of the irradiated area outside of the beam spot is dominated by blisters. Blister diameters range up to several $10\ \mu\text{m}$ and heights of several $100\ \text{nm}$ to a few μm can be observed. This increased roughness of the H-irradiated area of the sample by blister formation that is clearly visible in the confocal microscopy image, explains the darkening of the sample that is visible in Figure 6.3.

The irradiated surface was also investigated with AFM measurements with examples being compiled in Figure 6.5. The upper left image shows the smooth unirradiated W surface, which has an RMS roughness value of $2.4\ \text{nm}$ and a granular morphology. The surface of the NRA beam spot after irradiation (upper right image) shows a similar morphology with a very close RMS roughness of $2.5\ \text{nm}$. During the AFM analysis,

a second smooth spot without any blisters was found. This spot could be connected to the ToF-ERDA analysis of the sample before the H irradiations. ToF-ERDA uses energetic I ions for the analysis, which can be expected to have a similar effect as the ^{15}N NRA ions. The sample was investigated with ToF-ERDA once more after the whole campaign, but this did not lead to the removal of any previously formed blisters. Outside of these spots, the blisters cover the whole sample and smaller examples could be imaged in the AFM as is shown in the lower images in Figure 6.5. On a small scale, the surface on the blisters show similar granular morphology as observed for the unirradiated areas. This could be confirmed by an additional analysis of the top of a blister: After subtracting a polynomial background of second order, an RMS value of 2.1 nm could be determined for the surface, which is again close to the value for the unirradiated sample. Overall, this indicates that larger volumes of the W are moved by the blister formation during H irradiation and that this effect does not happen directly beneath the surface. Additionally, the significant differences in surface morphology observed in the microscopy investigations make it evident that IBA methods such as NRA and ToF-ERDA significantly alter how the W film sample is affected by H bombardment.

6.1.4 Discussion

H Retention and Depth Profiles

The implantation and retention of H isotopes together with depth profiling has been extensively investigated before (e.g. [219, 220, 221]). However, there exist many parameters during these investigations that vary between experiments. Most importantly, experiments with plasma devices and ion beam experiments have to be distinguished. Plasma devices apply high ion fluences (10^{28} / m^2 have been achieved [222]) at low energies (often only several 10 eVs). In contrast, ion beam experiments apply smaller fluences, but operate under more controlled conditions and at higher energies, where ion-induced damages play an important role.

In undamaged W, the H solubility is very limited [223], while diffusion activation energies are also low [224]. Implanted H will therefore be very mobile leading to low H concentrations in W. In a fusion reactor, this situation will change when high energy D ions, seeding gas ions or 14.1 MeV neutrons will create damage in the reactor's wall material. These damages can act as traps where H is collected and higher activation energies hinder the diffusion [223]. Therefore, higher H

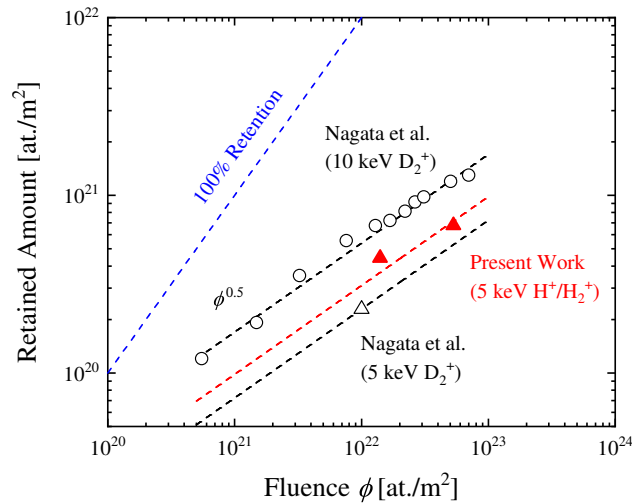


Fig. 6.6: The H content retained in the W film sample, determined by linear interpolation of NRA measurements, is compared to data for D irradiations at 2.5 (open triangle) and 5 keV/D (open circles) [225]. Fits proportional to the square root of the fluence ϕ are also included as the dashed lines. The obtained amount of retained H is consistent with these results from Nagata et al.

concentrations can be expected in damaged layers of W as well as an increase of the H retention.

The total amount of retained H in the above presented measurements was obtained by linearly interpolating the H concentrations from NRA. NRA profiles were recorded at two different fluences and the results are shown in Figure 6.6. After the highest applied fluence of 5.3×10^{22} H/m², a H content of 6.8×10^{20} H/m² was obtained, which represents 1.3% of the incident fluence. D retention under circumstances where ion-induced damages play a role have, for example, been investigated at similar energies and fluences by Nagata et al. [225]. Figure 6.6 compares the total amount of retained D from those investigations at different energies (open black symbols) to the H content determined from NRA measurements, plotted over fluence ϕ . The dashed lines represent fits to the datasets that are proportional to $\sqrt{\phi}$, which show that the H retention from NRA is in principle consistent with previous results. When it is taken into account that most of the ions are assumed to be 5 keV H₂⁺ and H will be less effective at creating damages in W than D, the measured H concentrations are even higher than it would be expected by the data from Nagata et al. [225].

Due to the connection between H retention and damage formation, the depth profile of implanted H after the full fluence of 5.3×10^{22} H/m² (blue) is compared to

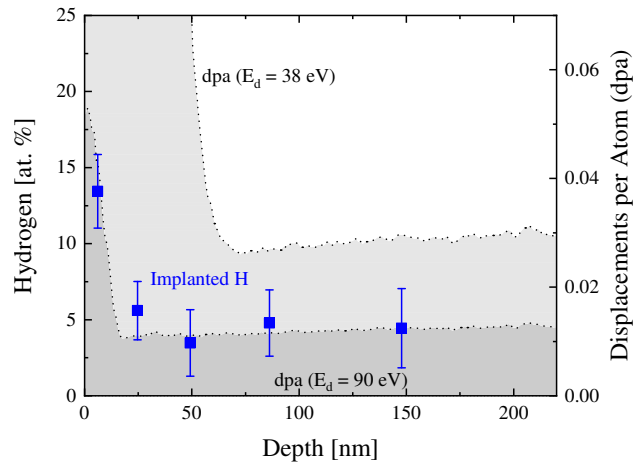


Fig. 6.7: The H profile measured after implantation (blue) is compared to SDTrimSP simulations of the damages created by both H and ^{15}N ions with two different W displacement energies E_d of 38 and 90 eV. The H profile fits well to the damage profile calculated for the recommended value of $E_d = 90$ eV.

simulated damage profiles from SDTrimSP (black dashed lines) in Figure 6.7. For the simulation of the ion-induced damages both due to the H bombardment and the ^{15}N beam from NRA analysis, two different W displacement energies E_d were used: The standard value for E_d of W in SDTrimSP is 38 eV, which is close to the reported minimum displacement energy of a W atom [226]. The generally recommended displacement energy value is, however, much higher at the average displacement energy of 90 eV (see for example [227]). This average energy, which is necessary to remove a W atom from its lattice position, has been used regularly for calculating displacements per atom (dpa) in W and was found to agree well with molecular dynamics simulations [228]. Figure 6.7 shows calculated dpa values for both 38 eV and 90 eV to illustrate the significance of the choice of E_d for the dpa calculation. The value of E_d strongly affects the number of displacements especially close to the surface, where most of the interactions between incoming H projectiles and W take place. Due to the large mass differences between H projectiles and W target atoms, the maximum energy transfer during an elastic collision is about 2% of the H's energy, which is calculated from the energy transfer factor $\gamma = 4 \cdot m_{\text{H}} \cdot m_{\text{W}} / (m_{\text{H}} + m_{\text{W}})^2$. As a result, 2.5 and 5 keV H ions can only transfer 54 and 108 eV to a W atom. For the choice of E_d of 90 eV, therefore only the 5 keV H will be able to cause displacements. The 2.5 keV H from the dominant H_2 part of the beam will not contribute to creating damages in this case. This varying behavior explains the vast differences for the two simulations up to the H range of about 60 nm. In the deeper layers, the damages are then only caused by the ^{15}N beam, which contributes between 0.01 and 0.03

dpa for the applied fluence, which is almost constant across the whole film.

When comparing both damage profiles to the measured H concentrations at different depths, they are much better reflected by the simulation with the recommended E_d value of 90 eV. High H concentrations between 10 and 15%, a value that also agrees with findings by Nagata et al. [225], are only found near the surface. For depths of 25 nm and larger, mostly constant H concentrations of about 5% are found. This profile is consistent with the constant damage profile from the ^{15}N ion beam from SDTrimSP. Density Functional Theory (DFT) calculations have shown that up to five H atoms can be trapped in one W vacancy [229], which would correspond to the 0.01 dpa from the 90 eV simulation to store 5% H. This comparison also shows that the ^{15}N ion beam has a significant influence on the retention of H because it creates a large number of additional defects. As discussed previously, the retained H is somewhat high when compared to D retention from Nagata et al. [225]. This will be dependent on the type of W sample used, but the observed tendency for the experiments presented here could also be caused by H being trapped in the displacements created during the prolonged ^{15}N NRA measurements. Focusing on the effects of neutron-induced damages mimicked by W self-implantation, an increasing H retention for increasing damages in the sample has been observed in multiple studies [230, 231]. The presented study provides further indication, how increased H concentrations are connected to displacements caused by MeV ions. Additionally, the method of ^{15}N NRA should be treated with caution for the investigation of H retention, especially when low count rates require longer measurement times already before irradiations.

Where the damage profiles shown in Figure 6.7 do not give an evident explanation, is the H profile shown in Figure 6.2 that was measured after heating the sample to 330°C while continuously recording NRA signals. There at 25 and 75 nm, a depletion of H was observed, while the concentrations in deeper layers were still around 5%. The continuous exposure to the ^{15}N beam will cause the creation of additional defects, while others might be annealed due to the increased temperature. The total ^{15}N ion beam fluence was 2.5 times higher than directly after the H implantation, which corresponds to the case shown in Figure 6.7. For $E_d = 90$ eV this would then lead to 0.03 dpa from the ^{15}N ion beam when annealing of defects is neglected. This effect alone is too low to sufficiently explain the depletion of H due to the formation of vacancy loops that would allow easier diffusion. The region where H is depleted does, however, roughly correspond to the region where 2.5 keV H ions will deposit their kinetic energy. The simulation with 90 eV will probably

only represent a lower limit for dpa creation because in some directions, W will be able to be displaced by those H ions. This increased defect formation by 2.5 keV H might give the needed explanation for the formation of vacancy loops. However, more experimental or numerical efforts are needed to understand this, especially because later measurements on D retention in W show a different behavior where no preferential depletion of near-surface regions occurs (see section 6.2).

Absence of Blisters in the ^{15}N NRA Beam Spot

Microscopy investigations of the W thin film after the experiments have revealed another obvious effect of the ^{15}N beam: the whole sample is covered with blisters apart from the spot where the ^{15}N ion beam hit the sample and the spot where probably ToF-ERDA analysis with I ions was performed. Instead of a blister-covered surface, a smooth morphology is found at these spots. The spot of ToF-ERDA analysis after H implantation did not affect the surface and it is also of interest to investigate if the ^{15}N NRA beam removed blisters or if their formation was suppressed. The first case would most likely represent an experimental artifact due to the prolonged irradiation with ^{15}N . However, the second case of blister suppression, probably due to additionally induced defects, could give insights into H retention in redeposited W layers that have been damaged by the continuous neutron flux of a nuclear fusion reactor.

Blister formation due to the collection of large amounts of H gas is a well-known phenomenon in plasma-wall interaction studies [232]. For example, Balden et al. have shown how blister formation can be connected to elastic deformation of the material, when pockets of initially mobile H gas are formed in cracks or grain boundaries [233]. For the present case of a W film on a Si substrate, the interface between the two sections represents the most evident natural defect where the collection of H might take place. A similar blistering due to D implantation in a W layer interface has, for example, been observed by Xu et al., who investigated D implantation in a 10 nm W film deposited on steel [234]. The fact that blisters are still visible after prolonged heating of the sample to 330°C, suggests a stable binding site for H gas. It is questionable if the additional energy that is provided by the NRA beam is enough to thermally remove H from the blisters. As discussed before, the induced damages by the NRA beam are also too low to provide an easier escape channel for implanted H through connected defects. Instead, it is more likely that the formation of blisters filled with H gas is already suppressed due to the

NRA measurement before H implantation. This would also fit with the observation for the ToF-ERDA spots, where suppression of blister from the analysis before the experiments was found, but no removal of blisters after the H implantation.

How H atoms reach the interface is very different depending on whether the H irradiation takes place inside or outside the ^{15}N beam spot. This is illustrated in Figure 6.8, where the dpa induced by H and ^{15}N are again plotted for the two displacement energies E_d of 38 (blue) and 90 eV (red). Two scenarios are compared: The upper image shows the calculated dpa from SDTrimSP for irradiation outside of the NRA beam spot. Here, damages are only created by the H irradiation. As a comparison, the lower image shows the dpa calculation inside the NRA beam spot, where the ^{15}N ions are responsible for additional displacements. The shaded areas represent the dpa caused by the NRA beam, which make up a large amount of the total damages especially further in the bulk of the sample. The black dashed line in both images in Figure 6.8 shows the distribution of ion ranges for the assumed 93:7 ratio of H_2^+ and H^+ . It can clearly be seen that especially for higher displacement energies, a significant amount of H will be initially implanted in a depth where no H-induced damages are created. Outside of the NRA beam spot, this H will be able to diffuse freely and also reach the interface. However, inside the NRA beam spot, the whole film is damaged by the dpa from the NRA beam representing additional trapping sites for H atoms. Using $E_d = 90$ eV, a total number of NRA-beam-induced vacancies $1.9 \times 10^{20} / \text{m}^2$ is formed by the NRA measurements before the D implantation and in-between implantation steps. As previously discussed, DFT calculations predict the possibility of up to five H atoms trapped in a single vacancy, which would give space for $9.5 \times 10^{20} \text{ H}/\text{m}^2$. From the measured NRA profiles, a total H retention of $6.8 \times 10^{20} \text{ H}/\text{m}^2$ could be deduced and thus a lower value than the maximum possible trapped H atoms in NRA-induced defects. The measured amount of retained H is similar to data from Nagata et al. and the observed order of magnitude for retention of H isotopes is further supported by the work of Haasz et al. [235] and Ogorodnikova et al. [51]. For fluences of around $5 \times 10^{22} \text{ D}/\text{m}^2$ at energies up to the low keV range, they report D amounts in the medium 10^{20} m^2 range as well.

Therefore, it is very plausible that the vacancies, which were induced by the ^{15}N ions from the NRA beam, trap a large part of the H before it can diffuse into the interface between W and Si. Outside of the NRA beam spot, the implanted H atoms are more mobile and diffuse until being trapped in the interface, where they form the observed gas bubbles. These experiments show once more how defects influence the behavior of H in a reactor wall material and similar cases as observed here will

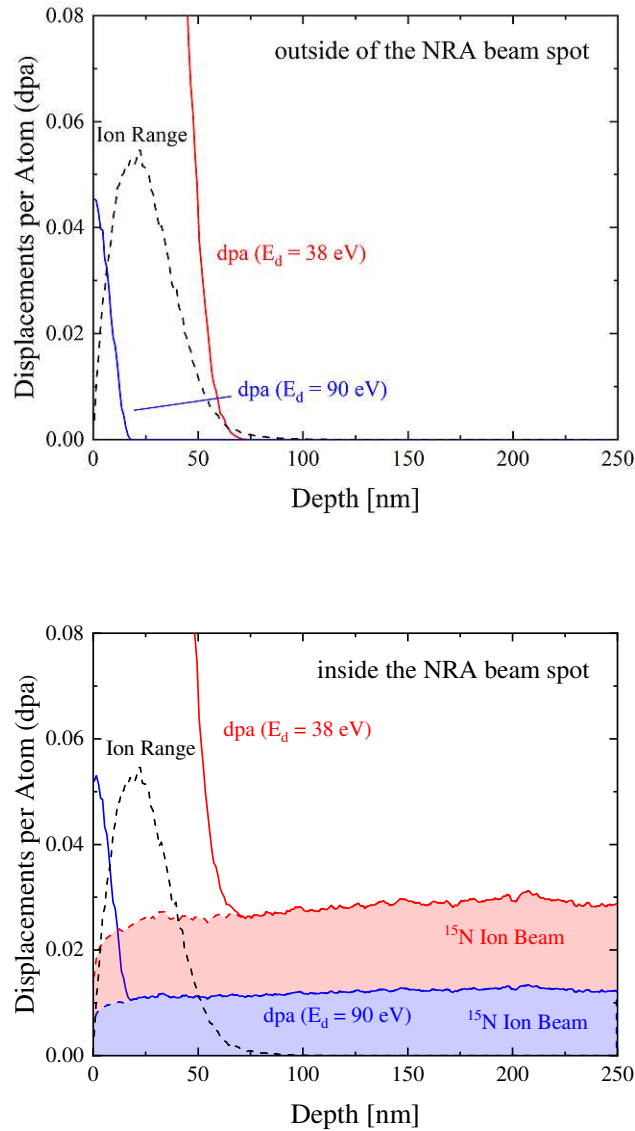


Fig. 6.8: These plots give an overview of the damage profiles that were calculated for the W samples as well as the ion range (dashed black line) from SDTrimSP based on the H and ¹⁵N fluences from the experiments. Two different displacement energies E_d were considered: 38 eV (red) and 90 eV (blue).

Upper image: Outside of the NRA spot, only displacements by the H ion bombardment are induced. For the commonly used displacement energy of 90 eV, a significant amount of H is implanted in regions where no damages are created. These H atoms will be able to diffuse freely.

Lower image: Inside the NRA spot, the ¹⁵N ions cause a significant additional contribution to the damages of the W sample, especially in depths beyond the H ion ranges. The calculated dpa from the ¹⁵N ions are signified by the dashed lines and the shaded area. Diffusion into deeper layers and to the W-Si interface is significantly hindered by the additional displacements.

also be relevant for additional defects caused by neutron irradiation.

6.1.5 Conclusions

From the discussions presented above, ^{15}N NRA investigations for profiling H concentrations in W evidently have to be treated with caution. This method provides unrivaled depth resolution compared to other IBA techniques, but this comes with several drawbacks. A large number of measurements (i.e. a high fluence) are necessary to profile a wider depth interval and the low gamma count rates also make a significant fluence of ^{15}N ions necessary. For subsequent H implantation, the displacements caused by these ions could be connected to differences in the amount of retained H and especially where the H is stored. As the NRA beam spot is completely free of any blistering, ^{15}N NRA cannot be regarded as a non-invasive method in this case. Instead, IBA methods with lower energies, lighter projectiles and lower fluence requirements should be favored especially for pre-characterization of the used samples.

These investigations of course also give further insights into effects that will play a role for neutron radiation. The 14.1 MeV neutrons that are products in a D-T fusion reaction will introduce additional defects into the wall materials, which will also affect H isotope retention. These effects have been investigated mostly with self-irradiation of MeV W ions [230]. The experiments presented in this thesis also show that in cases of extreme neutron doses, H isotopes might be completely prevented from diffusing deeper into the sample. This will lead to higher retention in more stable trapping sites, but closer to the surface they might be reintroduced into the plasma more easily as the wall material is eroded. Damages induced by neutron irradiation will definitely also play a role for the H retention in redeposited W layers. These layers will be formed during prolonged plasma irradiation leading to the growth of layers from atoms that were previously sputtered at another location. The interfaces between these W layers and the respective underlying materials can be expected to trap large amounts of H isotopes. For example, Xu et al. investigated such a case and observed significant blistering and W exfoliation [234], which would be an undesired effect for efficient reactor operation. However, if neutron-induced damages in the redeposited W layer trap H atoms and reduce or even prevent the formation of blisters at the interface, these negative effects could be mitigated based on the above presented observations. As the measurement of the H retention in redeposited W layers is a part of upcoming EUROFUSION research projects, the role of

neutron-induced damages should definitely be kept in mind and further investigated.

6.2 ERDA and TDS of D-implanted W Samples

Following the conclusions from the experiments of ^{15}N NRA presented in the previous section, several challenges have been found for in-situ IBA investigations of H retention. Most importantly, introducing new damages into the sample affects how H is implanted and should therefore be minimized. What was additionally not discussed in detail before, the fixed probing depth of ^{15}N NRA represents a disadvantage for investigating a sample during a heating process because only a very limited depth range of the sample can be observed continuously. It would instead be preferable to measure the H content at an extended depth range without the need of changing primary ion beam energy.

For this reason, further in-situ IBA measurements were performed by using ERDA with a 3.4 MeV He primary beam. He ions at this energy introduce fewer displacements than ^{15}N by about a factor of 300 according to SDTrimSP simulations ($E_d = 90$ eV). By energy-resolved measurement of the recoils, profiles of H and D up to depths of 350 nm can be continuously recorded at the same time with a depth resolution of about 40 nm. The studies presented in the following sections show, how this method can be applied to monitor the retention and outgassing of different H contributions in a W foil sample during the heating process of a TDS measurement.

6.2.1 Sample Preparation and Analysis

For the ERDA measurements, bulk targets were chosen to avoid any interface effects as observed for the thin film targets. The used bulk foils with a thickness of 0.5 mm were acquired from MaTeCK GmbH. The larger piece was cut into multiple smaller pieces of an area of about 10×10 mm² for individual irradiations. Before inserting into vacuum, all samples were cleaned with distilled water and isopropyl alcohol in an ultrasonic bath. The samples were analyzed with ToF-ERDA with a 36 MeV I^{8+} beam at Uppsala University, showing the purity of the sample to be better than

99% in accordance to the nominal purity of 99.9%. AFM measurements by Christian Cupak at IAP showed an RMS roughness of 7 nm, indicating a mostly flat sample.

6.2.2 Experimental Procedure

W foil samples were irradiated with D ions under an incidence angle of 4° at room temperature, using an acceleration voltage of 3 kV. Assuming again the ratio of 7% atomic D^+ ions and 93% molecular D_2^+ ions, irradiation fluences between 10^{21} and 10^{22} D/m² were achieved. After implantation, the samples were heated up to 1400 K, as checked with an optical pyrometer, using both step-wise and continuous heating ramps. Outgassing of D_2 was recorded with the RGA in parallel. ERDA measurements were not possible during the implantation, but before and during the sample heating, the D content in the sample was continuously monitored by probing the sample with the 3.4 MeV He^{2+} beam under 70° . ERDA with a 12.9 μm Al absorber foil in front of the PIPS detector was recorded at the same time as PIXE with a 204 μm mylar absorber foil in front of the SDD detector. PIXE was here mainly used for ion beam current normalization.

6.2.3 Results

A typically observed ERDA profile after implantation of 1.34×10^{22} D/m² is shown in Figure 6.9 as the black line. Contributions from both D and H are visible. The H signal can be attributed to water adsorption on the surface as well as H from residual water in the ion source being implanted in the sample as well. The red line in Figure 6.9 represents the result of a SimNRA simulation of the spectrum [133], which shows that the D signal can be separated into a near-surface component (region A, blue, signal from D in depths up to 45 nm according to SimNRA) and a bulk component (region B, green). Depth scales for both the D and H signals are included in Figure 6.9, but it has to be kept in mind that the depth resolution of the measured spectra are limited due to straggling effects [10]. This broadening of the energy distribution of primary ions in the sample as well as recoils in the sample and the absorber foil ultimately restricts the depth resolution of the ERDA measurements. For the above shown example, 4.5×10^{20} D/m² are retained in region A, which corresponds to an average concentration of 12.5% in the W sample, and 1.6×10^{20} D/m² are retained in region B (0.9%). Within the information depth of about 350

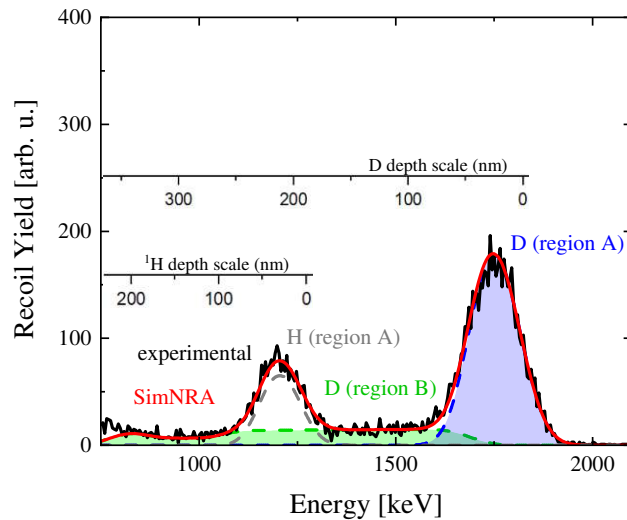


Fig. 6.9: This plot shows D and H signals from an ERDA measurement after implantation of 1.34×10^{22} D/m². The black line represents the measured data, the red line gives a simulated spectrum from SimNRA [133]. The included depth scales show that a large amount of D is concentrated near the surface in the interaction region of the incident ions (region A, blue). In the bulk of the sample, the D concentration is much lower (region B, green).

nm, 74% of the measured D content is found in region A within the top 45 nm of the sample. In total, a retention of 6.1×10^{20} D/m² or 4.5% of the irradiation fluence of 1.34×10^{22} D/m² is observed.

After implantation, the sample was heated up to about 1400 K and Figure 6.10 presents ERDA and TDS results from the same sample as shown in Figure 6.9. Blue dots and green triangles represent the development of the normalized D content from ERDA in region A and region B over time. The temperature was steadily increased from room temperature to 1400 K in a step-wise manner as it is shown in the inset in Figure 6.10. Bulk D in region B is found to already significantly decrease when a temperature of about 500 K is reached, while D close to the surface in region A stays mostly unchanged until a temperature of 650 K. Bulk D is much quicker depleted, while D from region A shows a steady decrease for increasing temperatures. At the end of the heating ramp, all D is removed from the sample. D₂ outgassing was also monitored with the RGA and from the measured signal, a remaining D inventory can be calculated, which is included in Figure 6.10 as the red line. It clearly follows a similar behavior as the D in region A closer to the surface and no further outgassing was measured with the RGA after the D in region A had been depleted. Due to different energy regions, where the respective recoils are

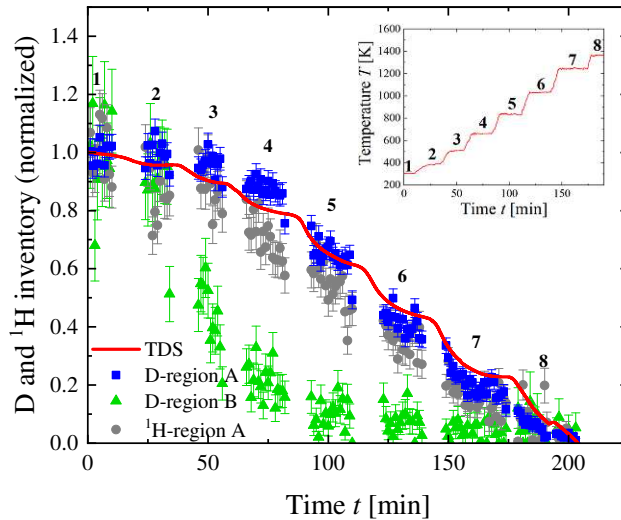


Fig. 6.10: During a step-wise heating ramp up to 1400 K, the D content in region A (blue) and region B (green) were measured with ERDA. At the same time, the outgassing of D_2 was measured with the RGA (red), which also allows calculating the remaining D inventory. Results from the TDS mostly follow the same behavior as the D stored in region A close to the surface.

recorded, the development of the H signal could also be measured at the same time, which is represented by the gray points in Figure 6.10. As the sample is heated up, the H content also decreases in the same manner as the D content in region A and is completely removed from the sample, when 1400 K are reached.

6.2.4 Discussion

D retention after implantation of 1.34×10^{22} D/m² was investigated with ERDA and significantly more D was observed in regions closer to the surface than deeper in the bulk. As already discussed above, the retention of D in W will strongly be connected to the damages of the sample. To investigate this relation for the present case of D retention in a W bulk target, SDTrimSP simulations were again performed with the W displacement energies E_d of 38 eV and 90 eV. Results of the simulated dpa are presented in Figure 6.11, together with the ion range of 3 keV D^+/D_2^+ and the separation into regions A and B. Damages induced by the 3.4 MeV He beam before D implantation were calculated to be lower by more than two orders of magnitude than the damages induced by D ions and are therefore neglected for this calculation. Evidently the separation of the retained D content into regions A and B allows some distinguishing between different types of binding sites. Both

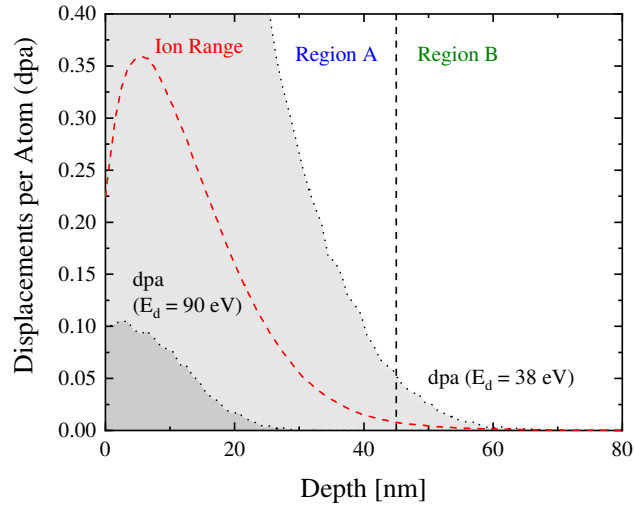


Fig. 6.11: As illustrated by SDTrimSP simulations of ion ranges and ion-induced displacements with $E_d = 38$ eV and $E_d = 90$ eV based on the experimental fluence of D irradiation, direct interactions between D projectiles and the W target atoms overwhelmingly take place in region A within the top 45 nm of the surface. D measured in Region B will reach its place via diffusion and subsequent placement in interstitial positions or trapping in pre-existing defects.

the ion range and the displacement of W atoms in the sample is overwhelmingly restricted to the top 45 nm of region A. D observed in region B will not be directly implanted there, but instead reach its place by diffusion. In region B, D atoms will then be retained in interstitial positions or in pre-existing defects such as grain boundaries.

The SDTrimSP simulation for $E_d = 90$ eV shown in Figure 6.11 gives a total number of 9.1×10^{19} vacancies/m² as a lower limit for ion-beam-induced damages. Assuming again that up to five D atoms trapped in each vacancy are possible, this would allow 4.6×10^{20} D/m² to be trapped in the ion-induced vacancies. This value agrees very well with the amount of D that was measured in region A with ERDA of 4.5×10^{20} D/m². This observation is also consistent with the ratio of retained H and calculated dpa for the W film discussed in section 6.1. There a H concentration of about 5% was measured in regions where the simulation with $E_d = 90$ eV predicts 0.01 dpa. The total observed D retention, which is 4.5% of the nominal irradiation fluence, furthermore coincides with literature data for similar energies and fluences that report D retention of a few percent as well (e.g. [225, 236, 237]).

The different binding of D atoms in region A and region B is also reflected in the ERDA measurements during the annealing of the sample. This can also be seen in

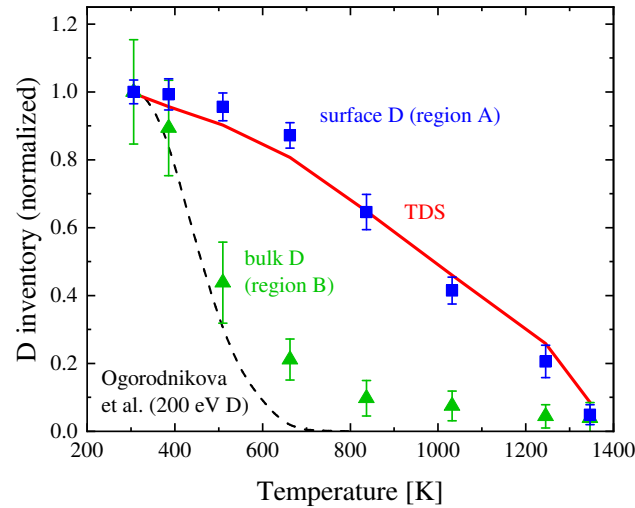


Fig. 6.12: This figure plots the experimental data for the parallel ERDA and TDS measurements from Figure 6.10 after a fluence of 1.34×10^{22} D/m² over the sample temperature. ERDA results for D are shown in blue for region A close to the surface and in green for region B in the bulk, while the red line represents the average for one step in the heating ramp. As a comparison with existing investigations, the TDS spectrum after a 200 eV D irradiation at a fluence of 10^{22} D/m² from Ogorodnikova et al. is included as the black dashed line [51]. At these energies no ion-induced displacements will be created in W and the D behavior over temperature agrees well with ERDA measurements in the undamaged bulk (green).

Figure 6.12, which shows the experimental data of the ERDA and TDS measurements averaged for each step of the heating ramp and plotted over temperature. The D from region B is depleted much quicker, which agrees with these D atoms being bound in less stable positions. Figure 6.12 shows a significant D decrease between steps 2 and 3, corresponding to a D release between 400 and 500 K. At temperatures above around 650 K, the D in region B is mostly depleted. This desorption of atoms that are not trapped in ion-induced defect is consistent with previous experiments and TDS results for a D irradiation at 200 eV from Ogorodnikova et al. are also plotted in Figure 6.12 (black dashed line) [51]. At 200 eV, the energy of the D ions is too low to cause W displacement and this data can therefore be compared to the decrease of D in the undamaged region B. Ogorodnikova et al. similarly observed a low-temperature desorption peak at around 450 K that could be modeled and attributed to trapping in natural defects [51]. They also identified a second high-temperature peak between 600 and 650 K due to D bubble formation [51]. The large drop in the D content of region B at around 450 K shown in Figure 6.12 follows the behavior reported by Ogorodnikova et al. [51], which indicates that more D within region B is trapped in natural defects than in bubbles, which would be released at higher temperatures. In the case presented in Figure 6.12, such observations would not be possible from the TDS signal alone, as it is dominated by the desorption from D stored in region A closer to the surface. Only identifying contributions from different depths in the ERDA measurement allows such insights from a case, where implantation in ion-induced effects also plays a significant role.

For the D atoms trapped in such ion-induced defects within region A, much higher temperatures are necessary to cause detrapping and subsequent desorption. D from region A only seems to be completely removed at the maximum reached heating temperature of around 1400 K. In comparison, depletion of 3 keV D at fluences of 10^{22} D/m², but at irradiation temperatures of around 400 K, was already observed at lower temperatures between 800 and 900 K by Ogorodnikova et al. [238]. However, the temperatures necessary to deplete all D are in agreement with Tyburska et al. and references therein [230], who state that some vacancy clustering defects require up to 1350 K to be removed.

The TDS signal for the desorption of D₂ gives an additional representation of the total amount of D that is removed from the sample. As its behavior agrees well with the development of the remaining D in region A, this does not indicate that a significant amount of D is retained in the sample beyond the ERDA information depth of 350 nm. However, only desorbed species with a mass of 4 amu were tracked and

additional D desorption could happen in the form of other molecules. Nevertheless, future investigations using the in-situ ERDA approach could be optimized with a lower He ERDA beam energy. Changing this parameter decreases the method's information depth, but at the same time a higher depth resolution becomes possible. This might improve the method beyond simply distinguishing between two regions of different trapping states, but could actually allow the observation of developing depth profiles while the sample is heated up.

Nevertheless, even the above presented measurements show how ERDA can give access to the observation of different D retention and desorption mechanisms that occur at different depths and would otherwise not be retrievable from only recording a TDS signal. This method will thus further be improved in the future and applied to other fusion-relevant materials such as Be to gain more insights into fusion-relevant retention effects of H isotopes.

6.3 Conclusions and Outlook

In the two previous sections, different experimental approaches of using IBA methods for the in-situ measurement of the retention and depletion of H isotopes in W samples were presented.

^{15}N NRA profiling of H has the large advantage of a very precise depth resolution. However, it was found that the required large beam fluences lead to a significant amount of additionally induced defects in the sample, which then affects H retention and possible blister formations. The damaging of the sample will be mitigated by varying the analysis spots or an improved detector geometry that requires shorter measurements, but it still seems to represent a general problem for studying H retention with this technique. While ^{15}N NRA was not found to be very well suitable for the original purpose of in-situ H retention analysis, some conclusions could be drawn on how H will be trapped in blisters in the interfaces of redeposited W layers and how neutron-induced damages could prevent this effect. Further experiments on H retention in such redeposited W layers will be performed in the scope of the upcoming EUROFUSION program and the role of pre-existing damages should be further investigated there.

In comparison to ^{15}N NRA, results of using ERDA for monitoring the D content implanted in a W sample during a TDS measurement were much more promising. The ability to continuously measure a whole depth range at the same time reveals several different D retention behaviors that cannot be retrieved from recording the desorbed D alone. Further ERDA+TDS investigations of other systems in the future will, therefore, lead to more new insights into the complex fuel retention processes in a nuclear fusion reactor.

Conclusion and Outlook

Within the scope of this thesis, several aspects of ion-solid interaction in the keV ion range with the background of space weathering and nuclear fusion research were investigated in both experiment and simulation. For space weathering, mostly sputtering by a wide array of different ions was examined to get a better understanding of how these ions affect erosion of planetary surfaces. In the area of nuclear fusion, new investigation methods for in-situ IBA of retained H isotopes were tested in cooperation with the University of Uppsala. The achieved results in both areas have already led to significant knowledge gains and represent an important basis for further research on these topics in the future.

Using the established QCM technique, sputtering of thin mineral films deposited from PLD was measured extensively. Using primarily wollastonite CaSiO_3 as an analogue for the Lunar and Hermean surfaces, sputtering of the major solar wind ions H and He as well as the minor multiply charged ions could be quantified much more precisely than in previous studies. For the kinetic sputtering contribution, simulation input parameters were found that allow a consistently precise reproduction of experimental results for singly charged ions. Using the same parameters has also led to reliable simulations of sputtering for other silicate minerals, so far revealing a similar sputtering behavior for this class of materials. H and He implantation were also observed in the experiment, showing how solar wind ions can be retained in planetary regolith.

For the potential sputtering of He^{2+} and multiply charged Ar ions, significant increases in sputtering were observed compared to singly charged ions, which scale linearly with the ion's potential energy. For both ion species, the measured dynamics of potential sputtering could be connected to a preferential sputtering of surface O, which ultimately causes a decrease of the O content in the equilibrium. The experimental results could be very well reproduced for both He^{2+} and multiply charged Ar irradiations by modeling the effect of surface composition changes on the total sputtering yields. Based on the achieved findings, the contribution of potential sputtering by solar wind He^{2+} ions to the total sputtering was estimated to

be at around 40%, which proves that this effect must not be neglected for the space weathering of planetary surfaces.

A different background was explored for the measurement of the sputtering of augite films as an analog for the Martian moon Phobos. Its space weathering by ions from the Martian atmosphere was investigated by irradiating augite samples with O^+ , O_2^+ , C^+ and CO_2^+ ions. The experiments showed significant implantation of O ions in the augite films even in the steady state, which is thought to be connected to the Fe content of the sample. Molecular O_2^+ behave the same as independent atomic ions in the low keV range, which was also found for CO_2^+ ions, when compared to O^+ and C^+ ions. Based on these findings, the total space weathering by ion impact on Phobos could be assessed: While the importance of sputtering by O^+ ions might have been overstated before, the studies in this thesis still support that planetary O ions are the dominant source for Phobos sputtering in the Martian magnetotail region. CO_2 ions, on the other hand, will most likely be negligible for the space weathering of the Martian moon. The implantation of O ions and the significant sputtering asymmetry of the tidally locked Phobos will be of great interest for future exploration endeavors such as the MMX mission.

Using thin films on a QCM have so far been a well-suited planetary analog for space weathering investigations, but there are still limits to the regolith properties that can be achieved with these samples. Especially crystallinity and grain-size effects cannot be considered and additionally, the applicability of PLD is restricted to some materials where the band gap is low enough. For this reason, an adapted circular catcher-QCM setup has been developed for the use of pressed mineral pellet targets [105, 167]. While being more challenging for the measurement of total sputtering yields, new insights on the erosion of realistic samples will be possible as well as on the angular distribution of sputtered particles, which is an important input for exosphere calculations. These experimental investigations will be accompanied by new modeling efforts focusing on the simulation of rough and granular regolith-like structures. The simulations will be achieved by using the 3D version of SDTrimSP as well as a newly developed ray-tracing code [104], which will allow a further improved understanding of the sputtering of planetary surfaces.

In the area of plasma-wall interaction research, several studies on the in-situ IBA investigation of H retention in W were performed. ^{15}N NRA gives precise insights into the depth distribution of H in W, but prolonged irradiation during analysis proved

to be very invasive for the actual experiment. Most evidently, blister formation on a W film sample after H implantation was completely suppressed inside the NRA analysis spot. This behavior could be connected to the additional damages caused by the ^{15}N ion beam. These ions create stable trapping sites for implanted H and prevents them from diffusing to the W film interface, where the blisters are formed. These observations show how the consistent influx of neutrons in a fusion reactor could diminish or even prevent the formation of H blisters underneath redeposited W layers.

In contrast to ^{15}N NRA, ERDA proved as a much better alternative for in-situ IBA investigations. For the first time, the development of the D depth distribution could be monitored, while the sample was heated up. While the retention and desorption mechanism that were observed agree with previous findings, ERDA allows much more nuanced insights into how different H components diffuse and desorb. With a fine-tuned depth resolution, in-situ ERDA will be a powerful tool for investigating complex retention mechanisms in systems that have not yet been investigated as precisely.

Further advances for in-situ IBA can also be expected in the area of sputtering and material modification research, where a EUROfusion Enabling Research (ENR) project has recently been funded for a cooperation between TU Wien and Uppsala University. Its main focus is investigating the underlying fundamental properties of ion-solid interaction for fusion-relevant materials, but within the scope of this project combining QCM and IBA measurements are also planned. These experiments will allow new insights into the sputtering of composite materials as the surface composition changes. Such a new setup could, however, also bring new chances for space weathering research. Sputtering connected to changes of the surface composition is an effect that is especially relevant for composite materials and this effect could be very well investigated by performing QCM measurements in combination with in-situ IBA. Furthermore, in-situ ERDA experiments with planetary analog material would also allow the detailed quantification and profiling of implanted H, He and O ions, which has not been done before in this form. It will definitely be interesting to see, which further insights these new approaches can bring to both space weathering and nuclear fusion research.

Bibliography

- [1]B. Hapke. “Space weathering from Mercury to the asteroid belt”. In: *Journal of Geophysical Research: Planets* 106.E5 (2001), pp. 10039–10073 (cit. on pp. 1, 12).
- [2]C. M. Pieters, L. A. Taylor, S. K. Noble, et al. “Space weathering on airless bodies: Resolving a mystery with lunar samples”. In: *Meteoritics & Planetary Science* 35.5 (2000), pp. 1101–1107 (cit. on p. 1).
- [3]B. E. Clark, B. Hapke, C. Pieters, and D. Britt. “Asteroid space weathering and regolith evolution”. In: *Asteroids III* 585 (2002), pp. 90086–2 (cit. on p. 1).
- [4]W. E. McClintock, E. T. Bradley, R. J. Vervack, et al. “Mercury’s exosphere: Observations during MESSENGER’s first Mercury flyby”. In: *Science* 321.5885 (2008), pp. 92–94 (cit. on p. 1).
- [5]A. E. Potter and T. H. Morgan. “Discovery of sodium and potassium vapor in the atmosphere of the Moon”. In: *Science* 241.4866 (1988), pp. 675–680 (cit. on p. 1).
- [6]C. T. Russell, J. G. Luhmann, and R. J. Strangeway. *Space Physics: An Introduction*. Cambridge University Press, 2016 (cit. on pp. 1, 12).
- [7]F. Aumayr and H. P. Winter. “Potential sputtering”. In: *Philosophical Transactions of the Royal Society of London A: Mathematical, Physical and Engineering Sciences* 362.1814 (2004), pp. 77–102 (cit. on pp. 2, 10, 11, 67, 74).
- [8]C. M. Pieters and S. K. Noble. “Space weathering on airless bodies”. In: *Journal of Geophysical Research: Planets* 121.10 (2016), pp. 1865–1884 (cit. on p. 2).
- [9]B. Wirth, K. Nordlund, D. Whyte, and D. Xu. “Fusion materials modeling: Challenges and opportunities”. In: *MRS bulletin* 36.3 (2011), pp. 216–222 (cit. on p. 3).
- [10]R. Wilhelm. “Ion-Solid Interaction”. In: *Lecture Notes* (2019) (cit. on pp. 6, 7, 45, 124).
- [11]J. F. Ziegler and J. P. Biersack. “The stopping and range of ions in matter”. In: *Treatise on heavy-ion science*. Springer, 1985, pp. 93–129 (cit. on pp. 6, 45, 47).
- [12]W. Wilson, L. Haggmark, and J. Biersack. “Calculations of nuclear stopping, ranges, and straggling in the low-energy region”. In: *Physical Review B* 15.5 (1977), p. 2458 (cit. on pp. 6, 45).
- [13]L. H. Thomas. “The calculation of atomic fields”. In: *Mathematical proceedings of the Cambridge philosophical society*. Vol. 23. 5. Cambridge University Press, 1927, pp. 542–548 (cit. on p. 7).

- [14]E. Fermi. “A statistical method for determining some properties of the atoms and its application to the theory of the periodic table of elements”. In: *Z. Phys* 48.1-2 (1928), pp. 73–79 (cit. on p. 7).
- [15]J. Ziegler. “The electronic and nuclear stopping of energetic ions”. In: *Applied Physics Letters* 31.8 (1977), pp. 544–546 (cit. on p. 7).
- [16]W. Eckstein and R. Preuss. “New fit formulae for the sputtering yield”. In: *Journal of Nuclear Materials* 320.3 (2003), pp. 209–213 (cit. on pp. 7, 10, 11, 56, 102).
- [17]E. Fermi and E. Teller. “The capture of negative mesotrons in matter”. In: *Physical Review* 72.5 (1947), p. 399 (cit. on p. 7).
- [18]O. Firsov. “A qualitative interpretation of the mean electron excitation energy in atomic collisions”. In: *Zhur. Eksptl'. i Teoret. Fiz.* 36 (1959) (cit. on p. 7).
- [19]J. Lindhard and M. Scharff. “Energy Dissipation by Ions in the kev Region”. In: *Phys. Rev.* 124 (1 Oct. 1961), pp. 128–130 (cit. on p. 7).
- [20]J. F. Ziegler, M. D. Ziegler, and J. P. Biersack. “SRIM–The stopping and range of ions in matter (2010)”. In: *Nuclear Instruments and Methods in Physics Research Section B: Beam Interactions with Materials and Atoms* 268.11 (2010), pp. 1818–1823 (cit. on pp. 7–9, 47, 58).
- [21]PlasmaQuest. *Sputtering Basics*. Web Page (<http://www.plasmaquest.co.uk/the-technology/sputtering-basics/>) (cit. on pp. 9, 12).
- [22]R. Behrisch and W. Eckstein. *Sputtering by Particle Bombardment: Experiments and Computer Calculations from Threshold to MeV Energies*. Springer Science & Business Media, 2007 (cit. on pp. 8, 46, 54, 57).
- [23]W. Eckstein, C. Garcia-Rosales, J. Roth, and J. László. “Threshold energy for sputtering and its dependence on angle of incidence”. In: *Nuclear Instruments and Methods in Physics Research Section B: Beam Interactions with Materials and Atoms* 83.1-2 (1993), pp. 95–109 (cit. on p. 10).
- [24]P. Sigmund. “Theory of Sputtering. I. Sputtering Yield of Amorphous and Polycrystalline Targets”. In: *Physical Review* 184.2 (1969), pp. 383–416 (cit. on pp. 10, 35, 46, 54, 57).
- [25]Y. Yamamura and S. Shindo. “An empirical formula for angular dependence of sputtering yields”. In: *Radiation effects* 80.1-2 (1984), pp. 57–72 (cit. on pp. 10, 56).
- [26]A. Mutzke, R. Schneider, W. Eckstein, et al. *SDTrimSP Version 6.00*. Report. 2019 (cit. on pp. 10, 11, 45, 47, 58).
- [27]M. Sporn, G. Libiseller, T. Neidhart, et al. “Potential sputtering of clean SiO₂ by slow highly charged ions”. In: *Physical Review Letters* 79.5 (1997), p. 945 (cit. on pp. 11, 70, 73–75).
- [28]V. Shulga and W. Eckstein. “Depth of origin of sputtered atoms for elemental targets”. In: *Nuclear Instruments and Methods in Physics Research Section B: Beam Interactions with Materials and Atoms* 145.4 (1998), pp. 492–502 (cit. on p. 11).

- [29]R. Killen, D. Hurley, and W. M. Farrell. “The effect on the lunar exosphere of a coronal mass ejection passage”. In: *Journal of Geophysical Research: Planets* 117.E10 (2012) (cit. on p. 12).
- [30]R. Brunetto and G. Strazzulla. “Elastic collisions in ion irradiation experiments: A mechanism for space weathering of silicates”. In: *Icarus* 179.1 (2005), pp. 265–273 (cit. on p. 12).
- [31]M. Sarantos, R. M. Killen, A. S. Sharma, and J. A. Slavin. “Influence of plasma ions on source rates for the lunar exosphere during passage through the Earth’s magnetosphere”. In: *Geophysical Research Letters* 35.4 (2008) (cit. on p. 13).
- [32]A. Mura, P. Wurz, H. I. M. Lichtenegger, et al. “The sodium exosphere of Mercury: Comparison between observations during Mercury’s transit and model results”. In: *Icarus* 200.1 (2009), pp. 1–11 (cit. on p. 13).
- [33]M. H. Burger, R. M. Killen, R. J. Vervack, et al. “Monte Carlo modeling of sodium in Mercury’s exosphere during the first two MESSENGER flybys”. In: *Icarus* 209.1 (2010), pp. 63–74 (cit. on p. 13).
- [34]P. Wurz, J. A. Whitby, U. Rohner, et al. “Self-consistent modelling of Mercury’s exosphere by sputtering, micro-meteorite impact and photon-stimulated desorption”. In: *Planetary and Space Science* 58.12 (2010), pp. 1599–1616 (cit. on p. 13, 47).
- [35]G. K. Wehner, C. Kenknight, and D. L. Rosenberg. “Sputtering rates under solar-wind bombardment”. In: *Planetary and Space Science* 11.8 (1963), pp. 885–895 (cit. on p. 13).
- [36]G. Betz and G. K. Wehner. “Sputtering of multicomponent materials”. In: *Sputtering by Particle Bombardment II*. Springer, 1983, pp. 11–90 (cit. on p. 13).
- [37]M. P. Seah and T. S. Nunney. “Sputtering yields of compounds using argon ions”. In: *Journal of Physics D: Applied Physics* 43.25 (2010), p. 253001 (cit. on p. 13).
- [38]R. Johnson and R. Baragiola. “Lunar surface: Sputtering and secondary ion mass spectrometry”. In: *Geophysical Research Letters* 18.11 (1991), pp. 2169–2172 (cit. on p. 13).
- [39]C. Dukes, R. Baragiola, and L. McFadden. “Surface modification of olivine by H+ and He+ bombardment”. In: *Journal of Geophysical Research: Planets* 104.E1 (1999), pp. 1865–1872 (cit. on p. 13).
- [40]M. J. Loeffler, C. A. Dukes, and R. A. Baragiola. “Irradiation of olivine by 4 keV He+: Simulation of space weathering by the solar wind”. In: *Journal of Geophysical Research: Planets* 114.E3 (2009) (cit. on p. 13).
- [41]C. A. Dukes, W.-Y. Chang, M. Famá, and R. A. Baragiola. “Laboratory studies on the sputtering contribution to the sodium atmospheres of Mercury and the Moon”. In: *Icarus* 212.2 (2011), pp. 463–469 (cit. on p. 13).
- [42]F. W. Meyer, P. R. Harris, C. N. Taylor, et al. “Sputtering of lunar regolith simulant by protons and singly and multicharged Ar ions at solar wind energies”. In: *Nuclear Instruments and Methods in Physics Research Section B: Beam Interactions with Materials and Atoms* 269.11 (2011), pp. 1316–1320 (cit. on p. 13, 50).

- [43]H. Hijazi, M. E. Bannister, H. M. Meyer, et al. “Anorthite sputtering by H⁺ and Arq⁺ (q= 1–9) at solar wind velocities”. In: *Journal of Geophysical Research: Space Physics* 119.10 (2014), pp. 8006–8016 (cit. on pp. 13, 40, 50).
- [44]H. Hijazi, M. Bannister, H. Meyer, C. M. Rouleau, and F. Meyer. “Kinetic and potential sputtering of an anorthite-like glassy thin film”. In: *Journal of Geophysical Research: Planets* 122.7 (2017), pp. 1597–1609 (cit. on pp. 13, 40, 50, 73–75, 81, 82).
- [45]J. Paméla, G. F. Matthews, V. Philipps, R. Kamendje, J.-E. Contributors, et al. “An ITER-like wall for JET”. In: *Journal of nuclear materials* 363 (2007), pp. 1–11 (cit. on p. 14).
- [46]S. Brezinsek, J. Coenen, T. Schwarz-Selinger, et al. “Plasma–wall interaction studies within the EUROfusion consortium: progress on plasma-facing components development and qualification”. In: *Nuclear fusion* 57.11 (2017), p. 116041 (cit. on p. 14).
- [47]G. Matthews, M. Beurskens, S. Brezinsek, et al. “JET ITER-like wall—overview and experimental programme”. In: *Physica Scripta* 2011.T145 (2011), p. 014001 (cit. on p. 14).
- [48]S. Brezinsek et al. “Plasma-surface interaction in the Be/W environment: Conclusions drawn from the JET-ILW for ITER”. In: *Journal of Nuclear Materials* 463 (2015), pp. 11–21 (cit. on p. 14).
- [49]T. Tanabe. “Review of hydrogen retention in tungsten”. In: *Physica Scripta* 2014.T159 (2014), p. 014044 (cit. on p. 14).
- [50]M. Oberkofler, M. Reinelt, A. Allouche, S. Lindig, and C. Linsmeier. “Towards a detailed understanding of the mechanisms of hydrogen retention in beryllium”. In: *Physica Scripta* T138 (2009), p. 014036 (cit. on p. 14).
- [51]O. Ogorodnikova, J. Roth, and M. Mayer. “Deuterium retention in tungsten in dependence of the surface conditions”. In: *Journal of Nuclear Materials* 313 (2003), pp. 469–477 (cit. on pp. 14, 120, 128, 129).
- [52]M. Poon, A. Haasz, and J. Davis. “Modelling deuterium release during thermal desorption of D⁺-irradiated tungsten”. In: *Journal of Nuclear Materials* 374.3 (2008), pp. 390–402 (cit. on pp. 14, 39).
- [53]K. Schmid, V. Rieger, and A. Manhard. “Comparison of hydrogen retention in W and W/Ta alloys”. In: *Journal of Nuclear Materials* 426.1-3 (2012), pp. 247–253 (cit. on p. 14).
- [54]V. K. Alimov, Y. Hatano, B. Tyburska-Püschel, et al. “Deuterium retention in tungsten damaged with W ions to various damage levels”. In: *Journal of nuclear materials* 441.1-3 (2013), pp. 280–285 (cit. on p. 14).
- [55]S. Markelj, T. Schwarz-Selinger, A. Založnik, et al. “Deuterium retention in tungsten simultaneously damaged by high energy W ions and loaded by D atoms”. In: *Nuclear Materials and Energy* 12 (2017), pp. 169–174 (cit. on p. 14).

- [56] B. M. Berger, R. Stadlmayr, D. Blöchl, et al. “Erosion of Fe-W model system under normal and oblique D ion irradiation”. In: *Nuclear Materials and Energy* 12. Supplement C (2017), pp. 468–471 (cit. on pp. 16, 21, 22, 44, 84).
- [57] E. Gruber. “Interaction of Ions with 3D and 2D Materials”. PhD thesis. TU Wien, 2017 (cit. on p. 16).
- [58] E. Galutschek, R. Trassl, E. Salzborn, F. Aumayr, and H. P. Winter. “Compact 14.5 GHz all-permanent magnet ECRIS for experiments with slow multicharged ions”. In: *Journal of Physics: Conference Series* 58.1 (2007), p. 395 (cit. on pp. 15–17).
- [59] G. Zschornack, M. Kreller, V. Ovsyannikov, et al. “Compact electron beam ion sources/traps: Review and prospects”. In: *Review of Scientific Instruments* 79.2 (2008), 02A703 (cit. on p. 17).
- [60] R. Geller. *Electron cyclotron resonance ion sources and ECR plasmas*. CRC Press, 1996 (cit. on p. 17).
- [61] E. Galutschek. “Development of a 14.5 GHz All-Permanent Magnet Multicharged ECR Ion Source for Remote Operation”. Thesis. 2005 (cit. on pp. 17, 18).
- [62] D. Weichselbaum. “Experimental sputtering of wollastonite using argon and helium-3 ions”. Bachelor’s thesis. TU Wien, 2019 (cit. on pp. 18, 33).
- [63] *Taking a closer look at LHC: Magnetic multipoles*. Web Page (https://www.lhc-closer.es/taking_a_closer_look_at_lhc/0.magnetic_multipoles) (cit. on p. 18).
- [64] G. Gerdin, W. Stygar, and F. Venneri. “Faraday cup analysis of ion beams produced by a dense plasma focus”. In: *Journal of Applied Physics* 52.5 (1981), pp. 3269–3275 (cit. on p. 20).
- [65] K. Dobes. “Erosion of Fusion Relevant Surfaces under Ion Impact”. Thesis. 2014 (cit. on pp. 21, 25, 26).
- [66] K. Kantre, M. V. Moro, D. Moldarev, et al. “SIGMA: A Set-up for In-situ Growth, Material modification and Analysis by ion beams”. In: *Nuclear Instruments and Methods in Physics Research Section B: Beam Interactions with Materials and Atoms* 463 (2020), pp. 96–100 (cit. on pp. 23, 24, 109).
- [67] K. Kantre, M. V. Moro, D. Moldarev, M. Wolff, and D. Primetzhofer. “Synthesis and in-situ characterization of photochromic yttrium oxyhydride grown by reactive e-beam evaporation”. In: *Scripta Materialia* 186 (2020), pp. 352–356 (cit. on pp. 23, 38).
- [68] P. Ström and D. Primetzhofer. “In-situ measurement of diffusion and surface segregation of W and Ta in bare and W-coated EUROFER97 during thermal annealing”. In: *Nuclear Materials and Energy* (2021), p. 100979 (cit. on p. 23).
- [69] M. Mayer, S. Möller, M. Rubel, et al. “Ion beam analysis of fusion plasma-facing materials and components: facilities and research challenges”. In: *Nuclear Fusion* 60.2 (2019), p. 025001 (cit. on p. 23).

- [70]E. Steinbauer, P. Bauer, M. Geretschläger, et al. “Energy resolution of silicon detectors: approaching the physical limit”. In: *Nuclear Instruments and Methods in Physics Research Section B: Beam Interactions with Materials and Atoms* 85.1-4 (1994), pp. 642–649 (cit. on p. 23).
- [71]A. Golczewski, K. Dobes, G. Wachter, M. Schmid, and F. Aumayr. “A quartz-crystal-microbalance technique to investigate ion-induced erosion of fusion relevant surfaces”. In: *Nuclear Instruments and Methods in Physics Research Section B: Beam Interactions with Materials and Atoms* 267.4 (2009), pp. 695–699 (cit. on p. 25).
- [72]B. M. Berger, R. Stadlmayr, G. Meisl, et al. “Transient effects during erosion of WN by deuterium ions studied with the quartz crystal microbalance technique”. In: *Nuclear Instruments and Methods in Physics Research Section B: Beam Interactions with Materials and Atoms* 382 (2016), pp. 82–85 (cit. on p. 25).
- [73]R. Stadlmayr, P. S. Szabo, B. M. Berger, et al. “Fluence dependent changes of surface morphology and sputtering yield of iron: comparison of experiments with SDTrimSP-2D”. In: *Nuclear Instruments and Methods in Physics Research Section B: Beam Interactions with Materials and Atoms* (2018) (cit. on pp. 25, 48).
- [74]G. Hayderer, M. Schmid, P. Varga, H. P. Winter, and F. Aumayr. “A highly sensitive quartz-crystal microbalance for sputtering investigations in slow ion–surface collisions”. In: *Review of Scientific Instruments* 70.9 (1999), p. 3696 (cit. on pp. 25, 30).
- [75]G. Hayderer, S. Cernusca, M. Schmid, et al. “Kinetically assisted potential sputtering of insulators by highly charged ions”. In: *Physical Review Letters* 86.16 (2001), pp. 3530–3533 (cit. on pp. 25, 70, 72, 77).
- [76]G. Hayderer, S. Cernusca, V. Hoffmann, et al. “Sputtering of Au and Al₂O₃ surfaces by slow highly charged ions”. In: *Nuclear Instruments and Methods in Physics Research Section B: Beam Interactions with Materials and Atoms* 182.1-4 (2001), pp. 143–147 (cit. on pp. 25, 70, 72).
- [77]R. Allas, A. Knudson, J. Lambert, P. Treado, and G. Reynolds. “Self-ion sputtering yields for copper, nickel, and aluminum”. In: *Nuclear Instruments and Methods in Physics Research* 194.1-3 (1982), pp. 615–619 (cit. on p. 25).
- [78]K. Sugiyama, M. Balden, S. Elgeti, et al. “Erosion of EUROFER steel by mass-selected deuterium ion bombardment”. In: *Nuclear Materials and Energy* 16 (2018), pp. 114–122 (cit. on pp. 25, 47).
- [79]J. Roth, K. Sugiyama, V. Alimov, et al. “EUROFER as wall material: Reduced sputtering yields due to W surface enrichment”. In: *Journal of Nuclear Materials* 454.1-3 (2014), pp. 1–6 (cit. on p. 25).
- [80]C. Herbig and T. Michely. “Graphene: the ultimately thin sputtering shield”. In: *2D Materials* 3.2 (2016), p. 025032 (cit. on p. 25).
- [81]G. Sauerbrey. “Verwendung von Schwingquarzen zur Wägung dünner Schichten und zur Mikrowägung”. In: *Zeitschrift für Physik* 155.2 (1959), pp. 206–222 (cit. on p. 26).

- [82]B. M. Berger. “Laboratory work on plasma-wall-interaction processes relevant for fusion experiments”. PhD thesis. TU Wien, 2017 (cit. on p. 26).
- [83]D. S. Stevens and H. F. Tiersten. “An analysis of doubly rotated quartz resonators utilizing essentially thickness modes with transverse variation”. In: *The Journal of the Acoustical Society of America* 79.6 (1986), pp. 1811–1826 (cit. on p. 26).
- [84]P. S. Szabo. “Experimental and Simulated Sputtering of Gold, Iron and Wollastonite with a Catcher-QCM Setup”. MA thesis. TU Wien, 2017 (cit. on pp. 26, 27, 35, 54, 55).
- [85]K. Dobes, M. Köppen, M. Oberkofler, et al. “Interaction of nitrogen ions with beryllium surfaces”. In: *Nuclear Instruments and Methods in Physics Research Section B: Beam Interactions with Materials and Atoms* 340 (2014), pp. 34–38 (cit. on p. 29).
- [86]H. Biber, P. S. Szabo, N. Jäggi, et al. “Solar wind Helium ion interaction with Mg and Fe rich pyroxene as Mercury surface analogue”. In: *Nuclear Instruments and Methods in Physics Research Section B: Beam Interactions with Materials and Atoms* 480 (2020), pp. 10–15 (cit. on pp. 29, 30, 39, 47, 54, 60, 61, 64–67, 89, 91, 95, 104).
- [87]P. S. Szabo, H. Biber, N. Jäggi, et al. “Experimental Insights Into Space Weathering of Phobos: Laboratory Investigation of Sputtering by Atomic and Molecular Planetary Ions”. In: *Journal of Geophysical Research: Planets* 125.12 (2020), e2020JE006583 (cit. on pp. 29, 48, 60, 85, 88–94, 96, 98, 100–104, 106).
- [88]P. S. Szabo, H. Biber, N. Jäggi, et al. “Dynamic Potential Sputtering of Lunar Analog Material by Solar Wind Ions”. In: *The Astrophysical Journal* 891.1 (2020), p. 100 (cit. on pp. 29, 48, 49, 51, 52, 58, 60, 65, 68, 69, 71, 72, 76–81).
- [89]R. Stadlmayr, P. S. Szabo, H. Biber, et al. “A high temperature dual-mode quartz crystal microbalance technique for erosion and thermal desorption spectroscopy measurements”. In: *Review of Scientific Instruments* 91.12 (2020), p. 125104 (cit. on pp. 29–31, 34, 35).
- [90]Y. Yamamura. “Computer studies of reemission and depth profiles for helium on molybdenum”. In: *Nuclear Instruments and Methods in Physics Research Section B: Beam Interactions with Materials and Atoms* 28.1 (1987), pp. 17–26 (cit. on p. 30).
- [91]R. Stadlmayr. “Erosion of Fusion Relevant Materials - Experiments and Modelling”. PhD thesis. TU Wien, 2020 (cit. on pp. 30, 34, 35).
- [92]B. Becker and M. A. Cooper. “A survey of the 2006–2009 quartz crystal microbalance biosensor literature”. In: *Journal of Molecular Recognition* 24.5 (2011), pp. 754–787 (cit. on p. 31).
- [93]R. S. Coe and M. S. Paterson. “The α - β inversion in quartz: a coherent phase transition under nonhydrostatic stress”. In: *Journal of Geophysical Research* 74.20 (1969), pp. 4921–4948 (cit. on p. 34).
- [94]A. Benjaminson and S. Stallings. “A microcomputer-compensated crystal oscillator using a dual-mode resonator”. In: *Proceedings of the 43rd Annual Symposium on Frequency Control*. IEEE. 1989, pp. 20–26 (cit. on p. 34).

- [95]P. Carrez, K. Demyk, P. Cordier, et al. “Low-energy helium ion irradiation-induced amorphization and chemical changes in olivine: Insights for silicate dust evolution in the interstellar medium”. In: *Meteoritics & Planetary Science* 37.11 (2002), pp. 1599–1614 (cit. on p. 35).
- [96]K. Schlueter, K. Nordlund, G. Hobler, et al. “Absence of a Crystal Direction Regime in which Sputtering Corresponds to Amorphous Material”. In: *Physical Review Letters* 125.22 (2020), p. 225502 (cit. on pp. 35, 46).
- [97]M. Küstner, W. Eckstein, V. Dose, and J. Roth. “The influence of surface roughness on the angular dependence of the sputter yield”. In: *Nuclear Instruments and Methods in Physics Research Section B: Beam Interactions with Materials and Atoms* 145.3 (1998), pp. 320–331 (cit. on p. 35).
- [98]R. Doerner, M. Baldwin, and P. Stangeby. “An equilibrium model for tungsten fuzz in an eroding plasma environment”. In: *Nuclear Fusion* 51.4 (2011), p. 043001 (cit. on p. 35).
- [99]T. A. Cassidy and R. E. Johnson. “Monte Carlo model of sputtering and other ejection processes within a regolith”. In: *Icarus* 176.2 (2005), pp. 499–507 (cit. on pp. 35, 83).
- [100]R. Stadlmayr, P. S. Szabo, D. Mayer, et al. “Sputtering of nanostructured tungsten and comparison to modelling with TRI3DYN”. In: *Journal of Nuclear Materials* 532 (2020), p. 152019 (cit. on p. 35).
- [101]B. M. Berger, P. S. Szabo, R. Stadlmayr, and F. Aumayr. “Sputtering measurements using a quartz crystal microbalance as a catcher”. In: *Nuclear Instruments and Methods in Physics Research Section B: Beam Interactions with Materials and Atoms* 406 (2017), pp. 533–537 (cit. on p. 35).
- [102]G. Z. Li, T. S. Matlock, D. M. Goebel, et al. “In situ plasma sputtering and angular distribution measurements for structured molybdenum surfaces”. In: *Plasma Sources Science and Technology* 26.6 (2017), p. 065002 (cit. on p. 35).
- [103]A. Galli, A. Vorburger, P. Wurz, and M. Tulej. “Sputtering of water ice films: A re-assessment with singly and doubly charged oxygen and argon ions, molecular oxygen, and electrons”. In: *Icarus* 291 (2017), pp. 36–45 (cit. on p. 35).
- [104]C. Cupak, R. Stadlmayr, P. S. Szabo, et al. “Sputtering of realistic surfaces: from nano- to microscopically rough surfaces”. Manuscript in preparation (2021) (cit. on pp. 35, 134).
- [105]H. Biber, P. S. Szabo, D. Gesell, et al. “Sputtering of Realistic Regolith Surfaces”. Manuscript in preparation (2021) (cit. on pp. 35, 134).
- [106]M. Wilde and K. Fukutani. “Hydrogen detection near surfaces and shallow interfaces with resonant nuclear reaction analysis”. In: *Surface science reports* 69.4 (2014), pp. 196–295 (cit. on pp. 36, 37).
- [107]U. Chaturvedi, U. Steiner, O. Zak, et al. “Structure at polymer interfaces determined by high-resolution nuclear reaction analysis”. In: *Applied physics letters* 56.13 (1990), pp. 1228–1230 (cit. on p. 36).

- [108]W. Lanford. “Analysis for hydrogen by nuclear reaction and energy recoil detection”. In: *Nuclear Instruments and Methods in Physics Research Section B: Beam Interactions with Materials and Atoms* 66.1-2 (1992), pp. 65–82 (cit. on p. 37).
- [109]K. Komander, M. V. Moro, S. A. Droulias, et al. “Hydrogen site location in ultrathin vanadium layers by N-15 nuclear reaction analysis”. In: *Nuclear Instruments and Methods in Physics Research Section B: Beam Interactions with Materials and Atoms* 455 (2019), pp. 57–60 (cit. on p. 37).
- [110]J. L’ecuyer, C. Brassard, C. Cardinal, et al. “An accurate and sensitive method for the determination of the depth distribution of light elements in heavy materials”. In: *Journal of Applied Physics* 47.1 (1976), pp. 381–382 (cit. on p. 38).
- [111]W. A. Bik and F. Habraken. “Elastic recoil detection”. In: *Reports on Progress in Physics* 56.7 (1993), p. 859 (cit. on p. 38).
- [112]M. Reinelt, A. Allouche, M. Oberkofler, and C. Linsmeier. “Retention mechanisms and binding states of deuterium implanted into beryllium”. In: *New Journal of Physics* 11.4 (2009), p. 043023 (cit. on p. 39).
- [113]D. Collins and W. Spicer. “The adsorption of CO, O₂, and H₂ on Pt: I. Thermal desorption spectroscopy studies”. In: *Surface Science* 69.1 (1977), pp. 85–113 (cit. on p. 38).
- [114]M. Setvin, X. Shi, J. Hulva, et al. “Methanol on anatase TiO₂ (101): Mechanistic insights into photocatalysis”. In: *ACS catalysis* 7.10 (2017), pp. 7081–7091 (cit. on p. 38).
- [115]D. Matveev, M. Wensing, L. Ferry, et al. “Reaction-diffusion modeling of hydrogen transport and surface effects in application to single-crystalline Be”. In: *Nuclear Instruments and Methods in Physics Research Section B: Beam Interactions with Materials and Atoms* 430 (2018), pp. 23–30 (cit. on p. 39).
- [116]P. B. Crandall, J. J. Gillis-Davis, and R. I. Kaiser. “Untangling the Origin of Molecular Hydrogen in the Lunar Exosphere”. In: *The Astrophysical Journal* 887.1 (2019), p. 27 (cit. on p. 39).
- [117]C. Zhu, P. B. Crandall, J. J. Gillis-Davis, et al. “Untangling the formation and liberation of water in the lunar regolith”. In: *Proceedings of the National Academy of Sciences* 116.23 (2019), pp. 11165–11170 (cit. on p. 39).
- [118]D. Dijkkamp, T. Venkatesan, X. Wu, et al. “Preparation of Y-Ba-Cu oxide superconductor thin films using pulsed laser evaporation from high T_c bulk material”. In: *Applied Physics Letters* 51.8 (1987), pp. 619–621 (cit. on p. 40).
- [119]D. H. Lowndes, D. Geohegan, A. Puzos, D. Norton, and C. Rouleau. “Synthesis of novel thin-film materials by pulsed laser deposition”. In: *Science* 273.5277 (1996), pp. 898–903 (cit. on p. 40).
- [120]H. M. Christen and G. Eres. “Recent advances in pulsed-laser deposition of complex oxides”. In: *Journal of Physics: Condensed Matter* 20.26 (2008), p. 264005 (cit. on p. 40).

- [121]F.-P. Yu, S.-L. Ou, and D.-S. Wu. “Pulsed laser deposition of gallium oxide films for high performance solar-blind photodetectors”. In: *Optical Materials Express* 5.5 (2015), pp. 1240–1249 (cit. on p. 40).
- [122]G. Wisz, I. Virt, P. Sagan, P. Potera, and R. Yavorskyi. “Structural, optical and electrical properties of Zinc Oxide layers produced by pulsed laser deposition method”. In: *Nanoscale Research Letters* 12.1 (2017), p. 253 (cit. on p. 40).
- [123]R. Dohmen, H.-W. Becker, E. Meißner, T. Etzel, and S. Chakraborty. “Production of silicate thin films using pulsed laser deposition (PLD) and applications to studies in mineral kinetics”. In: *European journal of mineralogy* 14.6 (2002), pp. 1155–1168 (cit. on p. 40).
- [124]R. Milke, R. Dohmen, H.-W. Becker, and R. Wirth. “Growth kinetics of enstatite reaction rims studied on nano-scale, Part I: Methodology, microscopic observations and the role of water”. In: *Contributions to Mineralogy and Petrology* 154.5 (2007), pp. 519–533 (cit. on p. 40).
- [125]J. M. Fernández-Pradas, P. Serra, J. L. Morenza, and P. N. De Aza. “Pulsed laser deposition of pseudowollastonite coatings”. In: *Biomaterials* 23.9 (2002), pp. 2057–2061 (cit. on p. 40).
- [126]Z. Chen, J. Zhai, D. Wang, and C. Chen. “Bioactivity of hydroxyapatite/wollastonite composite films deposited by pulsed laser”. In: *Ceramics International* 44.9 (2018), pp. 10204–10209 (cit. on p. 40).
- [127]D.-M. Miu, S.-I. Jinga, G. Voicu, and F. Iordache. “Characteristics of Wollastonite Ceramic Coatings Obtained by Pulsed Laser Deposition”. In: *Journal of Inorganic and Organometallic Polymers and Materials* (2020), pp. 1–7 (cit. on p. 40).
- [128]F. S. Baumann, J. Fleig, H.-U. Habermeier, and J. Maier. “Impedance spectroscopic study on well-defined (La, Sr)(Co, Fe) O_{3-δ} model electrodes”. In: *Solid State Ionics* 177.11-12 (2006), pp. 1071–1081 (cit. on p. 40).
- [129]G. Meisl, K. Schmid, O. Encke, et al. “Implantation and erosion of nitrogen in tungsten”. In: *New journal of physics* 16.9 (2014), p. 093018 (cit. on p. 40).
- [130]P. Lackner, A. J. Brandt, U. Diebold, and M. Schmid. “Few-monolayer yttria-doped zirconia films: Segregation and phase stabilization”. In: *The Journal of Chemical Physics* 152.6 (2020), p. 064709 (cit. on p. 40).
- [131]A. Einstein. “Über einem die Erzeugung und Verwandlung des Lichtes betreffenden heuristischen Gesichtspunkt”. In: *Annalen der Physik* 4 (1905) (cit. on p. 40).
- [132]J. F. Watts and J. Wolstenholme. *An introduction to surface analysis by XPS and AES*. Wiley, 2003 (cit. on pp. 40, 41).
- [133]M. Mayer. “Improved physics in SIMNRA 7”. In: *Nuclear Instruments and Methods in Physics Research Section B: Beam Interactions with Materials and Atoms* 332 (2014), pp. 176–180 (cit. on pp. 41, 124, 125).
- [134]C. Jeynes, N. Barradas, and E. Szilágyi. “Accurate determination of quantity of material in thin films by Rutherford backscattering spectrometry”. In: *Analytical chemistry* 84.14 (2012), pp. 6061–6069 (cit. on p. 42).

- [135]P. Ström, P. Petersson, M. Rubel, and G. Possnert. “A combined segmented anode gas ionization chamber and time-of-flight detector for heavy ion elastic recoil detection analysis”. In: *Review of Scientific Instruments* 87.10 (2016), p. 103303 (cit. on p. 43).
- [136]F. Busch, W. Pfeffer, B. Kohlmeyer, D. Schüll, and F. Pühlhoffer. “A position-sensitive transmission time detector”. In: *Nuclear Instruments and Methods* 171.1 (1980), pp. 71–74 (cit. on p. 43).
- [137]F. J. Giessibl. “Advances in atomic force microscopy”. In: *Reviews of modern physics* 75.3 (2003), p. 949 (cit. on p. 44).
- [138]D. Rugar and P. Hansma. “Atomic force microscopy”. In: *Physics today* 43.10 (1990), pp. 23–30 (cit. on p. 44).
- [139]E. Gruber, P. Salou, L. Bergen, et al. “Swift heavy ion irradiation of CaF₂—from grooves to hillocks in a single ion track”. In: *Journal of Physics: Condensed Matter* 28.40 (2016), p. 405001 (cit. on p. 44).
- [140]E. Gruber, L. Bergen, P. Salou, et al. “High resolution AFM studies of irradiated mica—following the traces of swift heavy ions under grazing incidence”. In: *Journal of Physics: Condensed Matter* 30.28 (2018), p. 285001 (cit. on p. 44).
- [141]D. C. Rapaport. *The art of molecular dynamics simulation*. Cambridge university press, 2004 (cit. on p. 44).
- [142]H. M. Urbassek. “Molecular-dynamics simulation of sputtering”. In: *Nuclear Instruments and Methods in Physics Research Section B: Beam Interactions with Materials and Atoms* 122.3 (1997), pp. 427–441 (cit. on p. 44).
- [143]M. Toulemonde, E. Paumier, and C. Dufour. “Thermal spike model in the electronic stopping power regime”. In: *Radiation Effects and Defects in Solids* 126.1-4 (1993), pp. 201–206 (cit. on p. 46).
- [144]D. Onderdelinden. “The Influence of Channeling on Cu Single-Crystal Sputtering”. In: *Applied Physics Letters* 8.8 (1966), pp. 189–190 (cit. on p. 46).
- [145]M. Posselt. “Crystal-trim and its application to investigations on channeling effects during ion implantation”. In: *Radiation Effects and Defects in Solids* 130.1 (1994), pp. 87–119 (cit. on p. 46).
- [146]J. Lindhard, M. Scharff, and H. E. Schiøtt. *Range concepts and heavy ion ranges*. Munksgaard Copenhagen, 1963 (cit. on p. 46).
- [147]O. S. Oen and M. T. Robinson. “Computer studies of the reflection of light ions from solids”. In: *Nuclear instruments and Methods* 132 (1976), pp. 647–653 (cit. on p. 46).
- [148]P. Wurz, U. Rohner, J. A. Whitby, et al. “The lunar exosphere: The sputtering contribution”. In: *Icarus* 191.2 (2007), pp. 486–496 (cit. on p. 47).
- [149]Q. Nénon and A. R. Poppe. “On the Long-term Weathering of Airless Body Surfaces by the Heavy Minor Ions of the Solar Wind: Inputs from Ion Observations and SRIM Simulations”. In: *The Planetary Science Journal* 1.3 (2020), p. 69 (cit. on pp. 47, 82, 108).

- [150]H. Hofsäss, K. Zhang, and A. Mutzke. “Simulation of ion beam sputtering with SDTrimSP, TRIDYN and SRIM”. In: *Applied Surface Science* 310 (2014), pp. 134–141 (cit. on p. 47).
- [151]M. Schaible, C. Dukes, A. Hutcherson, et al. “Solar wind sputtering rates of small bodies and ion mass spectrometry detection of secondary ions”. In: *Journal of Geophysical Research: Planets* 122.10 (2017), pp. 1968–1983 (cit. on pp. 47, 48, 62).
- [152]J. Biersack and W. Eckstein. “Sputtering studies with the Monte Carlo program TRIM. SP”. In: *Applied Physics A* 34.2 (1984), pp. 73–94 (cit. on p. 47).
- [153]W. Möller and W. Eckstein. “Tridyn — A TRIM simulation code including dynamic composition changes”. In: *Nuclear Instruments and Methods in Physics Research Section B: Beam Interactions with Materials and Atoms* 2.1-3 (1984), pp. 814–818 (cit. on p. 47).
- [154]W. Moller, W. Eckstein, and J. P. Biersack. “Tridyn - Binary Collision Simulation of Atomic-Collisions and Dynamic Composition Changes in Solids”. In: *Computer Physics Communications* 51.3 (1988), pp. 355–368 (cit. on p. 47).
- [155]J. Schmitz, A. Mutzke, A. Litnovsky, et al. “Preferential sputtering induced Cr-Diffusion during plasma exposure of WCrY smart alloys”. In: *Journal of Nuclear Materials* 526 (2019), p. 151767 (cit. on p. 47).
- [156]U. von Toussaint, A. Mutzke, K. Sugiyama, and T. Schwarz-Selinger. “Simulation of coupled sputter-diffusion effects”. In: *Physica Scripta* 2016.T167 (2016), p. 014023 (cit. on p. 47).
- [157]A. Mutzke, R. Schneider, and G. Bandelow. “SDTrimSP-2D: Simulation of Particles Bombarding on a Two Dimensional Target-Version 2.0”. In: *IPP Report 12/11* (2013) (cit. on p. 48).
- [158]U. von Toussaint, A. Mutzke, and A. Manhard. “Sputtering of rough surfaces: a 3D simulation study”. In: *Physica Scripta* Volume 2017.T170 (2017), p. 014056 (cit. on pp. 48, 89).
- [159]R. Arredondo, M. Oberkofler, T. Schwarz-Selinger, et al. “Angle-dependent sputter yield measurements of keV D ions on W and Fe and comparison with SDTrimSP and SDTrimSP-3D”. In: *Nuclear Materials and Energy* 18 (2019), pp. 72–76 (cit. on p. 48).
- [160]U. von Toussaint and A. Mutzke. “Fluence Dependent Changes of Erosion Yields and Surface Morphology of the Iron-Tungsten Model System: SDTrimSP-2D Simulation Studies”. In: *Nuclear Materials and Energy* 12 (2017), pp. 318–322 (cit. on p. 48).
- [161]R. Arredondo, M. Balden, A. Mutzke, et al. “Impact of surface enrichment and morphology on sputtering of EUROFER by deuterium”. In: *Nuclear Materials and Energy* (2020), p. 100749 (cit. on p. 48).
- [162]P. S. Szabo, R. Chiba, H. Biber, et al. “Solar Wind Sputtering of Wollastonite as a Lunar Analogue Material—Comparisons between Experiments and Simulation”. In: *Icarus* 314 (2018), pp. 98–105 (cit. on pp. 48, 49, 52, 55, 61–63, 73).

- [163] A. F. Barghouty, F. W. Meyer, P. R. Harris, and J. H. Adams. “Solar-wind protons and heavy ions sputtering of lunar surface materials”. In: *Nuclear Instruments and Methods in Physics Research Section B: Beam Interactions with Materials and Atoms* 269.11 (2011), pp. 1310–1315 (cit. on pp. 50, 54, 74, 81, 82).
- [164] S. T. Alnussirat, A. F. Barghouty, J. E. Edmunson, M. S. Sabra, and D. L. Rickman. “Contributions of solar-wind induced potential sputtering to the lunar surface erosion rate and it’s exosphere”. In: *Nuclear Instruments and Methods in Physics Research Section B: Beam Interactions with Materials and Atoms* 420 (2018), pp. 33–39 (cit. on pp. 50, 74, 82).
- [165] N. Yamashita, O. Gasnault, O. Forni, et al. “The global distribution of calcium on the Moon: Implications for high-Ca pyroxene in the eastern mare region”. In: *Earth and Planetary Science Letters* 353 (2012), pp. 93–98 (cit. on p. 50).
- [166] A. Sprague, J. Emery, K. Donaldson, et al. “Mercury: Mid-infrared (3–13.5 μm) observations show heterogeneous composition, presence of intermediate and basic soil types, and pyroxene”. In: *Meteoritics & Planetary Science* 37.9 (2002), pp. 1255–1268 (cit. on p. 50).
- [167] N. Jäggi, A. Galli, P. Wurz, et al. “Creation of Lunar and Hermean analogue mineral powder samples for solar wind irradiation experiments and mid-infrared spectra analysis”. In: *Icarus* 365 (2021), p. 114492 (cit. on pp. 52, 134).
- [168] W. A. Deer, R. A. Howie, and J. Zussman. *Rock-forming minerals: single-chain silicates, Volume 2A*. 1997 (cit. on p. 52).
- [169] K. Wittmaack, A. Giordani, R. Umbel, and J. L. Hunter Jr. “Order-of-magnitude differences in retention of low-energy Ar implanted in Si and SiO₂”. In: *Journal of Vacuum Science & Technology A: Vacuum, Surfaces, and Films* 34.5 (2016), p. 051404 (cit. on p. 54).
- [170] R. Kelly. “On the problem of whether mass or chemical bonding is more important to bombardment-induced compositional changes in alloys and oxides”. In: *Surface Science* 100.1 (1980), pp. 85–107 (cit. on p. 57).
- [171] J. Malherbe, S. Hofmann, and J. Sanz. “Preferential sputtering of oxides: A comparison of model predictions with experimental data”. In: *Applied Surface Science* 27.3 (1986), pp. 355–365 (cit. on p. 57).
- [172] W. Möller and M. Posselt. *TRIDYN User Manual*. Research rep. Forschungszentrum Rossendorf, 2001 (cit. on p. 57).
- [173] L. Morrissey, O. Tucker, R. Killen, S. Nakhla, and D. Savin. “Simulating Solar-Wind Ion Sputtering of Sodium from Silicate Minerals: The Importance of the Surface Binding Energy”. In: *52nd Lunar and Planetary Science Conference 2021*. 2021 (cit. on pp. 57, 60).
- [174] H. Lammer, P. Wurz, M. Patel, et al. “The variability of Mercury’s exosphere by particle and radiation induced surface release processes”. In: *Icarus* 166.2 (2003), pp. 238–247 (cit. on p. 57).

- [175]L. Skopinski, P. Ernst, M. Herder, et al. “Time-of-flight mass spectrometry of particle emission during irradiation with slow, highly charged ions”. In: *Review of Scientific Instruments* 92.2 (2021), p. 023909 (cit. on p. 60).
- [176]X. Yang and A. Hassanein. “Atomic scale calculations of tungsten surface binding energy and beryllium-induced tungsten sputtering”. In: *Applied surface science* 293 (2014), pp. 187–190 (cit. on p. 60).
- [177]K. Dobes, P. Naderer, N. Lachaud, C. Eisenmenger-Sittner, and F. Aumayr. “Sputtering of tungsten by N⁺ and N₂⁺ ions: investigations of molecular effects”. In: *Physica Scripta T145* (2011), p. 014017 (cit. on pp. 61, 98).
- [178]H. Lord. “Hydrogen and helium ion implantation into olivine and enstatite: Retention coefficients, saturation concentrations, and temperature-release profiles”. In: *Journal of Geophysical Research* 73.16 (1968), pp. 5271–5280 (cit. on pp. 62, 64).
- [179]M. J. Schaible and R. A. Baragiola. “Hydrogen implantation in silicates: the role of solar wind in SiOH bond formation on the surfaces of airless bodies in space”. In: *Journal of Geophysical Research: Planets* 119.9 (2014), pp. 2017–2028 (cit. on pp. 62, 64).
- [180]D. Roth, B. Bruckner, G. Undeutsch, et al. “Electronic stopping of slow protons in oxides: scaling properties”. In: *Physical review letters* 119.16 (2017), p. 163401 (cit. on p. 65).
- [181]DREEBIT. *DREEBIT Ionization Database*. Web Page (<http://www.dreebit-ibt.com/ionization-energy-database.html>). 2018 (cit. on p. 73).
- [182]G. Hayderer, M. Schmid, P. Varga, et al. “Threshold for Potential Sputtering of LiF”. In: *Physical Review Letters* 83.19 (1999), pp. 3948–3951 (cit. on p. 74).
- [183]T. Neidhart, F. Pichler, F. Aumayr, et al. “Potential sputtering of lithium fluoride by slow multicharged ions”. In: *Physical Review Letters* 74.26 (1995), p. 5280 (cit. on p. 74).
- [184]L. Wirtz, G. Hayderer, C. Lemell, et al. “Curve-crossing analysis for potential sputtering of insulators”. In: *Surface science* 451.1-3 (2000), pp. 197–202 (cit. on p. 74).
- [185]B. M. Jones, A. Aleksandrov, K. Hibbitts, M. Dyar, and T. M. Orlando. “Solar wind-induced water cycle on the Moon”. In: *Geophysical Research Letters* 45.20 (2018), pp. 10–959 (cit. on p. 83).
- [186]A. Poppe, M. Fillingim, J. Halekas, J. Raeder, and V. Angelopoulos. “ARTEMIS observations of terrestrial ionospheric molecular ion outflow at the Moon”. In: *Geophysical Research Letters* 43.13 (2016), pp. 6749–6758 (cit. on p. 84).
- [187]S. Li, P. G. Lucey, A. A. Fraeman, et al. “Widespread hematite at high latitudes of the Moon”. In: *Science advances* 6.36 (2020), eaba1940 (cit. on pp. 84, 97, 108).
- [188]Q. Nénon, A. Poppe, A. Rahmati, and J. McFadden. “Implantation of Martian atmospheric ions within the regolith of Phobos”. In: *Nature Geoscience* (2021), pp. 1–6 (cit. on pp. 84, 107, 108).

- [189]P. Thomas and J. Veverka. “Crater densities on the satellites of Mars”. In: *Icarus* 41.3 (1980), pp. 365–380 (cit. on p. 85).
- [190]A. Rivkin, R. H. Brown, D. E. Trilling, J. Bell III, and J. Plassmann. “Near-infrared spectrophotometry of Phobos and Deimos”. In: *Icarus* 156.1 (2002), pp. 64–75 (cit. on p. 85).
- [191]M. Pajola, M. Lazzarin, C. Dalle Ore, et al. “Phobos as a D-type captured asteroid, spectral modeling from 0.25 to 4.0 μm ”. In: *The Astrophysical Journal* 777.2 (2013), p. 127 (cit. on p. 85).
- [192]R. Hyodo, H. Genda, S. Charnoz, and P. Rosenblatt. “On the impact origin of Phobos and Deimos. I. Thermodynamic and physical aspects”. In: *The Astrophysical Journal* 845.2 (2017), p. 125 (cit. on p. 85).
- [193]R. Canup and J. Salmon. “Origin of Phobos and Deimos by the impact of a Vesta-to-Ceres sized body with Mars”. In: *Science advances* 4.4 (2018), eaar6887 (cit. on p. 85).
- [194]R. M. Canup and E. Asphaug. “Origin of the Moon in a giant impact near the end of the Earth’s formation”. In: *Nature* 412.6848 (2001), pp. 708–712 (cit. on p. 85).
- [195]A. Bagheri, A. Khan, M. Efroimsky, M. Kruglyakov, and D. Giardini. “Dynamical evidence for Phobos and Deimos as remnants of a disrupted common progenitor”. In: *Nature Astronomy* (2021), pp. 1–5 (cit. on p. 86).
- [196]S. Campagnola, C. H. Yam, Y. Tsuda, N. Ogawa, and Y. Kawakatsu. “Mission analysis for the Martian Moons Explorer (MMX) mission”. In: *Acta Astronautica* 146 (2018), pp. 409–417 (cit. on p. 86).
- [197]Q. Nénon, A. R. Poppe, A. Rahmati, and J. P. McFadden. “Implantation of Martian atmospheric ions within the regolith of Phobos”. In: *Nature Geosciences* (2021) (cit. on pp. 86, 87).
- [198]A. Witze, S. Mallapaty, and E. Gibney. “Invasion des Roten Planeten”. In: *Sterne und Weltraum* 10/2020 (2020), pp. 26–34 (cit. on p. 87).
- [199]F. Cipriani, O. Witasse, F. Leblanc, R. Modolo, and R. E. Johnson. “A model of interaction of Phobos’ surface with the Martian environment”. In: *Icarus* 212.2 (2011), pp. 643–648 (cit. on pp. 86, 89).
- [200]A. Poppe and S. Curry. “Martian planetary heavy ion sputtering of Phobos”. In: *Geophysical Research Letters* 41.18 (2014), pp. 6335–6341 (cit. on pp. 86, 89, 105).
- [201]R. Ramstad, S. Barabash, Y. Futaana, H. Nilsson, and M. Holmström. “Global Mars-solar wind coupling and ion escape”. In: *Journal of Geophysical Research: Space Physics* 122.8 (2017), pp. 8051–8062 (cit. on p. 86).
- [202]E. Dubinin, D. Winningham, M. Fränz, et al. “Solar wind plasma protrusion into the Martian magnetosphere: ASPERA-3 observations”. In: *Icarus* 182.2 (2006), pp. 343–349 (cit. on p. 86).
- [203]S. Barabash, A. Fedorov, R. Lundin, and J.-A. Sauvaud. “Martian atmospheric erosion rates”. In: *Science* 315.5811 (2007), pp. 501–503 (cit. on p. 86).

- [204]P. R. Mahaffy, C. R. Webster, S. K. Atreya, et al. “Abundance and isotopic composition of gases in the Martian atmosphere from the Curiosity rover”. In: *Science* 341.6143 (2013), pp. 263–266 (cit. on p. 87).
- [205]P. R. Mahaffy, M. Benna, M. Elrod, et al. “Structure and composition of the neutral upper atmosphere of Mars from the MAVEN NGIMS investigation”. In: *Geophysical research letters* 42.21 (2015), pp. 8951–8957 (cit. on p. 87).
- [206]Q. Nenon, A. R. Poppe, A. Rahmati, et al. “Phobos surface sputtering as inferred from MAVEN ion observations”. In: *Journal of Geophysical Research: Planets* 124.124 (2019), pp. 3385–3401 (cit. on pp. 87, 98, 99, 104, 105).
- [207]B. M. Jakosky, R. Lin, J. Grebowsky, et al. “The Mars atmosphere and volatile evolution (MAVEN) mission”. In: *Space Science Reviews* 195.1-4 (2015), pp. 3–48 (cit. on p. 87).
- [208]P. Vernazza, F. Cipriani, C. Dukes, et al. “Meteorite analogs for Phobos and Deimos: Unraveling the origin of the Martian moons”. In: *Meteoritics and Planetary Science Supplement* 73 (2010), p. 5076 (cit. on p. 89).
- [209]K. R. Kuhlman, K. Sridharan, and A. Kvit. “Simulation of solar wind space weathering in orthopyroxene”. In: *Planetary and Space Science* 115 (2015), pp. 110–114 (cit. on p. 97).
- [210]H. Andersen and H. Bay. “Nonlinear effects in heavy-ion sputtering”. In: *Journal of Applied Physics* 45.2 (1974), pp. 953–954 (cit. on p. 98).
- [211]H. Andersen and H. Bay. “Heavy-ion sputtering yields of gold: Further evidence of nonlinear effects”. In: *Journal of Applied Physics* 46.6 (1975), pp. 2416–2422 (cit. on p. 98).
- [212]Y. Yao, Z. Hargitai, M. Albert, et al. “New molecular collisional interaction effect in low-energy sputtering”. In: *Physical review letters* 81.3 (1998), p. 550 (cit. on p. 98).
- [213]L. Maes, M. Fraenz, J. P. McFadden, and M. Benna. “Escape of and Other Heavy Minor Ions From the Ionosphere of Mars”. In: *Journal of Geophysical Research: Space Physics* (2020), e2020JA028608 (cit. on p. 99).
- [214]J. Biersack and W. Eckstein. “Sputtering studies with the Monte Carlo program TRIM. SP”. In: *Applied Physics A* 34.2 (1984), pp. 73–94 (cit. on p. 105).
- [215]K. Terada, S. Yokota, Y. Saito, et al. “Biogenic oxygen from Earth transported to the Moon by a wind of magnetospheric ions”. In: *Nature Astronomy* 1.2 (2017), pp. 1–5 (cit. on p. 108).
- [216]T. Cassidy, A. W. Merkel, J. M. Raines, and A. N. Glass. “MESSENGER Observations of Sputtering in Mercury’s Exosphere”. In: *AGU Fall Meeting 2020* (2020) (cit. on p. 108).
- [217]K.-A. Kantre, P. S. Szabo, M. V. Moro, et al. “Combined in-situ ion beam analysis and thermal desorption spectroscopy for studying deuterium implanted in tungsten”. Manuscript in preparation (2021) (cit. on p. 109).

- [218]D. Rapp, P. Englander-Golden, and D. D. Briglia. “Cross sections for dissociative ionization of molecules by electron impact”. In: *The Journal of chemical physics* 42.12 (1965), pp. 4081–4085 (cit. on p. 111).
- [219]A. Manhard, K. Schmid, M. Balden, and W. Jacob. “Influence of the microstructure on the deuterium retention in tungsten”. In: *Journal of nuclear materials* 415.1 (2011), S632–S635 (cit. on p. 115).
- [220]G.-N. Luo, K. Umstadter, W. Shu, W. Wampler, and G.-H. Lu. “Behavior of tungsten with exposure to deuterium plasmas”. In: *Nuclear Instruments and Methods in Physics Research Section B: Beam Interactions with Materials and Atoms* 267.18 (2009), pp. 3041–3045 (cit. on p. 115).
- [221]M. Simmonds, T. Schwarz-Selinger, J. Yu, et al. “Isolating the detrapping of deuterium in heavy ion damaged tungsten via partial thermal desorption”. In: *Journal of Nuclear Materials* 522 (2019), pp. 158–167 (cit. on p. 115).
- [222]R. Doerner, M. Baldwin, T. Lynch, and J. Yu. “Retention in tungsten resulting from extremely high fluence plasma exposure”. In: *Nuclear Materials and Energy* 9 (2016), pp. 89–92 (cit. on p. 115).
- [223]J. Roth and K. Schmid. “Hydrogen in tungsten as plasma-facing material”. In: *Physica Scripta* 2011.T145 (2011), p. 014031 (cit. on p. 115).
- [224]R. Frauenfelder. “Solution and diffusion of hydrogen in tungsten”. In: *Journal of Vacuum Science and Technology* 6.3 (1969), pp. 388–397 (cit. on p. 115).
- [225]S. Nagata and K. Takahiro. “Deuterium retention in tungsten and molybdenum”. In: *Journal of nuclear materials* 283 (2000), pp. 1038–1042 (cit. on pp. 116, 118, 127).
- [226]F. Maury, M. Biget, P. Vajda, A. Lucasson, and P. Lucasson. “Frenkel pair creation and stage I recovery in W crystals irradiated near threshold”. In: *Radiation Effects* 38.1-2 (1978), pp. 53–65 (cit. on p. 117).
- [227]T. Schwarz-Selinger, J. Bauer, S. Elgeti, and S. Markelj. “Influence of the presence of deuterium on displacement damage in tungsten”. In: *Nuclear Materials and Energy* 17 (2018), pp. 228–234 (cit. on p. 117).
- [228]M. J. Banisalman, S. Park, and T. Oda. “Evaluation of the threshold displacement energy in tungsten by molecular dynamics calculations”. In: *Journal of Nuclear Materials* 495 (2017), pp. 277–284 (cit. on p. 117).
- [229]K. Heinola, T. Ahlgren, K. Nordlund, and J. Keinonen. “Hydrogen interaction with point defects in tungsten”. In: *Physical Review B* 82.9 (2010), p. 094102 (cit. on p. 118).
- [230]B. Tyburska, V. K. Alimov, O. Ogorodnikova, K. Schmid, and K. Ertl. “Deuterium retention in self-damaged tungsten”. In: *Journal of Nuclear Materials* 395.1-3 (2009), pp. 150–155 (cit. on pp. 118, 122, 129).
- [231]M. H. J. ’. Hoen, B. Tyburska-Püschel, K. Ertl, et al. “Saturation of deuterium retention in self-damaged tungsten exposed to high-flux plasmas”. In: *Nuclear Fusion* 52.2 (2012), p. 023008 (cit. on p. 118).

- [232]Y. Ueda, T. Funabiki, T. Shimada, et al. “Hydrogen blister formation and cracking behavior for various tungsten materials”. In: *Journal of nuclear materials* 337 (2005), pp. 1010–1014 (cit. on p. 119).
- [233]M. Balden, S. Lindig, A. Manhard, and J.-H. You. “D2 gas-filled blisters on deuterium-bombarded tungsten”. In: *Journal of Nuclear Materials* 414.1 (2011), pp. 69–72 (cit. on p. 119).
- [234]Y.-P. Xu, J. Wang, H.-S. Zhou, et al. “Plasma exposure behavior of re-deposited tungsten on structural materials of fusion reactors”. In: *Journal of Nuclear Materials* 488 (2017), pp. 129–133 (cit. on pp. 119, 122).
- [235]A. Haasz, J. Davis, M. Poon, and R. Macaulay-Newcombe. “Deuterium retention in tungsten for fusion use”. In: *Journal of nuclear materials* 258 (1998), pp. 889–895 (cit. on p. 120).
- [236]Y. Sakoi, M. Miyamoto, K. Ono, and M. Sakamoto. “Helium irradiation effects on deuterium retention in tungsten”. In: *Journal of Nuclear Materials* 442.1-3 (2013), S715–S718 (cit. on p. 127).
- [237]C. Taylor, M. Shimada, and B. Merrill. “Deuterium retention and blistering in tungsten foils”. In: *Nuclear Materials and Energy* 12 (2017), pp. 689–693 (cit. on p. 127).
- [238]O. Ogorodnikova, J. Roth, and M. Mayer. “Ion-driven deuterium retention in tungsten”. In: *Journal of Applied Physics* 103.3 (2008), p. 034902 (cit. on p. 129).

List of Figures

1.1	Compilation of space weathering processes.	2
1.2	Overview of plasma-wall-interaction processes.	3
2.1	Nuclear and electronic stopping of I in Si.	8
2.2	Compilation of stopping powers and ion ranges in SiO ₂	9
2.3	Sketch of ion-solid interaction.	9
2.4	Angular dependence and energy dependence of the sputtering yield.	11
2.5	Changes of surface composition due to preferential sputtering.	12
3.1	A sketch of the experimental setup for ion beam irradiations at TU Wien.	16
3.2	An overview of the working principle of the ECRIS at TU Wien.	16
3.3	The working principle of a quadrupole focusing magnet.	18
3.4	A plot of the analysis of past settings at Beamline 3.	20
3.5	A CAD model of the QCM sample holder.	21
3.6	An overview of the sample chamber setup.	22
3.7	Schematics of the SIGMA setup at Uppsala University.	24
3.8	An example for a QCM measurement.	28
3.9	A N irradiation of Be where both implantation and sputtering occur.	29
3.10	QCM temperature dependence for the fundamental mode and third overtone mode.	31
3.11	Example irradiations showing the transient effects on the frequency when the ion beam is turned on and off.	32
3.12	Analysis of the initial frequency drops at the start of the irradiation.	33
3.13	The dependence of the beat frequency $f_b = 3 \cdot f_1 - f_3$ on temperature.	34
3.14	The width of the $^1\text{H}(^{15}\text{N}, \alpha\gamma)^{12}\text{C}$ nuclear reaction.	36
3.15	The setup principle of an ERDA measurement with an absorber foil.	37
3.16	An example for a TDS measurement.	39
3.17	A spectrum from RBS analysis of a W film on a Si substrate.	41
3.18	ToF-ERDA measurement of a MgSiO ₃ film showing the capabilities of this analysis method.	43
3.19	A sketch illustrating the principle of BCA simulations.	45

4.1	Depth distribution of elements in wollastonite films from ToF-ERDA measurements.	51
4.2	Example AFM measurement results for a CaSiO ₃ sample.	52
4.3	Distribution of local inclination angles for a CaSiO ₃ sample.	53
4.4	Experimental data for Ar ⁺ irradiations of CaSiO ₃	55
4.5	Different SRIM modelling results for 2 keV Ar.	57
4.6	Different SDTrimSP modelling results for 2 keV Ar.	58
4.7	Experimental data for 1 keV and 4 keV Ar irradiations of CaSiO ₃ compared to SDTrimSP simulations.	59
4.8	Experimental data for 2 keV H ₂ ⁺ irradiations of CaSiO ₃	61
4.9	Fluence dependence of a H irradiation of CaSiO ₃ compared to SDTrimSP with included H implantation.	63
4.10	Angular dependence of H measurements compared to SDTrimSP simulation results with H implantation.	63
4.11	Sputtering yields of ⁴ He ⁺ and ³ He ⁺ ions.	65
4.12	Fluence dependence of the sputtering yield of CaSiO ₃ under ³ He ²⁺ irradiation.	68
4.13	Steady state sputtering yields of CaSiO ₃ under ³ He ⁺ and ³ He ²⁺	68
4.14	Fluence dependence of the sputtering yield of CaSiO ₃ under irradiation of 8 keV Ar ⁸⁺ ions.	71
4.15	Angular dependence of the sputtering yield of CaSiO ₃ by 8 keV Ar ⁸⁺ ions.	71
4.16	Dependence on the potential energy of initial and steady state sputtering yields for different Ar charge states.	72
4.17	A compilation of steady state sputtering yields of CaSiO ₃ for different Ar charge states.	73
4.18	Results of the potential sputtering model compared to measured sputtering yields for He.	76
4.19	Overview for the SDTrimSP error estimation for He and Ar.	77
4.20	Potential sputtering model results compared to measured sputtering yields for 8 keV Ar.	78
4.21	Steady state O concentrations for He and Ar irradiations predicted by the potential sputtering model.	79
4.22	Development of surface concentrations for solar wind irradiation of H ⁺ and He ²⁺	80
4.23	Modeled elemental sputtering yields for solar wind irradiation of H ⁺ and He ²⁺	80
5.1	An image of Phobos.	86

5.2	A sketch of the space weathering scenario of Phobos in the Martian tail region.	87
5.3	ToF-ERDA results for the augite samples.	88
5.4	Fluence dependent measurement results from O ⁺ irradiations of augite.	90
5.5	Angular dependent measurement results from O ⁺ irradiations of augite compared to SDTrimSP simulations.	91
5.6	Sputtering yields of wollastonite irradiated with O ⁺ ions.	93
5.7	Comparison of O sputtering yields for augite and wollastonite.	93
5.8	Comparison of Ar sputtering yields of augite and wollastonite.	94
5.9	Comparison of experimental and simulated sputtering yields of augite and wollastonite for different projectiles.	94
5.10	Dynamic SDTrimSP simulations accounting for both sputtering and O ion implantation.	96
5.11	Improved agreement for the measured O sputtering yields of augite with an SDTrimSP simulation including O implantation.	96
5.12	Comparison of sputtering yields of augite by atomic and molecular O ions.	98
5.13	Measurement results of C ⁺ irradiations for augite.	100
5.14	Measurement results of C ⁺ irradiations for wollastonite.	100
5.15	Measurement results of CO ₂ ⁺ irradiations on augite.	101
5.16	Simulated sputtering yields for C ⁺ , O ⁺ , CO ⁺ , O ₂ ⁺ and CO ₂ ⁺ ions at different energies.	102
5.17	Ratio of contributions from O ions and solar wind ions to the sputtering of Phobos.	106
6.1	ToF-ERDA results for the thin W films used in experiments of H retention.	110
6.2	H profiles recorded by NRA after implantation and after heating the W sample.	112
6.3	A picture of the W film sample after H implantation and NRA measurements.	113
6.4	A confocal microscopy image showing blister formation on the W sample.	113
6.5	A compilation of AFM images of the W sample after the experiments.	114
6.6	H retention in a W film from NRA results compared to literature data.	116
6.7	Comparison of measured H content after the total implantation to damage profiles.	117
6.8	Damage profiles from SDTrimSP simulations.	121
6.9	An measured ERDA spectrum following D implantation in the W sample.	125
6.10	ERDA and TDS results for monitoring the D content in W during a step-wise heating ramp.	126

6.11	The expected damage profiles and ion ranges from 3 keV D^+/D_2^+ bombardment.	127
6.12	ERDA for D retention compared to literature data.	128

List of Tables

4.1	ToF-ERDA measurements of elemental concentrations in the wollastonite films.	51
4.2	Fitting parameters for sputtering yields of CaSiO ₃ by Ar ⁺ irradiation. . .	56
4.3	Fitting parameters for sputtering yields of CaSiO ₃ by 2 keV H ₂ ⁺ irradiation.	61
4.4	Fitting parameters for sputtering yields of CaSiO ₃ by 3 keV ³ He ⁺ and 4 keV ⁴ He ⁺ irradiation.	66
4.5	Fitting parameters for the fluence dependence of the sputtering yield of CaSiO ₃ under 3 keV ³ He ²⁺ and 8 keV Ar ⁸⁺ irradiation.	69
4.6	Overview of calculated steady state surface concentrations and sputtering yields of CaSiO ₃ for a solar wind composition of 96% H ⁺ and 4% He ²⁺	81
5.1	Comparison of the augite samples' composition and the estimated composition of Phobos' surface.	89
5.2	Difference of O ⁺ measurement results compared to SDTrimSP simulations.	92
5.3	Fitting parameters used for describing the sputtering yields of atomic and molecular ions by the formula proposed by Eckstein and Preuss.	103
5.4	A table of the sputtering yields of Phobos from solar wind and planetary O contributions.	104

List of Abbreviations

ADC	Analog Digital Converter
AES	Auger Electron Spectroscopy
AFM	Atomic Force Microscope
amu	atomic mass unit
BCA	Binary Collision Approximation
CAD	computer-aided design
DFT	Density Functional Theory
dpa	displacements per atom
EBS	Elastic Backscattering Spectrometry
ECRIS	Electron Cyclotron Resonance Ion Source
ENR	Enabling Research
ERDA	Elastic Recoil Detection Analysis
ESA	European Space Agency
eV	electronvolts
FC	Faraday Cup
GHz	gigahertz
HCI	Highly-Charged Ion
HPGe	High Purity Ge
IAP	Institute of Applied Physics
IBA	Ion Beam Analysis
IPP	Max-Planck-Institute of Plasma Physics
ITER	International Thermonuclear Experimental Reactor

- JAXA** Japan Aerospace Exploration Agency
- keV** kilo-electronvolt
- MAVEN** Mars Atmosphere and Volatile Evolution
- MD** Molecular Dynamics
- MeV** mega-electronvolt
- MMX** Martian Moons eXploration
- MSO** Mars-Solar Orbital
- NRA** Nuclear Reaction Analysis
- PC** personal computer
- PFC** plasma-facing component
- PIPS** Passivated Implanted Planar Silicon
- PIXE** Particle-Induced X-ray Emission
- PLC** programmable logic controller
- PLD** Pulsed Laser Deposition
- QCM** Quartz Crystal Microbalance
- QP** quadrupole
- RBS** Rutherford Backscattering Spectrometry
- RGA** Residual Gas Analyzer
- RMS** root mean square
- SDD** Silicon-Drift Detector
- SDTrimSP** Static-Dynamic TRIM Sequential-Parallel
- SIGMA** Set-up for In-situ Growth, Material modification and Analysis
- SRIM** Stopping and Range of Ions in Matter
- STM** Scanning Tunneling Microscope
- SW** solar wind
- TPD** Temperature-Programmed Desorption

TRIDYN Dynamic TRIM

TRIM Transport of Ions in Matter

TDS Thermal Desorption Spectroscopy

ToF-ERDA Time-of-Flight Elastic Recoil Detection Analysis

UHV ultra-high vacuum

XRD X-Ray Diffraction

XPS X-ray Photoelectron Spectroscopy

ZBL Ziegler, Biersack and Littmark

Danksagung

Diese Dissertation setzt sich primär mit den wissenschaftlichen Themen meiner letzten dreieinhalb Jahre in der Arbeitsgruppe Atom- und Plasmaphysik auseinander. Ich will hier aber auch noch jenen danken, die mich auf dieser wissenschaftlichen Reise unterstützten und begleiteten.

Mein besonderer Dank gebührt meinem Doktorvater, Prof. Friedrich Aumayr, nicht nur für die tolle Betreuung während meiner Dissertation, sondern auch für die große Unterstützung während meiner gesamten bisherigen wissenschaftlichen Laufbahn. Ich lernte von Dir das wissenschaftliche Arbeiten und bekam schon früh die Gelegenheit, an internationalen Konferenzen teilzunehmen und dort meine Forschungsergebnisse zu präsentieren, was eine bei Weitem nicht selbstverständliche Gelegenheit darstellte. Diese Möglichkeiten, unzählige Forschende aus anderen Gruppen zu treffen und sich mit ihnen austauschen zu können, schätzte ich sehr. Du brachtest mir außerdem stets das Vertrauen entgegen, meine eigenen wissenschaftlichen Interessen innerhalb der vorgezeichneten Wege umzusetzen und unseren Forschungsthemen meinen eigenen Stempel aufzudrücken. Dass Du mir sowohl bei der Weltraumforschung als auch bei der Fusionsforschung zusätzliche Projektverantwortung übertrugst, war überaus motivierend für mich und ich profitierte von dieser vielfältigen Förderung sehr. Zudem schätzte ich es sehr wert, dass Du immer ein offenes Ohr und einen guten Ratschlag parat hattest. Deiner Anleitung verdanke ich wirklich viel!

Ich habe mich in der Arbeitsgruppe Atom- und Plasmaphysik von Anfang an sowohl wissenschaftlich als auch sozial sehr gut aufgehoben gefühlt. Daher will ich mich auch bei meinen Kolleginnen und Kollegen bedanken.

Herbert, die Zusammenarbeit im Space-Team, als Diplom- und später als Doktor-Partner, war immer eine große Bereicherung für mich. Ich bewundere Dein technisches Geschick sowie Deine Bereitschaft, anfangs nur erträumte Ideen dann tatsächlich umzusetzen. Unsere Klettertrips, die gemeinsamen Spieleabende und der tägliche Wettstreit, wer am besten finnische Wälder und mongolische Steppen zuordnen kann, waren immer ein erholsamer Ausgleich.

Schmu, Dein Durchhaltevermögen sowohl bei wissenschaftlichen Problemstellungen

als auch bei Bergläufen war ein tolles Beispiel dafür, dass man mit entsprechendem Einsatz alles schaffen kann. Die Zeit mit Dir gemeinsam im Büro und in Jülich genoss ich sehr, nicht nur weil es regelmäßig Schokolade gab. Für Euren kleinen Theodor empfehle ich dann aber doch eine ausgewogenere Ernährung.

Janine, Letzte in der ausgestorbenen Linie der Level-5-Doktorandinnen, Deine Zielstrebigkeit war immer eine große Inspiration für mich, ebenso schätzte ich Dein offenes Ohr für unterschiedliche Probleme. Auch die gemeinsamen Abenteuer rund um den Globus werde ich sehr positiv in Erinnerung behalten. Es freut mich zudem sehr, dass Du nun ebenfalls für die Weltraumforschung begeistert werden konntest, und ich bin mir sicher, dass Du auch bei Ruag erfolgreich sein wirst.

Georg, ich freute mich jedes Mal auf die positive Stimmung, die Du nach längeren Garching- oder Waldviertelaufenthalten wieder auf die Uni mitbrachtest. Die gemeinsamen Kinobesuche oder sportlichen Aktivitäten waren auch immer eine willkommene Abwechslung. Wirklich bemerkenswert finde ich, wie du Deine vielfältigen Projekte managst, und ich drücke Dir die Daumen, dass du Deinen Weg in der Fusionsforschung weiter gehen wirst.

Anna, Dein Einsatz für die aktuellen wissenschaftlichen Probleme stellten auch für mich oft eine Inspiration dar, an den eigenen Lösungen weiterzuarbeiten. Außerdem bist Du als kulinarische Versorgerin, Event-Organisatorin und gutes Gewissen der AG so ein essenzieller Teil der Gruppe geworden, dass man sich eigentlich fragt, wie das vorher alles funktioniert hat.

Christian, unsere gemeinsamen Uppsala-Messaufenthalte waren sehr spannende, wenn auch anstrengende Erfahrungen, auf denen wir beide einiges darüber lernten, wie man sich effizient in neue Themengebiete einarbeitet. Deine Begeisterung für Deine wissenschaftliche Tätigkeit und deine Genauigkeit, die Du regelmäßig zeigst, sind Eigenschaften, die ich sehr bewundernswert finde.

Gabriel, Du bringst eine tolle Stimmung in die Gruppe und ich empfand es immer als sehr spannend, von den aktuellen Fortschritten in eurem Labor zu hören. Vielen Dank außerdem dafür, dass Du immer Zeit für Fragen zum AFM hattest.

Lidija, auch Dein frischer Wind lockerte den Alltag immer wieder auf. Seien es Plasmoden, auxetische Strukturen oder komplett andere Themen - die gemeinsamen Kaffeepausen wurden nie langweilig.

Ausdrücklich möchte ich mich auch bei Richard bedanken. Von Dir konnte ich viel über den theoretischen Hintergrund der Ionen-Festkörper-Wechselwirkung und die Arbeit im Labor lernen. Es gab keine Frage, auf die Du nicht eine Antwort parat hattest, und es war sehr hilfreich, dass ich immer mit Problemen und Ideen zu Dir kommen konnte. Ich bin mir sicher, dass die Zeit für Ionen in den nächsten Jahren

sehr erfolgreich verlaufen wird.

Zu guter Letzt gebührt natürlich ein großer Dank auch meinen Eltern. Ich schätze wirklich sehr, dass Ihr mich bedingungslos unterstützt und dass Ihr immer für mich da seid, wenn ich einmal einen Rat brauche.

